SURFACE CHARACTERIZATION OF HETEROGENEOUS CATALYSTS USING LOW ENERGY ION SCATTERING SPECTROSCOPY COMBINED WITH ELECTROCHEMISTRY

A Dissertation

by

STEPHANUS AXNANDA

Submitted to the Office of Graduate Studies of
Texas A&M University
in partial fulfillment of the requirements for the degree of

DOCTOR OF PHILOSOPHY

December 2009

Major Subject: Chemistry

SURFACE CHARACTERIZATION OF HETEROGENEOUS CATALYSTS USING LOW ENERGY ION SCATTERING SPECTROSCOPY COMBINED WITH ELECTROCHEMISTRY

A Dissertation

by

STEPHANUS AXNANDA

Submitted to the Office of Graduate Studies of
Texas A&M University
in partial fulfillment of the requirements for the degree of

DOCTOR OF PHILOSOPHY

Approved by:

Chair of Committee,	David Goodman
Committee Members,	James Batteas
	Marcetta Darensbourg
	Daniel Shantz
Head of Department,	David H. Russell

December 2009

Major Subject: Chemistry

ABSTRACT

Surface Characterization of Heterogeneous Catalysts Using Low Energy Ion Scattering Spectroscopy Combined with Electrochemistry. (December 2009)

Stephanus Axnanda, B.S., Texas A&M University;

M.S., Texas A&M University

Chair of Advisory Committee: Dr. David Goodman

Fundamental studies of heterogeneous catalysis were performed and presented in this dissertation to gain a better understanding of heterogeneous catalytic reactions at a molecular level. Surface science techniques were employed in achieving the goal. Low energy ion scattering spectroscopy (LEISS) is the main surface science technique which will be used in all the studies discussed throughout this dissertation. The main objectives of LEISS measurements are to: 1) obtain the information of surface composition of heterogeneous catalysts from the topmost layer; 2) observe the effects of reaction conditions on the surface composition of heterogeneous catalysts.

The surface composition and morphology of Au-Pd clusters bimetallic model catalysts supported on SiO_2 were characterized using LEISS, infrared reflection absorption spectroscopy (IRAS), and temperature programmed desorption (TPD). It is observed that relative to the bulk, the surface of the clusters is enriched in Au. Ethylene adsorption and dehydrogenation show a clear structure-reactivity correlation with respect to the structure/composition of these Au-Pd model catalysts.

Pd-Sn bimetallic model catalysts were also studied. The surface composition, structure, and chemisorption properties were studied by low energy ion scattering spectroscopy (LEIS), low energy electron diffraction (LEED), X-ray photoelectron spectroscopy (XPS), infrared reflection adsorption spectroscopy (IRAS), and temperature programmed desorption (TPD). It is observed that a pair of suitably spaced, isolated Pd monomers is the efficient site for vinyl acetate (VA) synthesis.

A AuPd(100) alloy single crystal was also studied using LEISS and scanning tunneling microscopy (STM). It is shown that the distance between surface Pd atoms controls the catalytic formation of vinyl acetate from ethylene and acetic acid by AuPd catalysts. Scanning tunneling microscopy reveals that sample annealing has a direct effect on the surface Pd arrangements.

A combined UHV (LEIS, STM, XPS) and electrochemical study on Pt_3Co thin film and clusters alloy is also described in this dissertation. It was found that Pt-Co films yield a stable and well-ordered alloy at the outermost layer when annealed at a sufficiently high temperature, 900 to 1000 K. The surface phase diagram of the Pt-Co co-deposit shows Pt surface segregation. The stability of Pt-Co electrocatalysts was also studied.

DEDICATION

To my parents, Helinda, Antonia, and Alda

ACKNOWLEDGMENTS

I would like to express my deepest gratitude to many people whose supports have helped me to succeed throughout my doctoral study here at Texas A&M. I would like to first thank Dr. Goodman who has been a great advisor and taught me valuable skills necessary to achieve goals in performing scientific research. I also would like to thank him for his encouragement to keep me focused on achieving the best results in my doctoral degree instead of settling with mediocre results. I would also like to thank all my committee members, Dr. Dan Shantz, whom also has influenced me in pursuing knowledge through research, Dr. James Batteas, and Dr. Marcetta Darensbourg.

My deepest gratitude also goes to all the group members who I have had opportunities to work with and get to know. I would like to thank Dr. Kai Luo who had guided me in operating the surface science techniques available in the LEIS chamber. I would like to also thank Dr. Tao Wei, whom I had a privilege to work on IRAS chamber during my first year in my PhD program. Dr. Patrick Han, thank you for your collaboration. For Kyle Cummins and Dr. M. P. Soriaga, I would also like to thank you for the collaborative work we have done in the last two years of my doctoral study. Zihao and Zhoujun, thank you for your enthusiasm in collaborating with me on the Pt-Co project. Dr. Fan Yang, Dr. Yun Cai, Dr. Zhen Yan, Matt, Dr. Sean McClure, Dr. Feng Gao, and Dr Yi Ling thank you for the help around the lab and your acquaintance. Amy Liu, thank you for taking care of me and everyone else in the lab.

For Mama and my late Papa, I cannot tell you how much I owe you for all the things I have learned, all the success I have and will gain, and all the love I will always have from and for you. Terima kasih Ma, Pa.

TABLE OF CONTENTS

TABLE OF CONTENTS (continued)

Page

LIST OF FIGURES

Page

LIST OF FIGURES (continued)

Page

LIST OF FIGURES (continued)

Page

LIST OF FIGURES (continued)

Page

LIST OF FIGURES (continued)

Page

1. INTRODUCTION

Studies of Heterogeneous Catalysts Using Surface Science Techniques

Heterogeneous catalysts are important materials in many fields such as chemical production, energy storage and conversion, renewable energy, and environmental science. The activity of heterogeneous catalysts depends on many factors such as size and shape of the particles, properties of the metals, and supports or promoters of the catalyst. Knowledge of structural and chemical properties of the catalyst is needed to improve its selectivity and activity towards specific reactions. This knowledge comes from a fundamental understanding of the catalysts that correlates the microscopic structure of the catalyst and reaction kinetics. In the past decade, efforts have focused on obtaining a fundamental understanding of the heterogeneous catalyst.[1-4] Understanding the complex catalysts at the microscopic level has been made possible by studying model systems that have specific features of real catalysts without the full complexity of the catalyst itself.

The ultimate goal in heterogeneous catalysis research is to understand the correlation between the atomic-scale structure of a catalyst with its catalytic activity and selectivity toward specific reactions and products. Surface science techniques can provide information about atomic and molecular adsorption, diffusion, reaction, and

---

This dissertation follows the style of *Journal of Physical Chemistry B.*

desorption of molecule adsorbates on the surface of the catalyst by observing the surface of the model of the real catalyst. Most surface science techniques are performed under ultrahigh-vacuum (UHV, < 10^{-9} Torr) conditions. These reaction conditions differ markedly from the usual high-pressure and high-temperature conditions used in actual catalytic applications. The difference in the conditions used in surface science studies and the real-world catalyst is referred to as the "pressure gap." Studies of CO oxidation on a Pd(111) single crystal,[1] Ru(001),[2] and Ir(111)[3] have shown that information obtained in low-pressure conditions can be applied to high-pressure conditions assuming that the surface structure of the catalyst does not undergo any modification with pressure change.

Initial studies of heterogeneous catalysis using surface science techniques were performed on model catalysts using metal single crystals.[1,2] The adsorption of reactant gases and the reaction rate of a specific reaction with a metal single crystal were studied to understand the mechanism of the reaction. In 1978, Ertl studied the oxidation of CO on a Pd(111) single crystal using a molecular beam technique.[1] It was observed that CO oxidation occurs after both the reactant gases, O_2 and CO, are adsorbed on the surface of Pd. This mechanism is also known as Langmuir-Hinshelwood. However, it is observed that at different pressure and temperature ranges, changes in the adsorption rate of O_2, co-adsorption of CO and O_2, and in the geometrical arrangement within the adlayer will occur. Therefore, it was then proposed that the CO oxidation reaction rate expression is dependent on the coverage of CO and O_2.[1] There were many other metal single crystals used in the study of CO oxidation such as Ru(001) [2] and Ir(111).[3] However, real

catalysts are rarely in the form of bulk metals. Most catalysts are prepared as metals or oxide metals supported on oxide materials. Therefore, the studies reported do not represent all of heterogeneous catalysis. Fortunately, it is possible to apply surface science methods to study oxide surfaces that better represent real catalysts.

Supported Catalysts

Surface science has been applied in studies of many oxide-supported catalysts. In 1998, Valden et al. applied surface characterization techniques on Au catalysts supported on oxide materials to explain the origin of increased Au clusters activity in CO oxidation reactions.[4] Recently, it has been observed that the catalytic activity of highly dispersed Au on a metal oxide support is greatly enhanced toward a variety of reactions such as the partial oxidation of hydrocarbons, hydrogenation of unsaturated hydrocarbons, [5-9] reduction of nitrogen oxides, [10] and CO oxidation at low temperatures. [11-14] This discovery has led to considerable research in an attempt to better understand the unusual catalytic properties of Au. Although various mechanisms have been proposed, no consensus exists at this time. In the experiments performed by Valden et al., a highly dispersed nanosized planar model of Au supported on TiO_2 was studied by depositing Au particles on top of TiO_2 single crystals, TiO_2 (110). The system was probed with scanning tunneling microscopy (STM) to obtain an atomic scale image of the surface of the system. Scanning tunneling spectroscopy (STS) was used to obtain information about the electronic state of the observed area. It was found that the thickness of the particle rather than the particle diameter is the key structural feature that defines the catalytic activity. [14]

Further investigation in the use of the Au/TiO_2 system for CO oxidation provided information on the effects of surface composition and electronic state with regard to catalytic activity. The interaction between Au and the support alters the electronic structure of Au nanoparticles.[15,16] When depositing Au on an oxide support, defects on the oxide are thought to play an important role in the bonding that leads to a charge transfer from the oxide to the Au atoms.[15] Upon Au deposition onto TiO_2(110), low-energy ion scattering (LEIS) data show that Au initially forms two-dimensional (2-D) islands up to a critical coverage that depends on the defect density of the titania surface; higher Au coverage leads to a three-dimensional (3-D) particle growth.[15,16] The maximum coverage of the 2-D domains correlates with the surface defect density. [7,17,18] However, it has recently been shown that Au wets a reduced titania surface more completely than does Au on TiO_2 .[19-22] Specifically, Au completely wets a highly-ordered TiO_x film deposited on a Mo(112) substrate by forming well-ordered Au monolayer and bilayer structures. [19-22] A comparison between Au on TiO_2 [7,17,18] and Au on a reduced titania surface (TiO_x/Mo(112)) [19-22] shows that Au interacts to a greater extent with a reduced titania, Ti^{3+}.[22] The studies described demonstrate that surface science is a powerful technique for studying this area of heterogeneous catalysis, namely an oxide-supported metal catalyst. There are other types of heterogeneous catalysts that also have important roles in the industrial applications, bimetallic catalysts.

Bimetallic Catalysts

Fundamental surface science studies of bimetallic alloy systems are important to many industrial applications, some of which include metallurgy, catalysis,

electrochemistry, magnetic materials, and microelectronics fabrication.[23] Particularly in heterogeneous catalysis, the addition of a second metal often significantly enhances the reaction activity, selectivity, and stability.[24-26]

Further optimization of the catalytic performance requires a thorough understanding of the reaction mechanism at the atomic level for which model surface science studies on well-defined surfaces can provide critical information. The study of the Pt-Sn bimetallic catalyst is an example of the use of surface characterization techniques on a bimetallic system. The preparation of ordered Pt-Sn surface alloys was first demonstrated by depositing Sn on Pt(111) or Pt(100) followed by annealing to elevated temperatures.[27-30] These well-characterized surface templates were used for extensive catalytic reaction studies.[25,31-35] Model studies have provided a more in-depth understanding of the chemistry observed on ordered alloy surfaces, including the relative importance of ensemble and ligand effects. Another important bimetallic catalyst system is Pd-Sn system. Only a limited number of model studies on Pd-Sn bimetallic systems have been performed, despite the importance of Pd-based industrial catalysts.[36-39] Hamm et al.[36] and Lee et al.[37] studied the formation of two ordered Pd-Sn surface alloys by thermal treatment of vapor-deposited Sn films on a Pd(111) single crystal. Depending on the preparation conditions, two surface periodicities, p(2 × 2) and ($\sqrt{3} \times \sqrt{3}$)R30°, were observed with surface stoichiometries of Pd_3Sn and Pd_2Sn, respectively.[36,37] On the Pd(110) single crystal, two ordered structures, c(2 × 2) and (3 × 1), were also reported, which corresponded to an 0.5 monolayer (ML) and 0.67 ML of Sn in the surface layer.[39] In both cases, a strong chemical interaction between Sn and Pd was deduced based on

core-level binding-energy shifts (CLS) and attenuation of the CO adsorption energy in temperature programmed desorption (TPD) data.[37,39] However, no detailed investigations concerning Pd-Sn alloy formation on <100> oriented substrates have been reported. Previously, we studied disordered Pd-Au model alloy surfaces[24,40-44] where Pd atoms were found to be isolated by Au atoms at low surface Pd coverage.[24,40-45] It has been proposed that a pair of these Pd monomers serve as the active site for vinyl acetate synthesis.[24,40] A study of a Pd-Sn bimetallic model alloy will be presented in a later section.

Surface and Electrochemical Characterization of Pt-Co Electrocatalysts

To correlate surface and electrocatalytic properties, surface science can also be used in the study of electrocatalysts combined with traditional electrochemical measurements. In this study, Pt-Co is analyzed to obtain a better understanding in the use of this bimetallic system in fuel-cell applications. A fuel cell can be thought of as a cold-combustion device capable of converting stored chemical energy into usable electrical energy. Without a large heat transfer, a fuel cell is not plagued by the conversion efficiency penalties associated with hot-combustion devices. However, unlike a battery, the fuel cell is not a closed system as fuel and oxidant must be continuously supplied for its operation. In an operating fuel cell, the fuel is introduced through the fuel feed plates to the surface of the anode. Simultaneously, oxygen is delivered through oxidant feed plates to the surface of the cathode. The reactions that occur at the electrodes are facilitated by the surface properties of the catalyst. At the anode, H_2 is catalytically oxidized to H^+ through the following reaction

$$H_2 \rightarrow 2H^+ + 2e^- \; E^{0'} = 0.0V \; . \qquad (1.1)$$

The positively charged protons, because of a concentration gradient, diffuse through the electrolyte toward the cathode. The electrons travel through the completed external circuit toward the cathode where reduction of the oxidant will occur.

$$\tfrac{1}{2}O_2 + 2H^+ + 2e^- \rightarrow H_2O \; E^{0'} = 1.229V \qquad (1.2)$$

At the cathode, electrons recombine with H^+ from equation (1.1) and in the presence of oxygen, react to form water, which can be easily transported from the cell, giving

$$H_2 + \tfrac{1}{2}O_2 \rightarrow H_2O \; E^{0'} = 1.229V \qquad (1.3)$$

whose products, besides water, are the unidirectional flow of energy in the form of electrons. Figure 1 shows the reactions occurring at the electrodes.

Although the process is relatively simple, hydrogen fuel-cell research is over 200 years old. Fuel cell research can be said to have begun in the 1800s by Nicholson and Carlisle with their research of water electrolysis.[46] In 1833, Faraday's laws of electrolysis were proposed, [47] followed by the theory on the inter-relation of chemical affinity, electricity, heat, and magnetism in 1835.[48] In 1843, the first functioning hydrogen fuel cell, the "gas battery" was constructed and demonstrated by William Robert Grove.[49] In 1893, Friedrich Wilhelm Ostwald, founder of the field of physical chemistry, formulated the theoretical underpinnings of how the hydrogen fuel cell operates.[46,50,51] Following another 50 years of development, Francis Tomas Bacon invented the first practical hydrogen-oxygen fuel-cell, licensed to Pratt & Whitney. An

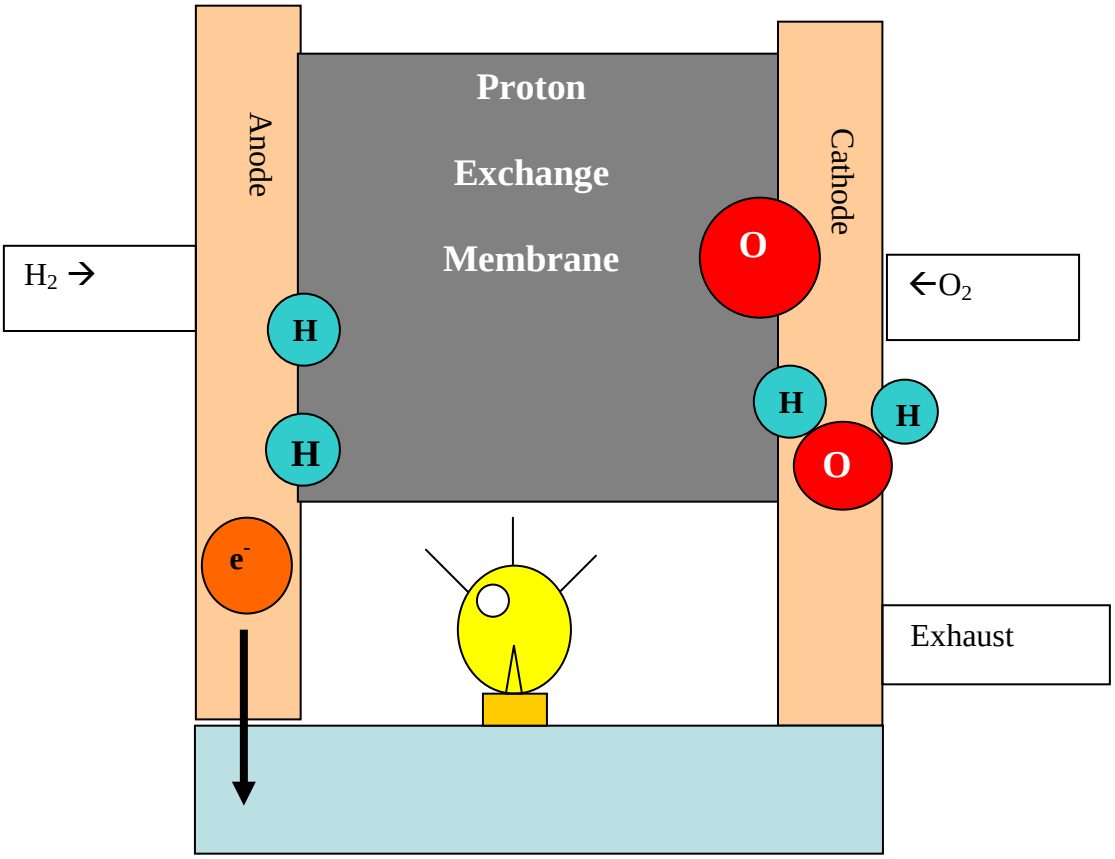

Figure 1. Schematic of fuel cell.

alkaline fuel cell using a nickel catalyst was developed. By increasing the operating temperature to 205 ºC and the pressure to about 600 psi, useful currents were achieved without boiling off the electrolyte. By increasing the catalyst-electrolyte-gas interfacial area, a 5kW system capable of powering a welding machine, a circular saw, and a 2-ton capacity forklift truck was constructed.[51,52]

Of the different types of fuel cells, the proton exchange membrane fuel cell (PEMFC) shows the most promise for commercialization. The PEMFC is the first type of fuel cell that had practical applications. In the 1960s, the National Aeronautic and Space Administration's Gemini space flight program used the PEMFC for on-board power generation. Twenty years later, the state of California and the U.S. Partnership for a New Generation of Vehicles program (PNGV) initiated the use of the PEMFC in transportation applications.[53] The electrolyte in the PEMFC is a solid proton-conducting membrane that allows the PEMFC to operate at low temperature and produces specific power (W/kg) and power density (W/cm^3), both of which are higher than other types of fuel cells. Therefore, in the PEMFCs, the membrane and the electrode are the important components. Of these two components, the membrane electrode assembly (MEA) is the center of operation in the fuel cell. However, there are two major problems in commercializing this technology: high cost and low reliability. The fuel-cell catalyst is the main contributor to these problems. In current PEMFC construction, Pt metal dispersed on a support is the most widely used electrocatalyst in fuel cells. Major drawbacks in employing Pt as the catalyst include high cost, sensitivity to contaminants,

and loss of Pt surface area.[54] For the PEMFCs, platinum is used as the catalyst in both the anode and the cathode.

Oxygen-Reduction Reaction (ORR) on Pt and Pt Alloy Thin Films

The mechanisms and reaction pathways of the oxygen reduction reaction (ORR) have been investigated thoroughly in an attempt to realize the promise of low-cost, low-temperature hydrogen fuel cells. As will be treated in a later section, the oxygen-reduction kinetics is very sluggish compared with that at the anode, and remains a major bottleneck in the overall performance of fuel cells. Slow electrode kinetics results in large overpotentials associated with reaction activation. Overcoming this problem is the main goal in efforts to develop better electrocatalysts.

Cell Overpotentials

When a net current flows from a fuel cell, the terminal voltage of the cell, E_{cell}, drops from the open circuit voltage, E_{rev}, by a value that is proportional to the current flowing from the cell. In this case, the cell is said to be polarized. Polarization of a cell can be further classified into three main types: activation polarization, concentration polarization, and ohmic polarization.[55]

Activation Polarization

Activation polarization is the potential drop across the cell that results from a net flow of current for reactions exhibiting slow electron transfer rates. When this occurs, part of the output potential of the cell must first be supplied as activation energy to keep up with the current demands of the cell. Many factors play a role in this loss, including

structure of the electrical double layer (EDL), interactions with solvent and electrolyte, interactions with the electrode surface, and low intrinsic reactivity. For most hydrogen-oxygen fuel cells, electron transfer is the rate-determining step (RDS). This rate at the cathode is on the order of 10^5 times less than the rate of hydrogen oxidation at the anode. This low-rate constant is the most significant source of over-potential with respect to the ORR at a Pt electrode and can quickly rise to 300 to 400 mV**.** The majority of studies on fuel cells are aimed at improving this problem.

Ohmic Polarization

Ohmic polarization or ohmic losses in the cell is the result of the electrical resistances of the electrolyte, electrode, and electrical connections. This overpotential scales linearly with current density, following Ohm's Law. This is an unavoidable drop, but can be minimized by careful materials selection and cell construction.

Concentration Polarization

Concentration polarization is the potential drop across the cell that results from mass transfer requirements in the conditions of high current. It results from the need to deliver electroactive species through the diffusion layer for electron transfer to occur. Even in cases of very large rate constants, concentration polarization will be present in perhaps tens of millivolts. However, fuel cells are rarely operated in the current range where this loss is significant.

ORR Mechanism on Pt

As demonstrated by Gubbins and Walker,[56] oxygen reduction can proceed by one of two overall pathways in aqueous media. In acidic solutions:

1. Direct 4 e^- pathway:

$$O_2 + 4H^+ + 4e^- \rightarrow 2H_2O \; E^{0'} = 1.229V \tag{1.4}$$

2. Peroxide pathway:

$$O_2 + 2H^+ + 2e^- \rightarrow H_2O_2 \; E^{0'} = 0.67V \tag{1.5}$$

followed by either reduction of the peroxide

$$H_2O_2 + 2H^+ + 2e^- \rightarrow H_2O \; E^{0'} = 1.77V \tag{1.6}$$

or its decomposition

$$2H_2O_2 \rightarrow 2H_2O + O_2 \tag{1.7}$$

At an electrode where oxygen reduction is occurring, one or both of these reactions can be present at the same time and the products may feed into each other. More detailed descriptions of the overall mechanism and reaction process have been proposed for various conditions.[56] A pathway proposed by Appleby and Savy considers likely reaction intermediates and accounts for feedback from side reactions.[57] Figure 2 shows the proposed reaction pathways.[57] For a Pt surface, the 4e^- direct-reduction process can be described as following a bridge-type Griffith's model of a transition metal oxide.[58]

Some important points need to be considered. In the case where oxygen coverage of the electrocatalyst surface can be increased, more reduction will occur on oxide-covered sites; thus, favoring the direct 4e^- mechanism and operation closer to the

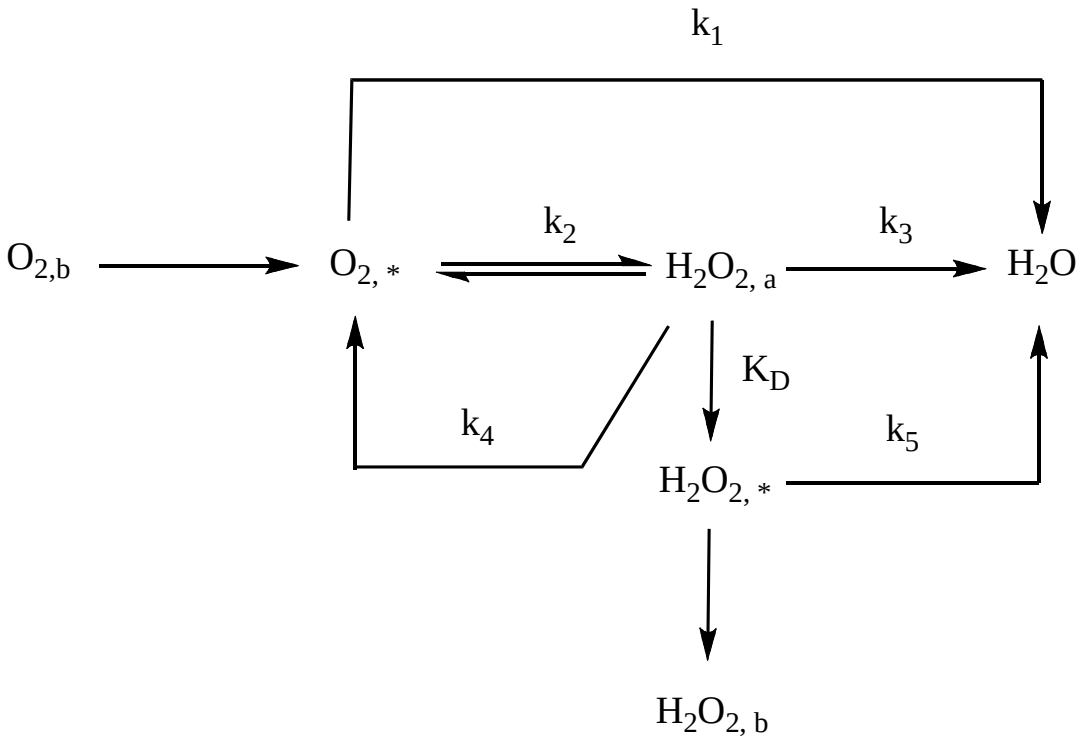

Figure 2. Proposed reaction pathways by Appleby and Savy.[57]

reversible cell potential. Additionally, the adsorption model proposed by Yeager[58] indicates the importance of the spacing of metal centers relative to the oxygen. This gives us a good impetus to pay attention to the lattice parameters of alloy surfaces and how they pertain to catalysis.

Theoretical and Experimental Studies on Model Catalysts for ORR

In the PEMFC, cathode and anode electrode materials are heterogeneous catalysts. As explained previously, increasing the catalytic activity of the cathode in the PEMFC results in a higher fuel efficiency and reduces the amount of Pt, increasing the cost efficiency of the fuel cells. Therefore, many efforts have been directed toward searching for a way to reduce the amount of Pt used while simultaneously increasing the catalytic activity. One way to increase the efficiency of the PEMFC is to increase the catalytic activity of the ORR catalyst. It has been shown that alloying Pt with a less-noble metal can achieve this in a dual-effect mode: first, by increasing the catalytic activity towards ORR and second, by decreasing the Pt required for the same output power density.

It was recently reported that the Pt-Co alloys have enhanced catalytic activity compared to pure Pt for ORR.[59] Some explanations for the increase of catalytic activity of Pt-Co towards ORR have been proposed,[60-63] including (i) changes in the electronic structure of Pt atoms by the interaction with the alloying metal; (ii) changes in Pt-Pt bonding distance, and (iii) changes in oxygen-adsorption sites on Pt or alloying metal. Many studies to date have presented the changes in the catalytic activity of Pt-Co

electrocatalysts as compared to those of pure Pt in fuel cell. A few studies have characterized the functional Pt-Co electrocatalyst materials outside of the fuel cell.

Theoretically, it can be shown that the role of alloy metals in the increase of the electrocatalytic activity of Pt for the ORR is to tune the electronic structure of Pt.[64] Density functional theory (DFT) calculations were used to measure the activity of the model Pt-M alloy towards ORR. This activity is indicated by the oxygen-metal bond interaction[64] and shows that the oxygen-metal bond depends on the position of the metal d states relative to the Fermi level.[64] The plot of activity at 0.9 V versus d-band center position shows volcano-shaped dependence, which was also observed experimentally.[60] Another theoretical study performed by Wang and Balbuena proposed a mechanism in the increased activity toward ORR for any two metals.[65] They observed that when two metals with different occupancy of d-orbitals are alloyed, the d-orbital coupling effect between the two metals can significantly decrease Gibbs free energy for the electron transfer steps in the ORR. For example when metals with a low level of occupancy of d-orbitals, such as Co, Ni, Cr, or V, are alloyed with metals with fully occupied d-orbitals, such as Pd, Au, and Ag, the Gibbs free energy for electron transfer steps in the ORR will be decreased.[65] Hammer and Norskov made density functional theory calculations showing that a reduction of bond lengths between metals could be the explanation supporting the increased activity: in this case, Pd metal favors ORR.[66] When metals are alloyed, the d-band center of the metal can be shifted, resulting in a reduction of the metal's lattice parameter: i.e., shortening the bond lengths. The change in the metal d-band center will result in a change in the surface activity of the metals.[66]

In 2002, an experimental study by Stamenkovic et al characterized the real surface composition of Pt_3Co and Pt_3Ni using a highly sensitive surface science technique called low-energy ion scattering spectroscopy (LEISS).[67] With this combination they were able to establish a clear correlation between the catalyst surface properties and its activity towards ORR. From the LEISS study, it was shown that two different surfaces can be prepared in UHV, depending on the treatment of a bulk Pt_3Co and Pt_3Ni polycrystalline sample.[67] Following sputtering of the polycrystalline sample with 0.5 keV Ar^+ ions, the surface has a 75 at. % Pt and 25 at. % Co characteristic. When the polycrystalline is annealed at 1000 K, the topmost surface layer consists of only Pt atoms and has been referred to as a "Pt-skin." From their activity study, they found that the "Pt-skin" surface has a higher activity (3-4 times that for pure Pt) compared to Pt_3Co and Pt_3Ni when 0.1 M $HCLO_4$ is used as the electrolyte.

In 2006, Stamenkovic et al. presented another study of Pt-Co alloy, showing the effect of immersion on the alloy surface composition by the electrolyte as determined by LEISS, Auger electron spectroscopy (AES), and ultraviolet photoemission spectroscopy (UPS).[64] In this study, they found that following the immersion of "Pt-skin" in 0.1 M $HClO_4$, the LEISS of the sample does not change, indicating a constant surface composition. However, when a sputtered Pt_3Co sample was immersed, Co dissolution from the near surface was observed, giving a "Pt skeleton" surface. However, in this study, when a Pt-Co alloy with 50 at % Pt and 50 at % Co was annealed in UHV at 1000 K, the LEISS data showed no "Pt skin" formation on the surface. A weak increase in Co surface composition was observed for the annealed sample compared to the sputtered Pt-

Co sample. It can then be concluded then that the extent of Pt segregation in Pt alloy depends on the bulk ratio of the alloying components. However, there is no experimental study showing the real surface composition of Pt-Co alloys with varying bulk compositions after annealing to sufficiently high temperatures to achieve stable alloying composition. Also, no studies have been conducted at different fuel cell operating conditions, where the change in surface composition of Pt-Co electrocatalysts has been monitored after electrochemistry. In a later section, a case study performed in our laboratory is presented showing the surface phase diagram as well as a correlation between the surface composition and electrochemical behavior of Pt-Co model alloys utilizing surface science and electrochemistry techniques.

2. EXPERIMENTAL

This section provides brief descriptions of the important surface-science techniques used throughout the studies and discusses experimental procedures for each experiment described in this dissertation. Surface science techniques, such as X-ray photoelectron spectroscopy (XPS), LEIS, low energy electron diffraction (LEED), temperature programmed desorption (TPD), and STM, and electrochemistry measurements will be discussed briefly. Comprehensive reviews on XPS[68], LEIS[69], LEED[70], TPD[70,71], and STM[72] provide more detailed explanations about the techniques.

Ultra High Vacuum (UHV) Chamber

For most of the studies that will be discussed in the following sections, the UHV chamber is equipped with XPS, LEISS, LEED, and TPD. Figure 3 shows the front view of the UHV chamber. The base pressure of the chamber is 5 x 10^{-10} Torr. XPS and LEISS spectra are collected using a concentric hemispherical analyzer (PHI, SCA 10-360). The sample is mounted on a stainless steel sample probe at the top of the chamber. Liquid nitrogen can be filled into the probe to lower the sample temperature to around 80 K. On the feedthrough, there are four connections: two thermocouple connections and two copper leads for sample heating and cooling. A type C thermocouple (5%Re/W-26%Re/W, provided by H. Cross Co.) is used to measure the sample temperature. The sample can also be heated using a DC power supply that supplies current through the sample to heat it resistively. Resistive heating can bring the sample temperature up to 1500 K. For higher temperature heating, electron-bombardment heating is used. In

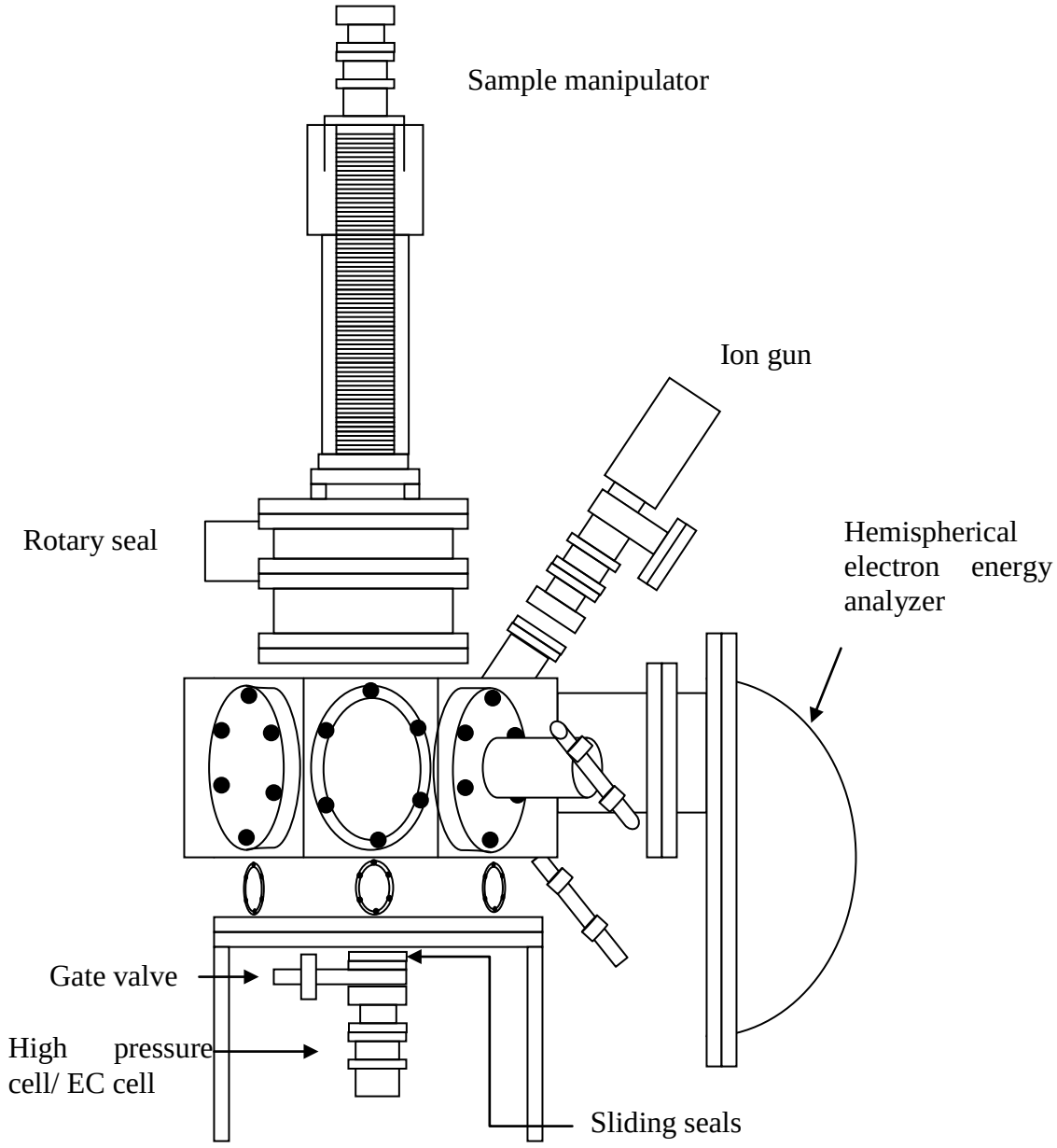

Figure 3. Front view of UHV chamber.

electron-bombardment heating, the sample is heated by a filament made out of W wire placed behind the sample. The sample is then positively biased (up to 600 V) to extract electrons from the W filament. At one end of the probe where the sample is mounted, a metal-ceramic feedthrough is attached.

Infrared studies were carried in a second chamber, equipped with AES, IRAS, and TPD with a base pressure of 1 x 10^{-10} Torr. The IR cell was equipped with CaF_2 windows and could be pressurized to several Torr. The sample can be cooled and heated as described previously.

For electrocatalytic activity measurements, the sample is transferred to an electrochemistry cell that is at a higher pressure condition through series of differentially pumped sliding seals. The sliding seals design consists of three Teflon seals separated from each other by two pump-out ports placed in between the seals. The pump-out port in the bottom section is pumped with a mechanical pump while the upper section is pumped by a turbo pump. The inner diameter of the seals fits perfectly over the polished chrome-plated probe. When the probe is passed through the seals and the differential pumping lines are connected, the UHV chamber is isolated from the elevated pressure section of the chamber. The differential pumping also allows the probe to be rotated without losing vacuum inside the chamber.

Surface Science Techniques

X-Ray Photoelectron Spectroscopy

Electronic structure of solid surfaces can be analyzed using photoelectron spectroscopy.[71,73] In photoelectron spectroscopy techniques, photons (hν) induce

electron emission from a solid surface, provided the photon energy is greater than the work function (Φ) plus the binding energy of the electrons. The work function of a solid is defined as the minimum energy required to remove an electron from the highest occupied energy level in the solid to the 'vacuum level'. Figure 4 illustrates the X-ray photoemission process.

In XPS, a monochromatic beam of X-ray collides with the sample surface, which causes electrons from both core and valence levels to be ejected. Core-level electrons are electrons at the inner quantum shells while valence electrons are electrons in the partially filled outer quantum shells that are more weakly bound. The outermost electrons are involved in chemical bonding. The ejected electron caused by the incoming photon has a certain kinetic energy that can be estimated as:

$$E_{kin} = h\nu - E_b - \Phi, \tag{2.1}$$

where E_b represents the binding energy of the particular core level. Each core-level peak represents particular elemental species. Therefore, by observing the binding energies of different core-level photoelectron peaks, elements at the surface can be identified.

Other then identifying elements available on the surface region, XPS can also be used to indicate the chemical environment of the elements. Core-level binding energies can be modified by many factors such as valence state of the element and the molecular environment in general. Changes in these factors can shift the core-level binding energy of an element as much as a few eV. By observing the shift in the binding energy of a pure element, information about bonding between atoms in the surface region, oxidation state, charge transfer, or electron orbital redistribution can be assessed.[68]

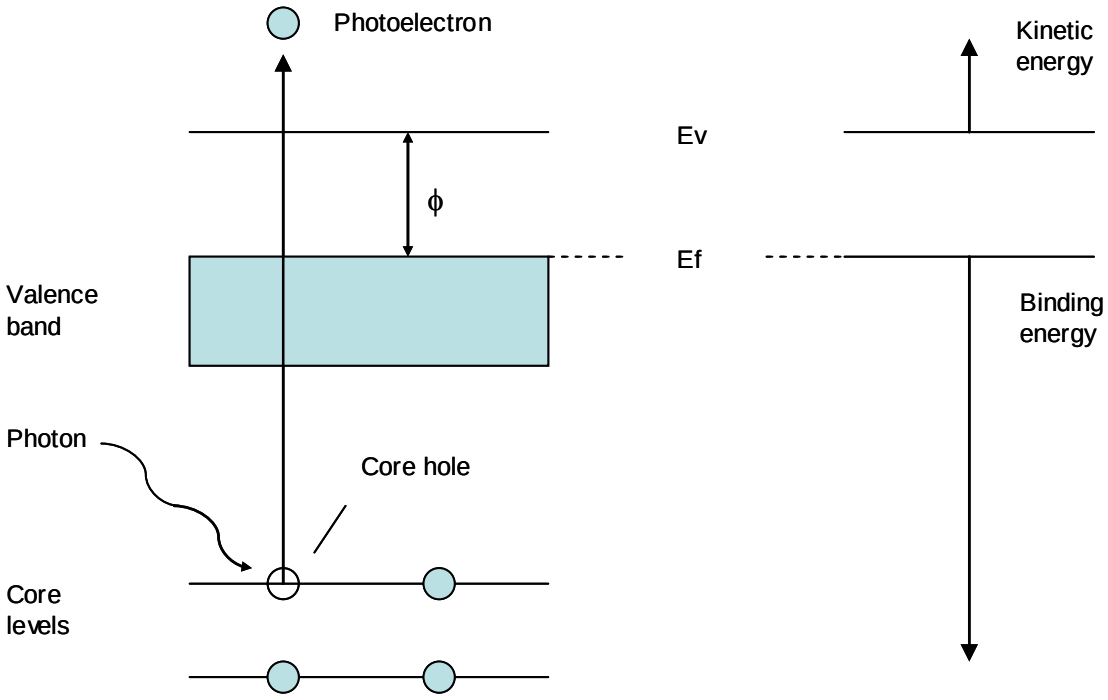

Figure 4. Diagram of photoemission process.

Another useful application of XPS in surface science techniques is determining the thickness of a deposited film on a surface. The thickness of the deposited film can be estimated by observing the attenuation of the XPS intensity caused by the underlying substrate, as defined by the following equation:

$$d = -\lambda[\ln(I / I_0)], \tag{2.2}$$

where d is the thickness of the deposited film, λ is the mean free path of the electron, I is the intensity of the underlying substrate after a certain amount of film is deposited, and I_0 is the initial intensity of the underlying substrate before any film is deposited.[68]

XPS can also be used to differentiate the composition at various surface depths. X-rays can penetrate deep into materials; however, when an X-ray beam strikes the surface at a grazing angle, only near surface atoms will be identified by XPS. Therefore, by setting the X-ray beam at different angles with respect to the sample, information from various depths of the surface can be acquired.[68]

The studies that will be discussed in this dissertation were performed using a Perkin-Elmer 5500 XPS system. This system uses a hemispherical analyzer and a dual Mg/Al anode.

Low-Energy Ion-Scattering Spectroscopy (LEISS or ISS)

LEISS provides surface atomic composition information. An ion beam with energy ranging between 100 eV and 10 keV collides with a target surface and the primary backscattered ions are detected. Ions from inert gases such as He^+, Ne^+, and Ar^+ are the most commonly used incident ions. When the incident ion impinges the target surface at a fixed angle, it will lose a certain amount of energy that depends on the mass

of the surface atoms. In LEISS, only the signal from the scattered ions will be analyzed for quantitative surface analysis. The analyzed ions are scattered from the surface mainly by binary collisions. In these elastic binary collisions, the incoming ions can be seen as a projectile having mass of m_1^+ and initial energy E_0. The surface can be treated as a target atom with mass m_2 at rest. When the projectile collides with a target atom, there will be a resulting energy transfer that depends on the scattering angle, θ. Figure 5 shows a schematic of a binary collision in ISS techniques. The scattered projectile will then have a different energy, E_f, which can be calculated from energy and momentum conversion, yielding the following equation[69]:

$$E_f = \left(\frac{\cos\theta \pm \sqrt{\left(\frac{m_2}{m_1}\right)^2 - \sin^2\theta}}{1 + \frac{m_2}{m_1}} \right)^2 .E_0 \qquad (2.3)$$

where the positive sign is applied when $m_2/m_1 \geq 1$, while both positive and negative signs are used when $0 \leq m_2/m_1 \leq |\sin\theta|$. Therefore, the LEISS data plot an energy spectrum of the different energy losses which correspond to elements with specific masses available on the surface of the target.[74]

In a LEISS experiment, the scattering angle, θ, is usually about 140°.[69] From equation (2.3), it is shown that backscattering with $\theta > 90°$ for $m_2/m_1 \leq 1$ is impossible. Because the lightest inert ion available is He^+, hydrogen is the only element that cannot be detected by LEISS.

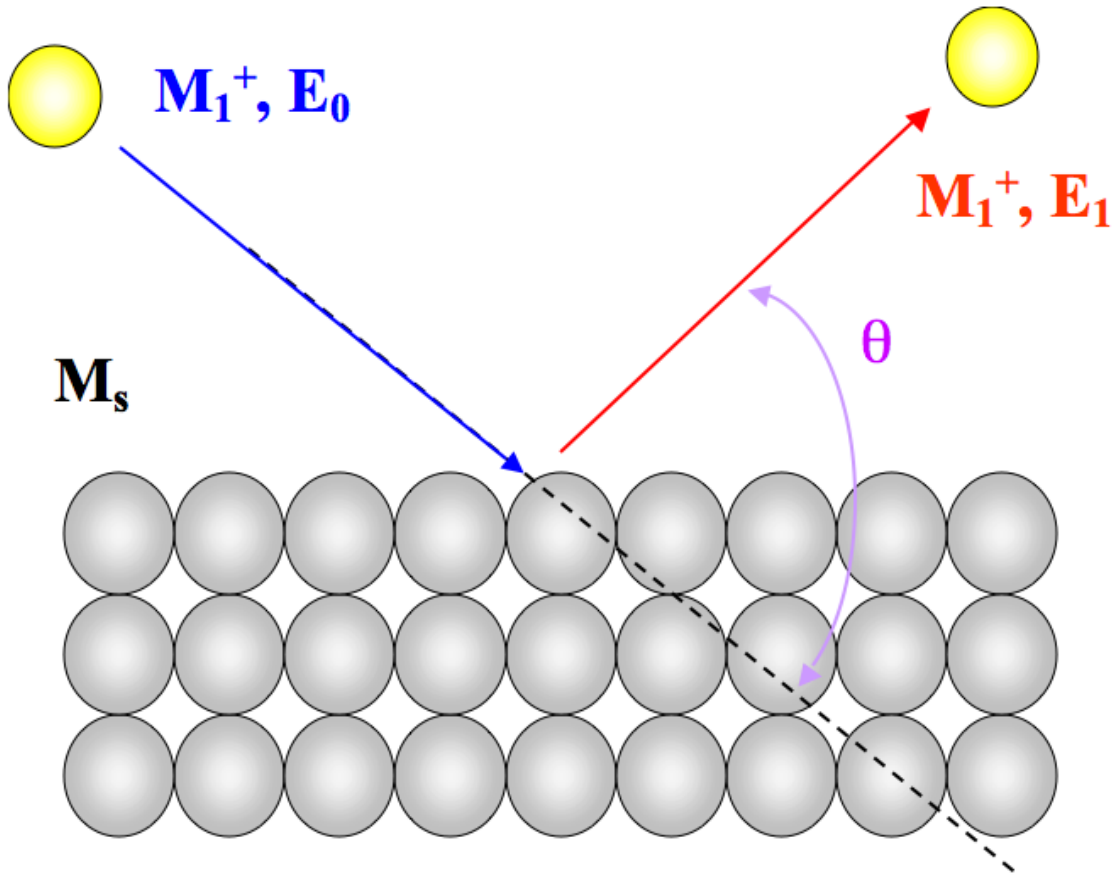

Figure 5. Schematic of binary collision in ISS technique.

Other than indicating the type of elements that are available on the surface, LEISS can also be used to measure the concentration of each element. The intensity or the peak area of the LEISS signal can be used for surface composition measurement. However, using the peak area in the determination of surface composition is more accurate. The following equation shows the relationship between surface concentrations, N_i and ion yield of the backscattered ions, S_i[69]:

$$S_i = \frac{I_p}{e}.t.\xi.R.\eta_i.N_i \tag{2.4}$$

where I_p is the primary ion beam current; e the elementary charge; t is the acquisition time; ξ is an instrumental factor including detector solid angle, detector efficiency and analyzer transmission; R is a factor, which takes the surface roughness and the shielding by neighboring atoms into account; and η_i is the elemental sensitivity factor.

Although equation (2.4) shows an elemental sensitivity factor in the quantitative measurement, it is useful to perform actual calibration against a reference sample because the elemental sensitivity factor is only available for certain combinations of elements, ion energies, and scattering angles. For LEISS calibration, a single crystal or a thick film of a fixed amount of pure elements being studied is measured under the same conditions. The peak intensity from each element will be the reference for quantitative measurements of elemental surface concentrations.

LEISS is extremely surface sensitive because of the low-energy ion beam, which allows the electron to obtain information of the topmost layer of the surface. Also, because of the large cross section for the interaction between the ion and the surface

atoms, the atoms on the first surface layer will screen the atoms from the second layer. For the studies that will be discussed in the next sections, a Perkin-Elmer ion gun and hemispherical analyzer were utilized for LEISS measurements. He^+ ions with energies ranging between 500 eV and 1000 eV have been employed.

Low Energy Electron Diffraction (LEED)

LEED is a surface characterization technique used in determining the crystal surface structure of a metal. Low-energy electrons (50 to 200 eV) impinge the surface of a metal and the diffracted electrons then travel to a fluorescent screen. Only elastically scattered electrons reach the fluorescent screen. Figure 6 shows a diagram of the LEED optics, including the hemispherical fluorescent screen that is incorporated with an electron gun at the central axis of the screen. The hemispherical screen contains three to four grids for screening out the inelastically scattered electrons. The sample is placed at the center of the hemispherical screen and the position can be optimized to obtain a LEED pattern on the fluorescent screen.

LEED is a surface-sensitive technique due to the low-energy electrons used in the process. Following the universal curve,[70] electrons with energies between 50 and 200 eV will penetrate only ~10 Å into the surface, providing surface sensitivity. Constructive or destructive interference patterns will form on the fluorescent screen from the scattered electron. Constructive interference occurs only when the Bragg condition is satisfied by the scattering[70]:

$$d = a\sin\theta = n\lambda\,, \tag{2.5}$$

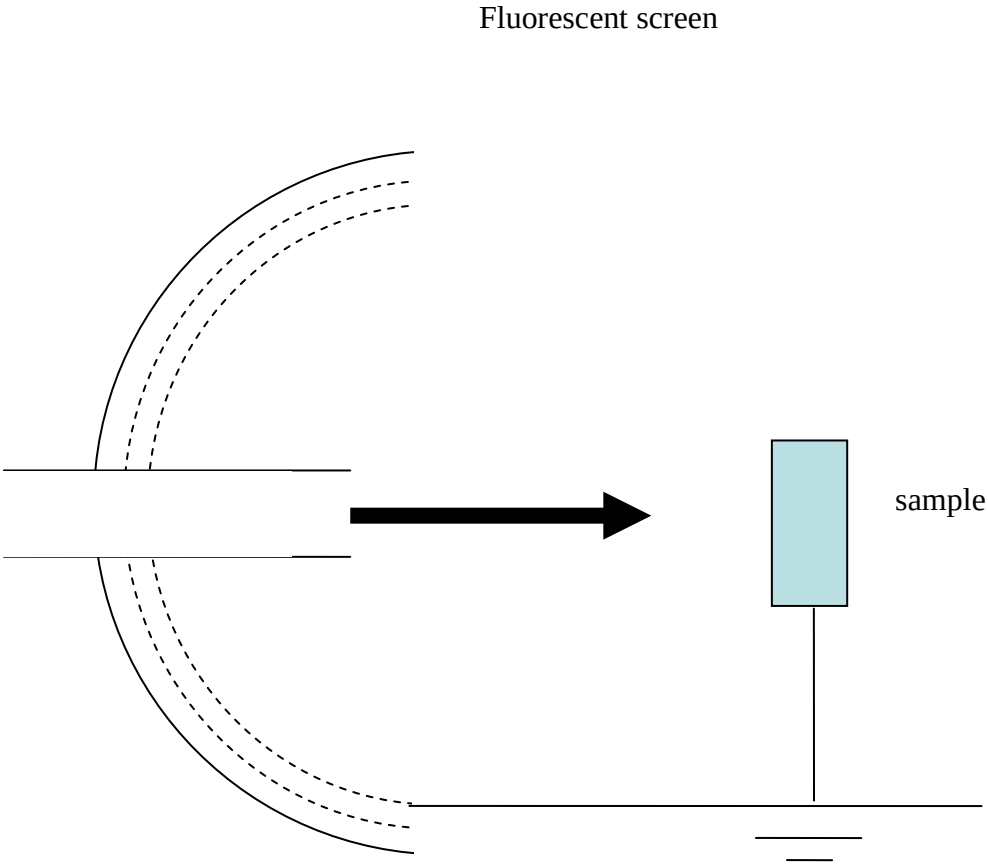

Figure 6. Diagram of LEED optics.

where *d* is the path difference of scattered electrons traveling toward a detector; *a* is the distance between two adjacent atoms; and θ is the angle between the scattered beam and the surface normal.

Temperature-Programmed Desorption (TPD)

TPD is a technique used to study the surface-adsorbate bonding strength and desorption kinetics. In a TPD experiment, the sample is heated at a constant heating rate while adsorbate with a specific mass desorbs into the gas phase and is monitored using a quadrupole mass spectrometer. The mass spectrometer is positioned near the front side of the sample in a direct line of sight.[71] The heating is restricted only to the sample; thus, avoiding desorption from other surfaces such as the sample holder. The amount of desorbed adsorbate with respect to time is recorded. The thermal desorption rates are described by the Polanyi-Wigner equation[75]:

$$r(\Theta) = -d\Theta / dt = v(\Theta)\Theta^n \exp[-E(\Theta) / RT], \tag{2.6}$$

where *r* is the desorption rate; Θ is the adsorbate coverage; *t* is the time; *v* is the pre-exponential factor for desorption; *n* is the order of desorption; *E* is the activation energy for desorption; *R* is the gas constant; and *T* is the temperature.

By analyzing a TPD spectrum, the relative surface coverage of the adsorbate, the activation energy for desorption, and the strength of the lateral adatom interactions can be estimated. Because the heating rate is linear, temperature and time are related by the following equation:

$$\beta = dT / dt. \tag{2.7}$$

Lateral interactions between adsorbates on the surface will dictate the desorption parameters mentioned previously.[75]

Scanning Tunneling Microscopy (STM)

Invented in early 1980s by Binnig and Rohrer[72], STM was used originally to image surface structures and also to probe the electrical properties of insulating materials sufficiently thin to allow electron tunneling.[72] This means that initially, STM was invented to image the structure of conducting materials or thin insulating materials and also to probe the local conductivity. However, because of the adaptability of the technique and the tunable low-electron energies used in the technique, STM has been used for real-space imaging with atomic resolution for many types of surfaces.

The basic principle of the STM technique involves electron tunneling, which is a phenomenon that occurs between two conductors separated by a thin insulating layer or potential barrier. In STM, the electron tunneling occurs between the tip and the sample surface as can be seen in Figure 7. To image the surface, a bias voltage is applied between the metal tip that is atomically sharp and a conducting sample surface. When the distance between the sample and the surface is a few Å, a tunneling current will flow between the tip and the surface. The piezoelectric tripod allows the positioning of the tip in the z-direction, and to also scan the tip across the surface in the x-direction and y-direction.[72] There are two types of scanning methods that can be used to image the surface. In constant height imaging (CHI), the height between the surface and the tip is kept constant and the change in the tunneling current is recorded. Another type of scanning method, constant current imaging (CCI), is used in the following studies and

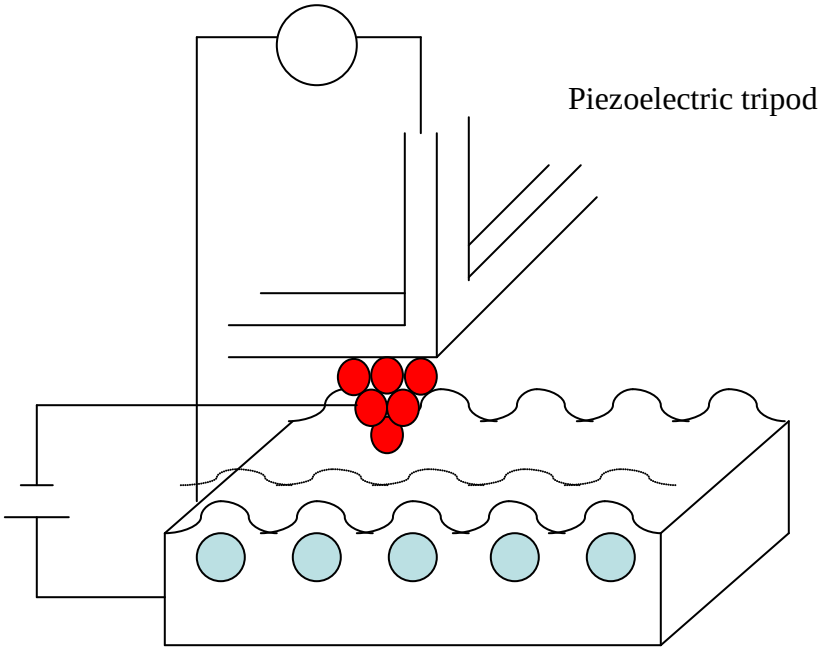

Figure 7. Diagram showing basic principle of STM.

discussed in the later sections. In CCI, the tunneling current between the tip and the sample is kept constant and the height of the tip varied to maintain a constant current.

Additional Techniques

A Mattson Cygnus 100 FTIR spectrometer was used for the infrared reflection absorption spectroscopy (IRAS) measurements of bimetallic clusters system (Au-Pd) and bimetallic planar system (Pd-Sn). An FEI Tecnai F20 G2 Transmitted Electron Microscopy (TEM) equipped with a field emission gun at a working voltage of 200 kV and energy dispersive spectrometer (EDS) and post-column Gatan Image filter was used for the study of bimetallic alloy electrocatalyst (Pt-Co). TEM imaging and EDX analysis were used to characterize the Pt-Co nanoparticles.

Electrochemistry Techniques and Procedures

One section in this dissertation will discuss the combined study of surface science (UHV) and electrochemistry (EC) of Pt-Co electrocatalyst. In this work, the UHV-EC studies of ORR catalysis on Pt-Co thin-film and cluster alloys will include the use of cyclic voltammetry (CV) and open circuit potential (OCP) analysis for electrochemical characterization and steady-state polarization for dissolution/corrosion studies using a stationary electrode of conventional dimensions. All potentials referenced are versus the reversible hydrogen electrode (RHE). High purity 0.1 M H_2SO_4 was used as the electrolyte and solutions were prepared using Millipore MilliQ water. UHP N_2 and O_2 were used for oxygen-saturated and deaerated conditions. Experiments were conducted using an EG&G PARC model 273 Potentiostat interfaced with a Windows PC running EChem software. A three-electrode assembly was employed. The reference

electrode and auxiliary electrode were separated from the working electrode by a fine glass frit. A custom Ag/AgCl reference was used with a 0.01mM NaCl filling solution.

Voltammetry

For voltammetric analysis, cyclic voltammetry (CV) was conducted according to the following procedure. Once the sample is introduced to the electrolyte, the system was allowed to remain at rest for 20 minutes to reach a steady state. Before any other experimental measurements took place, the open circuit potential (OCP) of the system was recorded for later analysis. Scans started at OCP and were scanned cathodically to hydrogen evolution and reversed. The upper switching potential, dependent upon the experiment, was set as OCP, 1.1 V, or 1.4 V. After the scans were complete, the OCP was recorded and the sample removed. CVs were collected at a scanning rate of 1 mV/s unless otherwise indicated.

OCP Analysis

To produce an electrode that operates closer to the theoretical potential for Pt will require more complete oxygen coverage of surface Pt sites. A fast and very simple method for determining the affinity of the electrode for increased oxygen coverage is to evaluate the OCP of the model alloy in an oxygen-saturated solution and compare the results from one Pt-Co model alloy composition to the next.

Samples and Dosers Preparations

Au-Pd/SiO_2

Au and Pd were evaporated from dosers made of high-purity Au and Pd wires (99.99%) wrapped around Ta filaments. The Au or Pd coverages were calibrated using

the distinct monolayer and multilayer TPD desorption features of the corresponding metal from a Mo substrate. XPS, LEIS, and AES data were also collected and used to monitor the coverage. Ultrahigh purity O_2 (99.98%, Matheson Tri-gas), CO (99.99%, Matheson Trigas), and deuterated ethylene (99%, Aldrich) were introduced through leak valves. The silicon dosers were wrapped with W wires and resistively heated during deposition. The details of the SiO_2 film preparation have been described previously.[76] The SiO_2 films were characterized with AES and XPS with the results showing that the SiO_2 films were fully oxidized. The SiO_2 film thickness was measured using the attenuation of the Mo substrate signals and the known mean-free paths of the X-ray and Auger electrons.

Pd-Sn/Rh(100)

The Rh(100) single crystal was cleaned by Ar^+ sputtering, oxidation (1200 K, 5×10^{-7} Torr O_2) and vacuum annealing (1400 K) cycles until no carbon and oxygen were detected in AES and a sharp (1 × 1) LEED pattern was observed. The Pd doser consisted of a tungsten filament about which a high-purity Pd wire was wound. The Sn doser was similarly constructed with the Sn wire source housed in a ceramic tube. Impurities in the evaporators were removed thoroughly by degassing prior to use. All metal depositions were performed with the sample at room temperature and the dosing rates calibrated by the break points in the LEIS, XPS, or AES data as a function of coverage. Carbon monoxide and oxygen (99.99%, Matheson Gas Products) were further purified by storage in a liquid-nitrogen reservoir prior to transfer to glass bulbs attached to the gas manifold.

AuPd(100)

The AuPd(100) bulk-alloy single crystal was purchased from Matek, and the ordered surface was obtained through repeated sputtering and annealing cycles (E = 500 eV, I = 0.38 μA, Ar^+ sputtering at room temperature for 20 min, and annealing at ~550 °C for 15 min). The sample was annealed without sputtering at 550 °C for 30 min before imaging and was allowed to cool to room temperature without deliberate temperature quenching. The surface temperature was measured optically by infrared pyrometry.

Pt-Co Films and Clusters

Thin films were prepared by physical vapor deposition in an ultrahigh vacuum (UHV) as described previously.[77] A doser was constructed by tightly winding wires of the Pt and Co metals in small segments around a Ta filament. The filament was heated resistively at a current sufficiently high to initiate sublimation of subject metals onto a cold (Ru or Mo) substrate. For Pt-Co clusters, Pt and Co metals were deposited onto a highly oriented pyrolitic graphite (HOPG) sample with a submonolayer amount of Pt or Co to achieve clusters of Pt-Co alloy.

3. BIMETALLIC CLUSTERS MODEL SUPPORTED CATALYST CHARACTERIZATION*

Preparation and Characterization of Silica Supported Au-Pd Model Catalysts

Au−Pd mixed-metal catalysts are currently used for a variety of reactions, including vinyl acetate synthesis,[78-81] acetylene hydrogenation[82]/trimerization,[83-85] and CCl_2F_2 hydrodechlorination.[86,87] An atomic-level characterization of the surface composition, morphology, physical/electronic structure, and chemisorptive/catalytic properties of oxide-supported Au-Pd model catalysts is critical to understanding the role Au plays in enhancing the catalytic properties of Pd. Stable bulk alloys[88-95] and thin-film alloys of Au-Pd grown on low index single crystals[45,96-101] have been extensively studied using various surface sensitive techniques. Preferential segregation of Au at the surface has been observed by Auger electron spectroscopy (AES),[88,89,91] X-ray photoelectron spectroscopy (XPS),[91,92] and low energy ion scattering spectroscopy (LEIS).[90,92,96,99,100,102] Electronic perturbation of Au and Pd due to the sp and d band charge redistribution or orbital hybridization has been proposed based on studies by X-ray absorption near-edge spectroscopy (XANES),[95] ultraviolet photoelectron spectroscopy (UPS),[97] XPS,[94-96] and computational modeling.[94,95,97] Using scanning

*Reprinted with permission from "Preparation and Characterization of Silica Supported Au-Pd Model Catalysts" by K. Luo, T. Wei, C.-W. Yi, S. Axnanda, and D. W. Goodman, *Journal of Physical Chemistry B* **2005,** *109*, 23517-23522, Copyright [2005] by American Chemical Society

tunneling microscopy (STM), Behm and co-workers carried out a detailed structural study of the surface of Pd/Au(111).[45] With supporting infrared data, these authors observed a marked ensemble effect with respect to adsorption of CO and H_2. Our group has recently studied alloy surfaces of Au-Pd/Mo(110),[43] Pd/Au(100),[24] and Pd/Au(111),[24] characterizing them with LEIS, XPS, AES, infrared reflection absorption spectroscopy (IRAS), and temperature programmed desorption (TPD).[43] The formation of stable AuPd surface alloys and surface segregation of Au were observed after sequential deposition of Au and Pd with subsequent annealing. A special surface ensemble consisting of isolated Pd sites was identified by CO-TPD and CO-IRAS.[43] Moreover, an ensemble consisting of noncontiguous Pd dimers on Pd/Au(100) was shown to exhibit an unusually high reactivity (turnover frequency or TOF) for vinyl acetate synthesis.[24] Several studies have addressed oxide-supported Au-Pd catalysts.[98,103-105] The structural properties of silica supported Au-Pd catalysts prepared from colloid precursors were studied using X-ray diffraction (XRD), extended X-ray absorption fine structure (EXAFS), and XANES.[103-105] Davis et al. concluded that Pd atoms decorate a core of Au atoms using EXAFS.[103] Utilizing similar techniques, Lamb et al. also concluded that a partial monolayer of Pd atoms decorates a Au-rich core.[104] On the other hand, Kaszkur et al.[105] used XRD to show that a Pd-decorated surface induced by oxygen adsorption can be transformed to a Au-decorated surface with a pulse of H_2. Related infrared studies from our laboratories of CO adsorption on alumina supported Au−Pd and Cu−Pd clusters[98] suggested that a geometrical rather than a ligand effect was dominant. The present investigation is an extension of our previous studies of

planar surfaces to silica-supported Au-Pd bimetallic clusters.[24,43] LEIS, IRAS, and TPD with CO as a probe are utilized to systematically investigate the cluster surface composition and structure. To highlight the effects of alloying on catalysis, ethylene dehydrogenation was investigated and a structure–reactivity correlation obtained.

Growth of Au-Pd Alloy Clusters

The experiments were carried out in two ultrahigh vacuum (UHV) chambers. One chamber was equipped with LEIS, XPS, AES, TPD, and low energy electron diffraction (LEED) with a base pressure of 2×10^{-10} Torr. The Mo(112) single crystal was mounted to copper leads by high purity Ta wires. The sample could be heated to 1500 K resistively or to 2400 K by an e-beam and cooled to 90 K by a liquid nitrogen reservoir attached to the copper leads. The temperature was measured using a W-5%Re/W-26%Re (C-type) thermocouple spot-welded to the backside of the sample. LEIS experiments were carried out with a He^+ beam with energy of 1050 eV and an incident angle of ~45° from the surface normal. The TPD apparatus utilizes a line-of-sight quadrupole mass spectroscopy (QMS) with a differential pumped aperture and a linear heating ramp of 5 K/s. The second chamber was equipped with AES, IRAS, and TPD and maintained at a base pressure of 1×10^{-10} Torr. The substrate Mo(110) single crystal could be heated as described above. The substrate can be cooled to 80 K due to the slight difference of the probe design and sample mounting. The IR cell was equipped with CaF_2 windows and could be pressurized to several Torr. The infrared spectra were collected while exposing the sample to 1×10^{-8} Torr CO, i.e., saturation coverage, at various substrate temperatures.

Au and Pd were evaporated from dosers made of high-purity Au and Pd wires (99.99%) wrapped around Ta filaments. The Au or Pd coverages were calibrated using the distinct monolayer and multilayer TPD desorption features of the corresponding metal from a Mo substrate. XPS, LEIS, and AES data were also collected and used to monitor the coverage. Ultrahigh purity O_2 (99.98%, Matheson Tri-gas), CO (99.99%, Matheson Trigas), and deuterated ethylene (99%, Aldrich) were introduced through leak valves. The silicon dosers were wrapped with W wires and resistively heated during deposition. The details of the SiO_2 film preparation have been described previously.[76] The SiO_2 films were characterized with AES and XPS, with the results showing that the SiO_2 films were fully oxidized. The thickness of the SiO_2 films was measured using the attenuation of the Mo substrate signals and the known mean free paths of the X-ray and Auger electrons.

The growth and characterization of nanosized clusters of Au and Pd on SiO_2 surfaces have been discussed in the literature.[76,106-109] In general, Pd clusters are more highly dispersed for a given coverage and are more sinter-resistant compared to Au.[107-109] In the present study, amorphous SiO_2 films (2-5 nm) were used to support Au-Pd clusters. To synthesize the clusters, 1.0 monolayer (ML) Pd was first deposited on SiO_2 and then annealed to 800 K for 10 min. Subsequently, Au was deposited at 300 K and annealed to 800 K for 10 min. LEIS was used to characterize the surface composition and morphology for each deposition condition, with all spectra being collected with a substrate temperature of 300 K. The LEIS spectrum in Figure 8a is that following the deposition of 1.0 ML Pd on the SiO_2 film and a subsequent 800 K anneal. Three LEIS

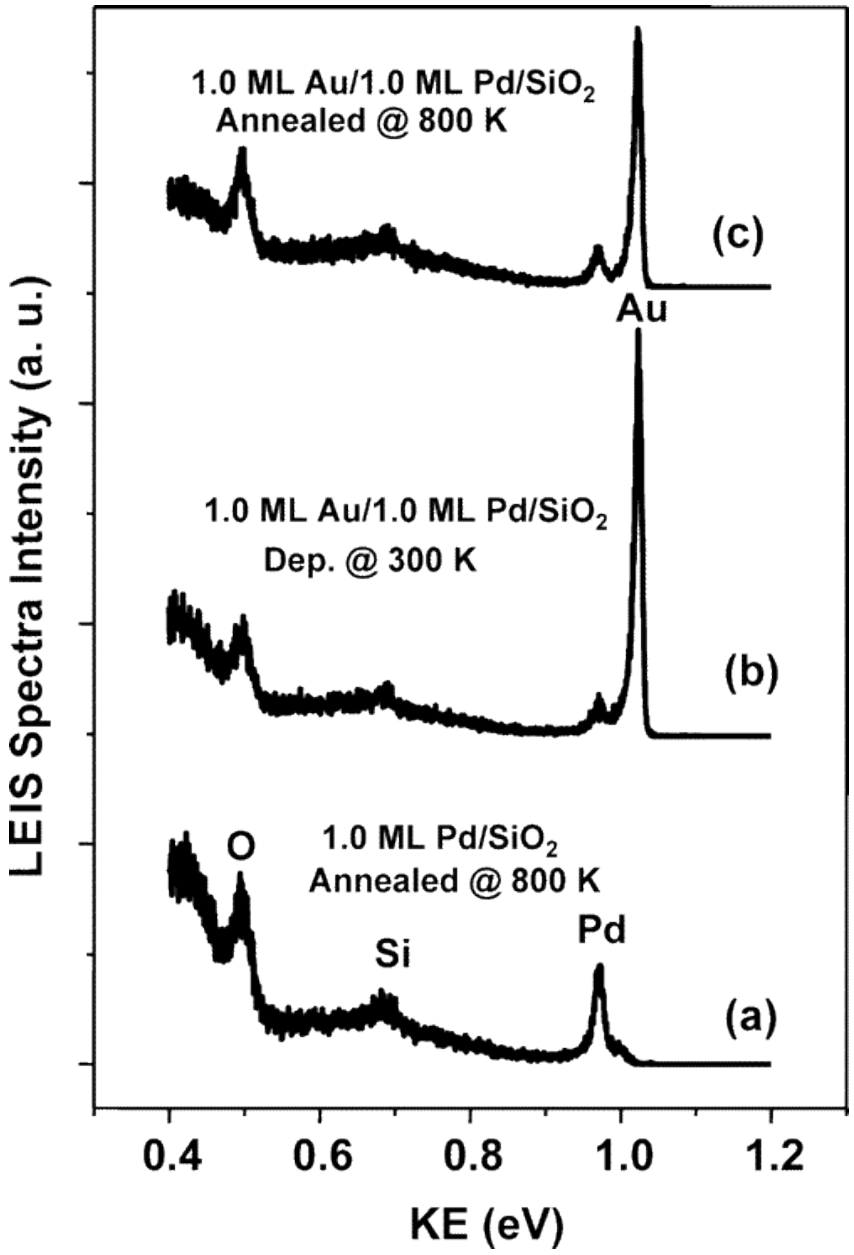

Figure 8. LEIS spectra of (a) 1.0 ML Pd/SiO_2 after a 800 K anneal; (b) after deposition of 1.0 ML Au deposition 300 K on 800 K preannealed 1.0 ML Pd/SiO_2; and (c) 1.0 ML $Au/1.0$ ML Pd/SiO_2 annealed to 800 K. All spectra were collected at 300 K.

features with kinetic energy (KE) at 0.45, 0.70, and 0.97 keV are assigned to O, Si, and Pd, respectively. A Mo feature at 0.94 keV was not present, consistent with the Mo substrate being fully covered by the SiO_2 thin film. Upon deposition of 1.0 ML Au at 300 K, the intensity of the Pd feature dramatically decreases by ~65%. Concomitantly, a large Au scattering feature appears at 1.03 keV. The significant decrease of the Pd feature upon deposition of Au indicates that a significant amount of the deposited Au decorates the Pd clusters. Upon annealing 1.0 ML Au/1.0 ML Pd/SiO_2 to 800 K, the Pd feature intensity remained essentially constant; however, the Au intensity decreased by ~30%, likely due to alloying of the Au with Pd and/or sintering of Au-only clusters. Similar LEIS measurements were carried out by reversing the deposition sequence, i.e., 1.0 ML Pd/1.0 ML Au/SiO_2 (Au deposited first) (data not shown here). The Au scattering intensity was unchanged following Pd deposition, likely because only a small fraction of the added Pd nucleates on the Au clusters, with the remainder forming Pd-only clusters.[108,109] Based on data above, the deposition of Pd first is clearly preferable for the synthesis of more uniform Au-Pd alloy clusters.

LEIS Au-Pd scattering data for Au-Pd silica supported clusters, i.e., 1.0 ML Au/1.0 ML Pd/SiO_2, and a planar Au-Pd surface, i.e., 5.0 ML Au/5.0 ML Pd/Mo(110), are shown in Figure 9 as solid and dashed lines, respectively. Note that each of these was annealed to 800 K prior to acquisition of the LEIS spectrum at 300 K. The preparation details of the planar 5.0 ML Au/5.0 ML Pd/Mo(110) surface are described elsewhere.[43] The data of ref [43] show the planar surface composition consists of ~20% Pd and ~80% Au. For 1.0 ML Au/1.0 ML Pd/SiO_2, the LEIS data show Pd to have a similar relative

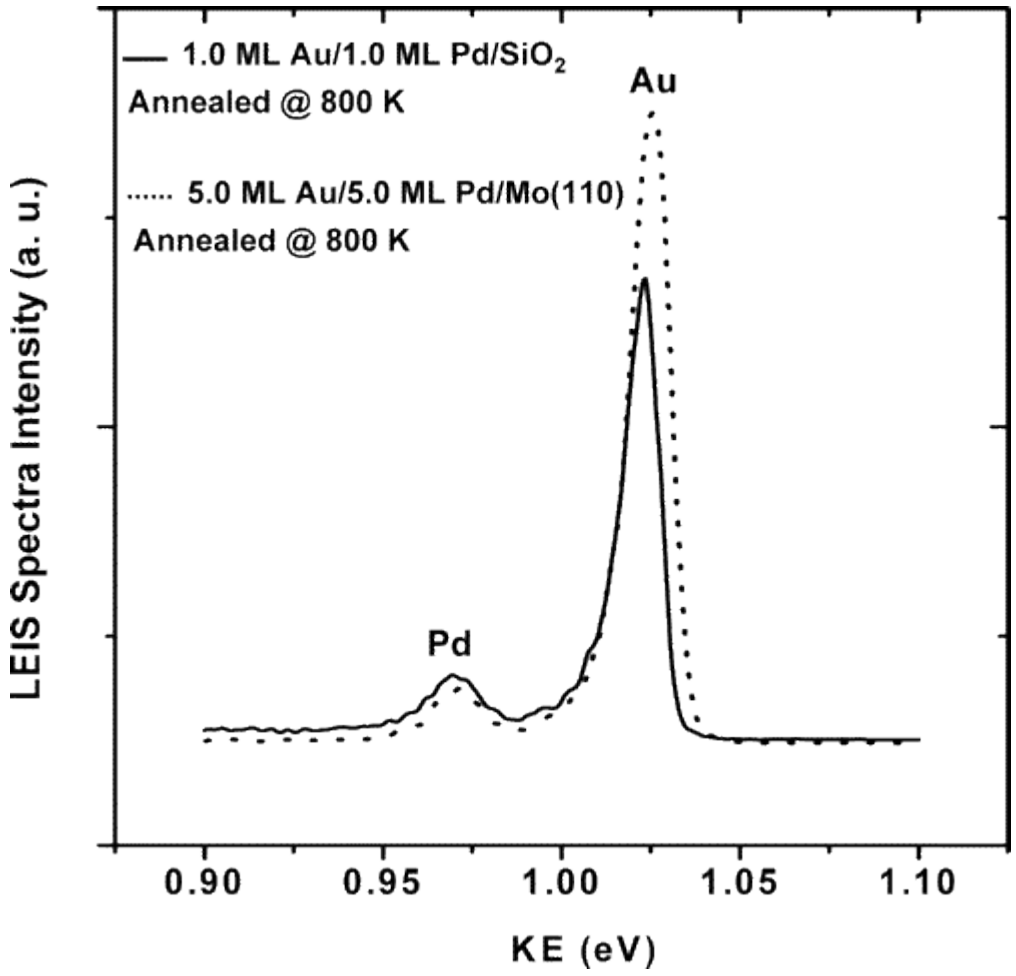

Figure 9. LEIS data for 1.0 ML Au/1.0 ML Pd/SiO_2 after 800 K annealing (solid line) and 5.0 ML Au/5.0 ML Pd/Mo(110) after 800 K annealing (dashed line). All spectra were collected at 300 K.

intensity compared to the extended Au-Pd surface spectrum. The Au LEIS spectral intensity for the Au-Pd clusters, however, is significantly less in Figure 9 compared to the Au LEIS signal for the extended Au-Pd surface, implying that the Au-Pd cluster surfaces are more Pd-rich compared to the corresponding Au-Pd extended surface. Normalization of the Pd LEIS intensity suggests that the cluster surface concentration consists of ~33% Pd and ~67% Au. We note also that XPS of supported Pd clusters on the silica films here after annealing to temperatures as high as 800 K indicated no silicide formation as previously reported for Pd growth on monolayer SiO_2.[107,108]

In previous studies of Au-Pd surface alloys on Mo(110) surface, CO TPD was used to distinguish isolated Pd sites from Pd bridging/three-fold hollow sites. This same methodology was used in the present studies for the silica-supported Au–Pd clusters. TPD from a saturated coverage of CO (1.0 Langmuir, L) was carried out for the bare SiO_2 and SiO_2-supported Au-Pd clusters, each annealed to 800 K. In Figure 10, CO TPD spectra for the bare SiO_2 surface, 1.0 ML Pd/SiO_2, and 1.0 ML Au/SiO_2 are shown in Figures 11a, Figure 10b, and Figure 10c, respectively. In Figure 10a, for CO on bare SiO_2, a single broad low-temperature feature centered at 135 K was observed from CO adsorbed on the SiO_2 support. In Figure 10b for CO/1.0 ML Pd/SiO_2, additional features centered at 465, 320, and 250 K were observed. Based on previous studies of CO TPD on Pd low index single-crystal surfaces and oxide-supported clusters,[43,98,110-115] the 465 K feature is assigned to CO adsorbed on Pd three-fold hollow sites. The features at 250 and 320 K are likely due to CO adsorbed on atop Pd sites at various Pd facets, e.g., Pd(100), Pd(111), corners/edges, etc. The desorption features between 320 and 465 K

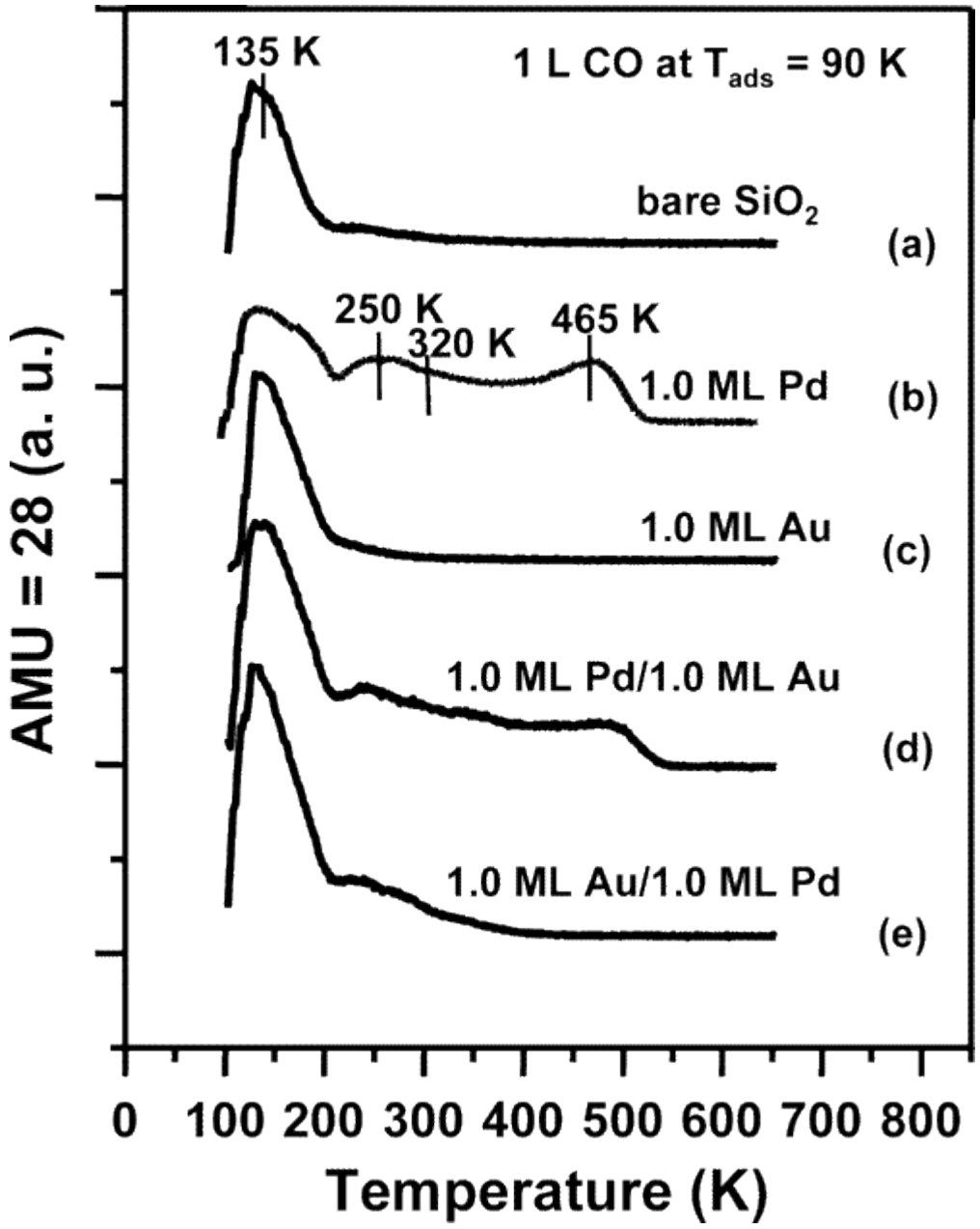

Figure 10. TPD spectra of CO: (a) with 1.0 L CO exposure at 90 K on bare SiO_2; (b) 1.0 ML Pd/SiO_2; (c) 1.0 ML Au/SiO_2; (d) 1.0 ML Pd/1.0 ML Au/SiO_2; and (e) 1.0 ML Au/1.0 ML Pd/SiO_2.

are assigned to CO on Pd bridging sites, in agreement with the studies of Carlson et al., of CO adsorption on Pd/Al_2O_3 surfaces.[112] Figure 10c shows CO TPD from 1.0 ML Au/SiO_2, with no strong desorption features apparent above 200 K, indicating weak CO bonding as reported previously.[109,116] In Figure 10d and Figure 10e, CO TPD from 1.0 ML Pd/1.0 ML Au/SiO_2 and 1.0 ML Au/1.0 ML Pd/SiO_2 are shown, respectively. In Figure 10d, a slight decrease of CO desorption is apparent for all the features above 200 K, compared to Figure 10b of CO/1.0 ML Pd/SiO_2. In comparison to Figure 10a,b,c, an increase in intensity for the low temperature feature at 135 K was observed due to the additional weakly bonded CO on Au. In this deposition sequence, the surface exhibits the primary CO desorption features associated with pure Pd clusters, i.e., 1.0 ML Pd/SiO_2, and is consistent with the primary nucleation of Pd-only, rather than Au-Pd clusters. However, in Figure 10e, both the high temperature feature at 465 K and the features between 320 and 465 K completely disappear for 1.0 ML Au/1.0 ML Pd/SiO_2. The intensity of the atop Pd sites at 250 and 320 K remains with ~30% attenuation. These results are significantly different from those of Figure 10b, implying considerable alloying with Au deposition onto pre-deposited Pd clusters and a subsequent anneal.

Surface Pd Sites

LEIS, CO-TPD, and CO-IRAS were combined to characterize the compositional and structural properties of the Au-Pd alloy clusters. First, LEIS experiments of various Au coverages (0.1-1.0 ML) on 1.0 ML Pd/SiO_2 were carried out. Note that the surface was annealed to 800 K for 10 min after each Au deposition and all LEIS spectra were collected at 300 K. Using the same method used to acquire the data of Figure 8 and

Figure 9, the surface concentration of Pd on Au-Pd alloy clusters was measured with various Au coverages and plotted as a function of the Au/Pd atomic ratio in the filled square data of Figure 11. The dashed line is the calculated Pd concentration, assuming that the surface composition reflects the bulk composition. The concentration of Pd at the cluster surface decreases more rapidly than does the dashed line data, indicating that the cluster surfaces are Au-rich compared to the bulk. For comparison, the surface concentration of Pd for Au-Pd/Mo(110) planar surfaces as a function of the Au/Pd atomic ratio has been extracted from ref [43] and plotted in Figure 11 as the filled circle data. For Au-Pd planar surfaces, segregation of Au to the surface as a function of the Au/Pd ratio is much more significant. For example, for a Au/Pd ratio atomic ratio of ~0.11, only ~60% Pd is observed at the surface, whereas for a Au/Pd ratio of 1:1, the surface is only ~20% Pd. In any case, for Au-Pd clusters and extended surfaces, the outermost surface layer is enriched significantly in Au, with the surface concentration of Pd on Au-Pd clusters being greater than that for planar surfaces with an identical Au/Pd bulk composition.

To further characterize the surface composition, CO TPD experiments were carried out to probe the surface structure and absorption sites on 0.1-1.0 ML Au/1.0 ML Pd/SiO_2. Note that each surface was annealed to 800 K for 10 min, then cooled to 90 K prior to CO adsorption and TPD. In Figure 12, CO TPD spectra are shown as a function of Au coverage. As discussed earlier, Figure 12a exhibits multiple CO adsorption features on Pd: atop, bridging, three-fold hollow sites, and support-related sites for 1.0 ML Pd/SiO_2. With a very small amount of Au deposition, e.g. 0.1 ML, an

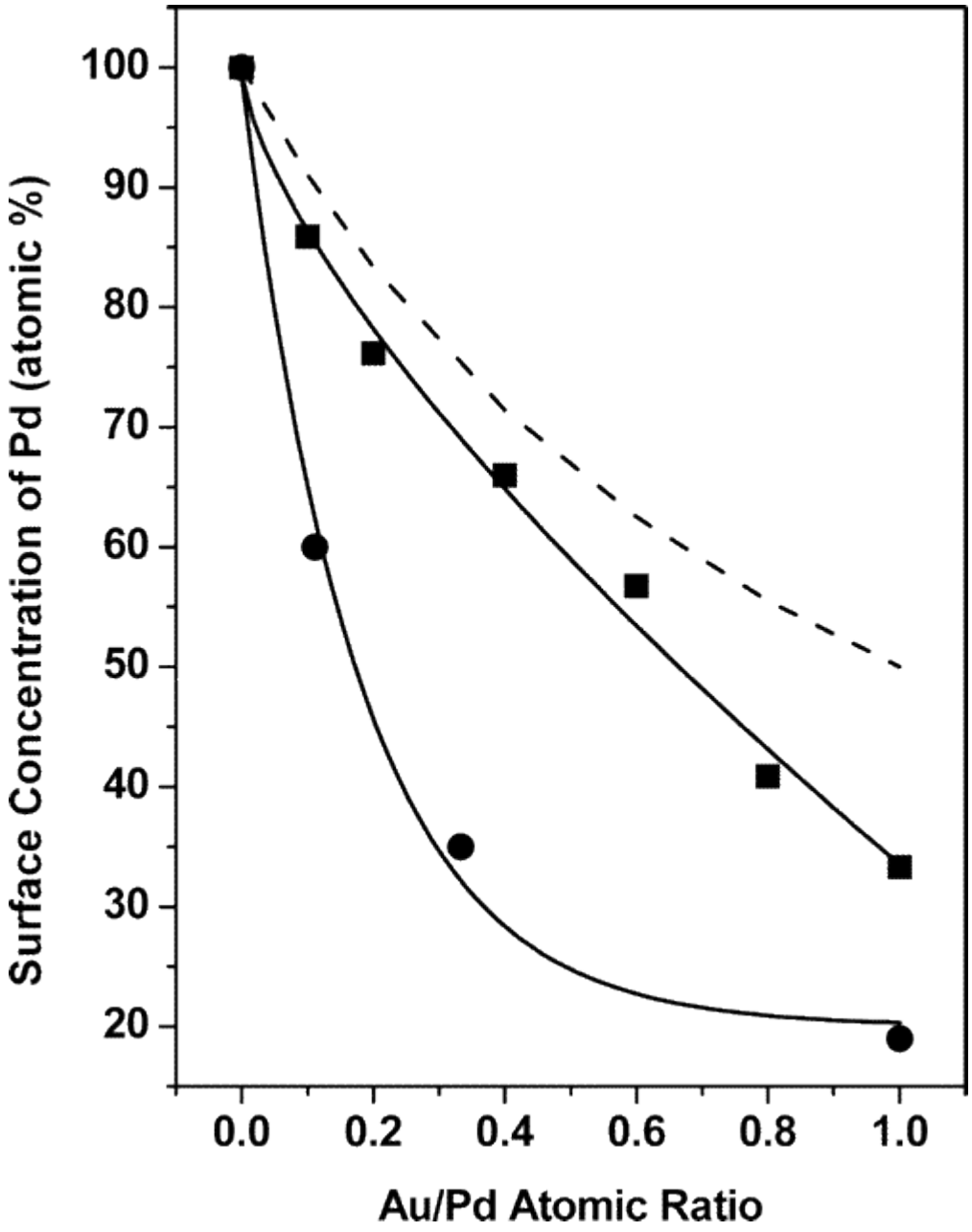

Figure 11. Surface concentration of Pd as a function of Au/Pd atomic ratio for various Au coverage (0.1-1.0 ML) on 1.0 ML Pd/SiO_2 after 800 K annealing (■); for Au-Pd/Mo(110) after 800 K annealing (●).

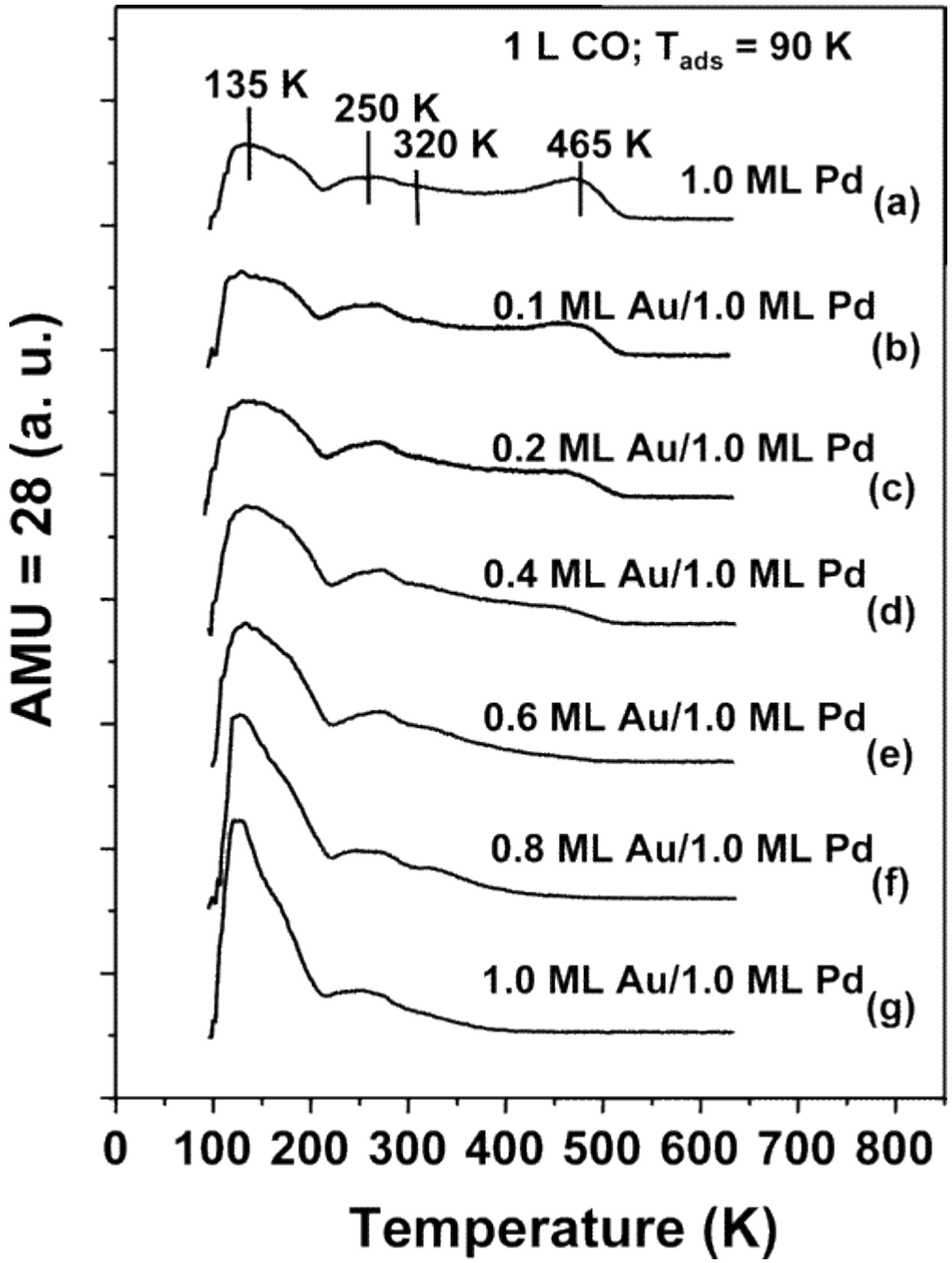

Figure 12. CO TPD with 1.0 L CO exposure at 90 K of different Au coverage (0.1-1.0 ML) on 1.0 ML Pd/SiO_2.

obvious signal reduction was detected for the three-fold hollow sites at 465 K in 5b, and a slight intensity increase for the atop site features at 250 and 320 K. Simultaneously, an increase in the low temperature desorption feature at 135 K was observed due to the addition of Au. Considering the relatively large density of Pd clusters,[107,108] higher sticking coefficients of Au on Pd versus Au on silica and the low Au coverage of 0.1 ML, we assume that all Au atoms nucleate on Pd clusters to form alloy clusters after annealing. Alloying leads to the following: (a) the formation of 85% Pd versus 15% Au on the alloy cluster surfaces (from the LEIS data in Figure 11 with a Au/Pd ratio of 0.1); (b) diminution of the Pd three-fold hollow site density; and (c) an increase in the density of the Pd atop sites. As the Au coverage increases from Figure 12b to Figure 12d, the density of the Pd three-fold hollow features progressively decreases. These features completely vanish at a Au coverage of 0.6 ML in Figure 12e. In this transition, the signal intensity of the feature between 320 and 465 K, assigned to Pd bridging sites, also gradually decreases at 0.6 ML Au coverage. However, the Pd atop features at 250 and 320 K remain unchanged up to 0.6 ML Au. With increasing Au coverage to 1.0 ML, the bridging sites completely disappear and the intensity of the atop feature decreases ~30%. As a result, the loss of Pd bridging/three-fold hollow sites and the prevalence of atop sites are apparent on the Au-Pd alloy cluster surfaces.

IRAS studies addressing the surface morphology of the Au-Pd clusters were first carried out by adsorbing CO on 1.0 ML Au/SiO_2/Mo(110). The spectra as a function of temperature are shown in Figure 13a. Only a single, sharp feature at 2109 cm^{-1} is evident at 80 K, and is assigned to CO on Au atop sites.[98,116] The intensity of this feature

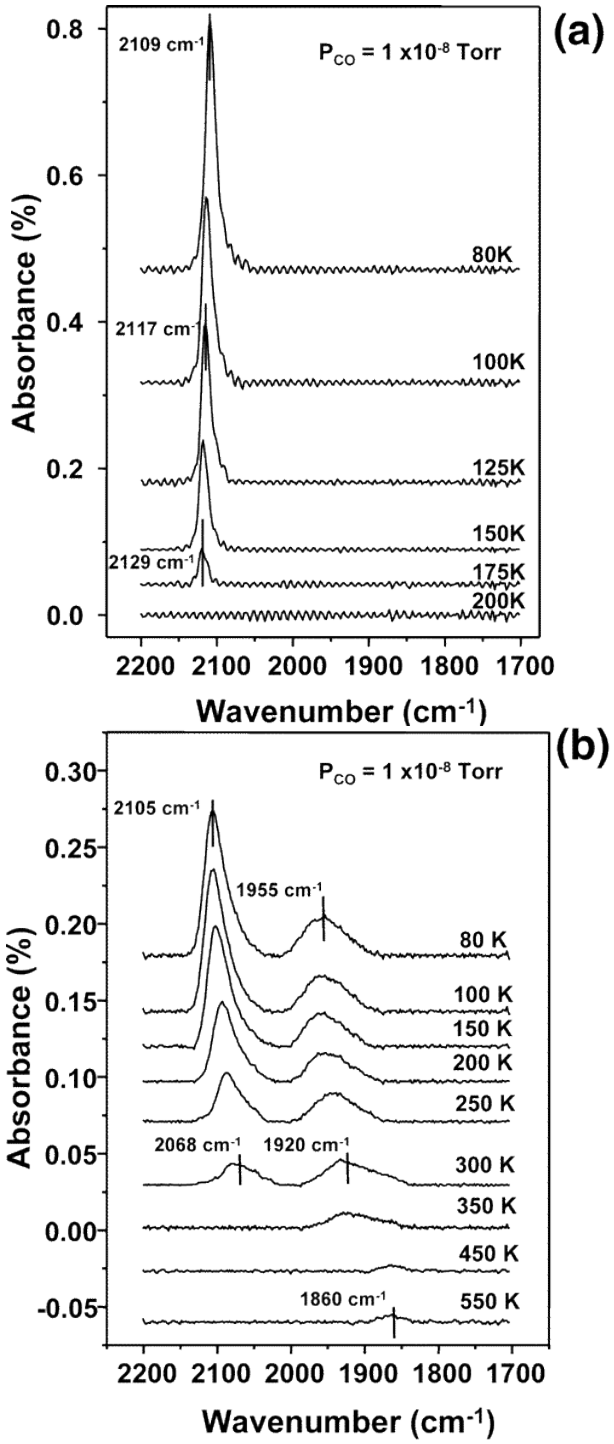

Figure 13. IRAS spectra of CO adsorption: (a) on 1.0 ML $Au/SiO_2/Mo(110)$ as a function of temperature; and (b) on 1.0 ML $Pd/SiO_2/Mo(110)$ as a function of temperature.

decreases with an increase temperature, and its position blue shifts to 2129 cm^{-1} at 175 K; at 200 K the intensity of this feature vanishes. This behavior parallels closely the TPD results of Figure 10c, where no CO desorption was detected above 200 K. The blue shift for the Au clusters is decidedly different from the red-shift for CO adsorption on Pd clusters.[98] The blue shift is characteristic of CO on Au clusters and accordingly can be used to identify Au-only clusters. In Figure 13b, IRAS spectra of CO adsorption on 1.0 ML Pd/SiO_2 are shown as a function of temperature. A relatively narrow feature at ~2105 cm^{-1} and a broad feature extending from 2000 to 1875 cm^{-1} are apparent at 80 K. Extensive studies have been carried out with IRAS of CO adsorption on Pd(111), Pd(100), and oxide-supported nanosized Pd particles.[98,110,111,114,115,117] From studies on Pd(111) and Pd(100), three CO adsorption sites, atop, bridging, and three-fold hollow sites are observed with CO stretching frequency in the ranges 2090 to 2120 cm^{-1}, 1895−2000 cm^{-1}, and 1830−1920 cm^{-1}, respectively. For alumina- or silica-supported Pd clusters,[98,111,113,114,117,118] the CO adsorption sites and their corresponding frequencies are in agreement with previous work on Pd(100) and Pd(111). Accordingly, the high-frequency feature at ~2105 cm^{-1} is assigned to CO on Pd atop sites and the broad band at 2000 cm^{-1} −1875 cm^{-1}, to CO on bridging and three-fold hollow sites.[98,111,113,114,117,118] With increasing temperature, the atop feature red shifts to 2068 cm^{-1} at 300 K; the signal intensity gradually decreases and completely vanishes at 350 K. Concomitantly, the intensity of CO on bridging/three-fold hollow sites also decreases. The peak position red shifts to ~1860 cm^{-1} before the signals completely disappear above 550 K. Our data closely agree with the previously reported IRAS data for small Pd particles grown on

SiO_2 and Al_2O_3.[98,111,114,117,118] The CO adsorption sites and the corresponding desorption temperatures agree with the CO TPD results discussed above. In Figure 14, the IRAS spectra of CO absorbed on 1.0 ML Au/1.0 ML Pd/SiO_2/Mo(110) are presented as a function of temperature. At 80 K, a sharp feature at 2112 cm^{-1} with a small shoulder at lower frequency side is apparent, with no features corresponding to CO adsorbed on Pd in bridging or three-fold hollow sites. As the temperature is increased, the primary feature blue shifts to 2122 cm^{-1} at 200 K and completely vanishes at 250 K. According to the distinctive blue shift exhibited by CO stretching frequency on Au clusters upon annealing in Figure 13a and the complete loss of signal intensity at 250 K, we conclude that the feature at 2112 cm^{-1} is from CO adsorbed on Au atop sites. The shoulder observed on the low-frequency side of the 2112 cm^{-1} peak at 80 K is clearly evident at 150 K with a stretching frequency at 2086 cm^{-1} and distinctly resolved from the Au atop sites at 200 K. Furthermore, it is the only CO feature present at 250 K. In the inset of Figure 14, this feature can still be seen at 2083 cm^{-1} at 300 K. This unique feature, with a frequency of ~20 cm^{-1} lower than CO adsorbed on regular Pd atop sites on Pd single-crystal substrates and oxides supported clusters,[43,98,110,111,114,115] is characteristic of a Au-Pd alloy cluster surface and has been observed for Au-Pd planar alloy surfaces and for alumina-supported Au-Pd clusters.[43,98] No significant frequency shift was observed over the entire temperature range investigated. With consideration of enhanced surface segregation of Au and the characteristic atop Pd sites observed by CO TPD, the Pd atoms are believed to be surrounded by Au atoms, forming isolated Pd sites on the alloy

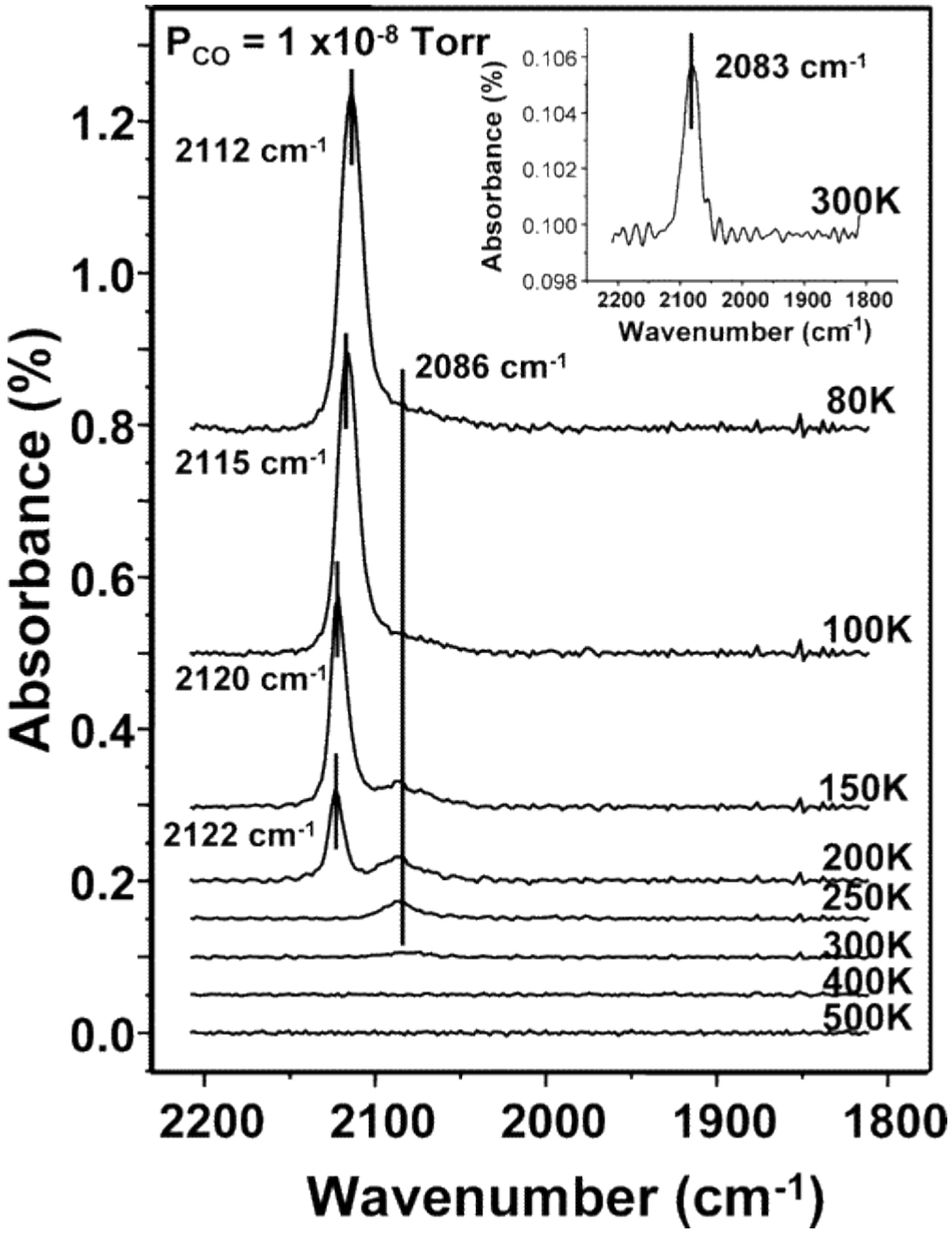

Figure 14. IRAS spectra of CO adsorption on 1.0 ML Au/1.0 ML Pd/SiO_2/Mo(110) as a function of temperature.

clusters of 1.0 ML Au/1.0 ML Pd/SiO_2. The red shift can be due either to stronger bonding of CO to the isolated Pd or to reduced lateral destabilization of CO on the surrounding Au atoms. The apparent stabilization of the CO/Au feature in the IRAS data of Figure 14 compared with the CO/Au-only feature of Figure 13a may be a consequence of a small electronic effect of Pd on the surrounding Au atoms.

Correlation of Surface Structure and Reactivity

To probe the surface structure of the Au-Pd alloy clusters as well as their catalytic reactivity, a TPD study of deuterated ethylene (C_2D_4) adsorption and dehydrogenation on the silica-supported Pd and Au-Pd alloy clusters was carried out. In Figure 15, the TPD spectrum acquired following 2.0 L C_2D_4 adsorption on 1.0 ML Pd/SiO_2/Mo(112) is shown as the open circle line. The C_2D_4 spectra are shown after subtraction of background contributions below 170 K. A broad feature is observed with a desorption temperature peak maximum at 250 K, assigned to contributions from π-bonded and di-σ bonded C_2D_4.[119-121] The broadness of the desorption features is likely due to the inhomogeneity of adsorption sites on the clusters. [119-123] The data shown in the solid circles were acquired after the addition of 0.2 ML Au to the 1.0 ML Pd/SiO_2 clusters followed by a 800 K anneal. Compared to C_2D_4/1.0 ML Pd, the C_2D_4 TPD shows a reduction in the signal intensity and a shift in the peak desorption maximum from 250 to 230 K. These changes are attributed to dilution of the Pd surface concentration upon Au deposition. With 1.0 ML Au deposition to 1.0 ML Pd/SiO_2 and annealing, a significant further loss of C_2D_4 desorption intensity is obvious, together

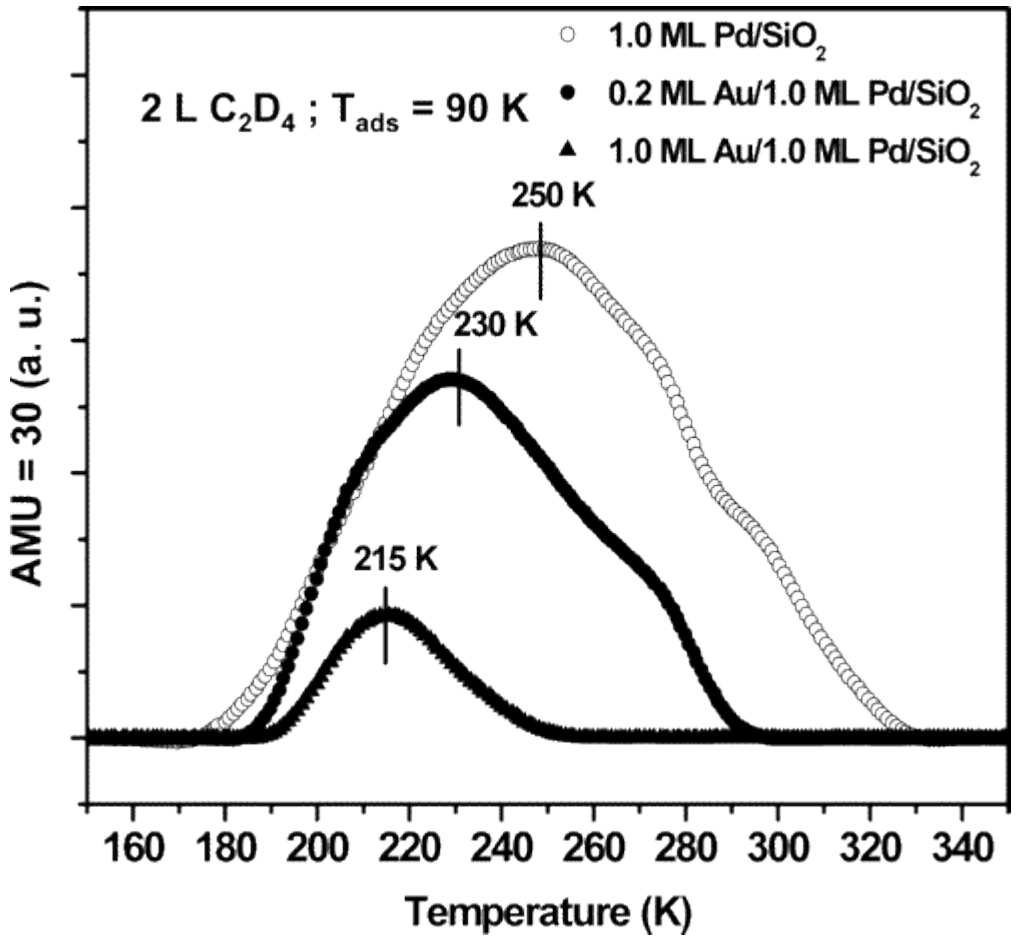

Figure 15. TPD of C_2D_4 with 2.0 L C_2D_4 exposure at 90 K on 1.0 ML Pd/SiO_2 (○); 0.2 ML Au/1.0 ML Pd/SiO_2 (●); and 1.0 ML Au/1.0 ML Pd/SiO_2 (▲).

with a desorption peak maximum shift to 215 K. These data indicate that the addition of Au to Pd clusters leads to attenuation of the stronger di-σ bonded C_2D_4 requiring adjacent Pd atoms. C_2D_4, in contrast, bonds primarily to isolated Pd sites via π-bonding. These results are in agreement with the CO-IRAS and CO-TPD data discussed above.

D_2 formation from ethylene dehydrogenation was also monitored with TPD. Pd-catalyzed ethylene dehydrogenation has been studied extensively on Pd(111), Pd(100), and alumina-supported Pd cluster surfaces.[119-121] From these studies, a strong interaction between ethylene adsorbates and two adjacent Pd atoms via di-σ bonding is purported to be responsible for ethylene dehydrogenation. Ethylidyne (≡C−CH_3) and vinylidene (=CH−CH_2) species are proposed to be the reaction intermediates on Pd(111) and Pd(100) facets, respectively, with the reaction site requiring three-fold hollow and bridging Pd sites. In Figure 16, D_2 produced in the TPD following C_2D_4 adsorption on silica supported Pd and Au-Pd clusters are shown after subtracting the background signals for C_2D_4/SiO_2. In Figure 16a for C_2D_4 dehydrogenation on 1.0 ML $Pd/SiO_2/Mo(112)$, two D_2 features appear with the desorption peak maxima at 310 and 470 K. These features are assigned to the β and γ states (the combination of γ_1 and γ_2 states), respectively. [119-121,123] With the addition of 0.1, 0.2, and 0.4 ML Au to 1.0 ML Pd/SiO_2 and a subsequent annealing at 800 K, the production of D_2 from C_2D_4 TPD gradually decreases from Figure 16b to Figure 16d. Upon addition of 0.6 ML Au in Figure 16e, the D_2 production yield is negligible. As demonstrated by the CO-IRAS/TPD and C_2D_4 TPD data, the loss of active sites, i.e., adjacent Pd atoms for di-σ bonded C_2D_4, is clearly responsible for attenuation of the C_2D_4 dehydrogenation reaction

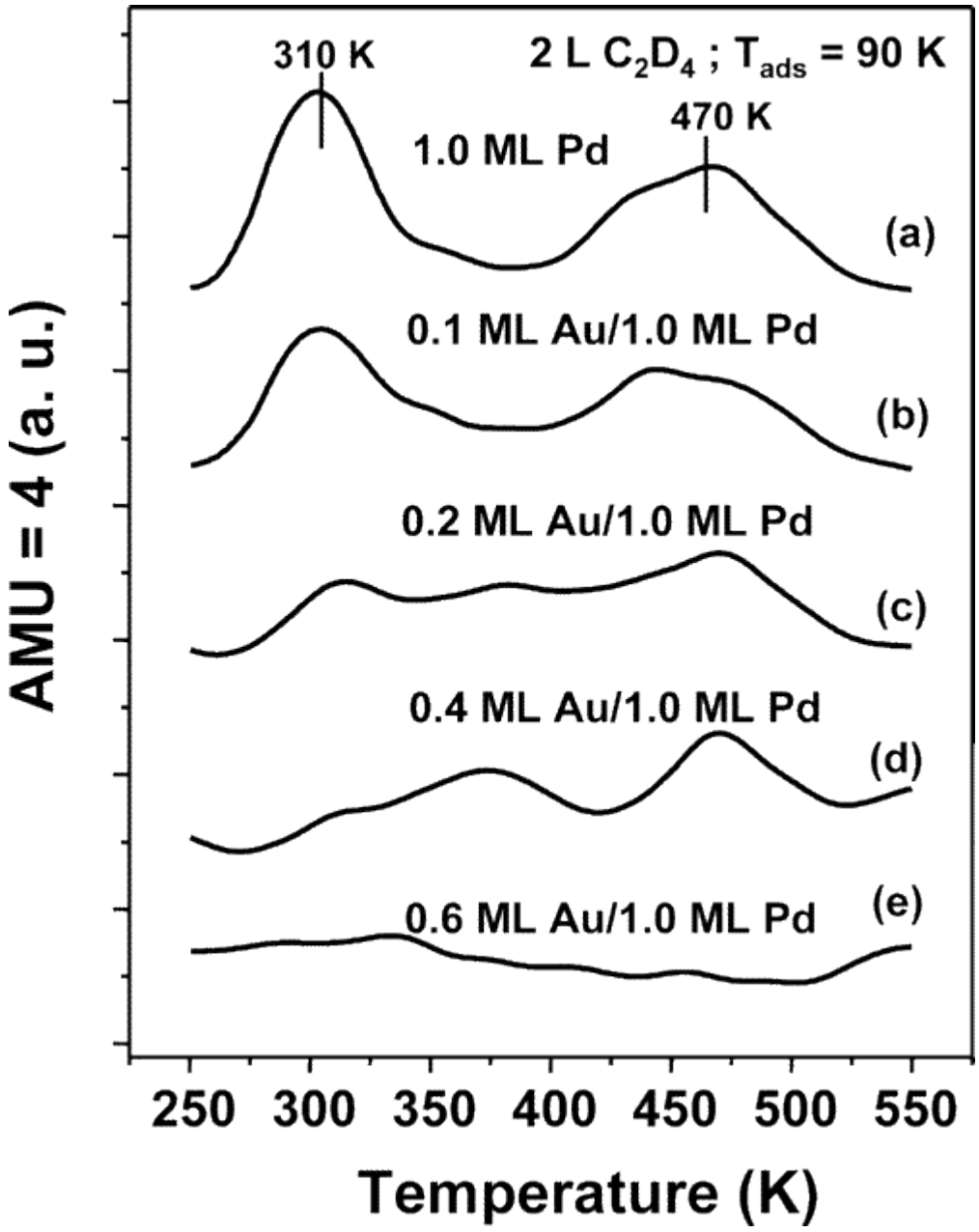

Figure 16. D_2 signals collected from C_2D_4 TPD with 2.0 L C_2D_4 exposure at 90 K on: (a) 1.0 ML Pd/SiO_2; (b) 0.1 ML; (c) 0.2 ML; (d) 0.4 ML; and (e) 0.6 ML Au/1.0 ML Pd/SiO_2 surfaces.

on the Au-Pd alloy cluster surface. The lack of suitable surface adsorption sites, i.e., three-fold hollow/bridging sites for the reaction intermediates, i.e., ethylidyne (≡C−CD_3) or vinylidene (=CD-CD_2), could also account for the loss of D_2 production. In Figure 17, the D_2 production yield, normalized to that obtained for 1.0 ML Pd/SiO_2, is plotted as a function of the density of the multiple Pd adsorption sites, i.e., bridging and three-fold hollow sites, after deposition of Au from 0 to 0.6 ML. The density of Pd multiple adsorption sites is obtained by subtracting the CO adsorption signals of atop Pd and Au sites in Figure 12e from Figure 12a−d, normalizing to that observed for 1.0 ML Pd/SiO_2. The plot in Figure 17 exhibits an excellent linear relationship for the D_2 formation as a function of the density of multiple Pd adsorption sites.

Conclusions

The growth of Au-Pd alloy clusters via a sequential deposition and annealing on amorphous ultrathin SiO_2 films has been characterized using LEIS and CO TPD. The surface composition of the Au-Pd clusters is shown to be Au-rich compared to the bulk of the cluster as observed previously for extended Au-Pd surfaces. However, the extent of Au enrichment is less for the Au-Pd clusters compared to the extended surfaces. CO adsorption on the Au-Pd alloy cluster surfaces was studied by TPD and IRAS and isolated Pd sites identified as a unique surface ensemble. TPD of ethylene adsorption and dehydrogenation show a clear surface structure-reactivity correlation with the population of isolated Pd sites.

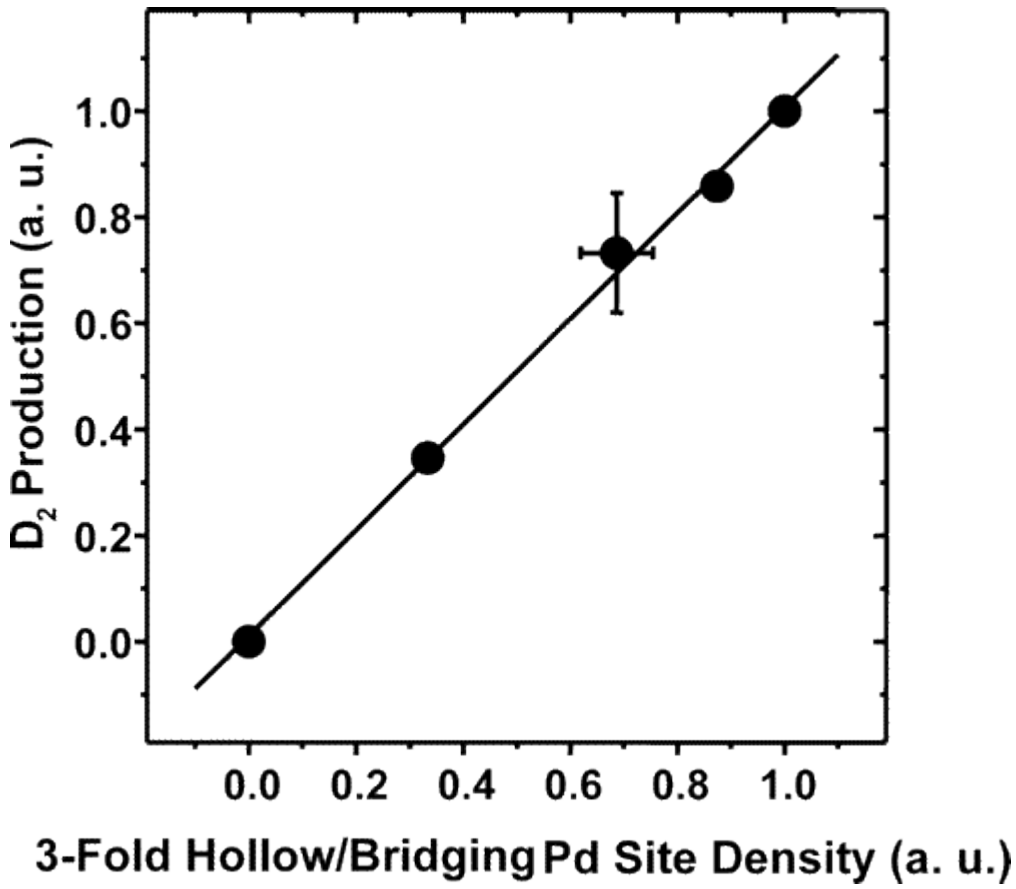

Figure 17. D_2 production yield as a function of 3-hollow/bridging Pd site density for C_2D_4 dehydrogenation of Au−Pd/SiO_2 alloy cluster surfaces.

4. BIMETALLIC PLANAR MODEL CATALYST CHARACTERIZATION*

Vinyl Acetate Synthesis over Model Pd-Sn Bimetallic Catalysts

Fundamental surface science studies of bimetallic alloy systems are important to many industrial applications some of which include metallurgy, catalysis, electrochemistry, magnetic materials, and microelectronics fabrication.[23] Particularly in heterogeneous catalysis, the addition of a second metal often greatly enhances the reaction activity, selectivity, and stability.[24-26] Further optimization of the catalytic performance requires a thorough understanding of the reaction mechanism at the atomic level, for which model surface science studies on well-defined surfaces can provide critical information. The preparation of ordered Pt-Sn surface alloys was first demonstrated by depositing Sn on Pt(111) or Pt(100) followed by annealing to elevated temperatures.[27-30] These well-characterized surface templates were used for extensive catalytic reaction studies.[25,31-35] These model studies have provided a more in depth understanding of the chemistry observed on ordered alloy surfaces including the relative importance of ensemble and ligand effects.

Only a limited number of model studies on Pd-Sn bimetallic systems have been performed despite the importance of Pd-based industrial catalysts.[36-39] Hamm et al.[36] and Lee et al.[37] studied the formation of two ordered Pd-Sn surface alloys by thermal

---

*Reprinted with permission from "Vinyl Acetate Synthesis over Model Pd-Sn Bimetallic Catalysts" by T. Wei, D. Kumar, M. S. Chen, K. Luo, S. Axnanda, M. Lundwall, and D. W. Goodman, *Journal of Physical Chemistry C* **2008,** *112*, 8332-8337, Copyright [2008] by American Chemical Society

treatment of vapor deposited Sn films on a Pd(111) single crystal. Depending on the preparation conditions, two surface periodicities, p(2 × 2) and (√3 × √3)R30°, were observed with surface stoichiometries of Pd_3Sn and Pd_2Sn, respectively. [36,37] On the Pd(110) single crystal, two ordered structures, c(2 × 2) and (3 × 1), were also reported corresponding to 0.5 monolayer (ML) and 0.67 ML of Sn in the surface layer.[39] In both cases, a strong chemical interaction between Sn and Pd was deduced based on core level binding energy shifts (CLS) and attenuation of the CO adsorption energy in TPD data.[37,39] However, no detailed investigations concerning Pd-Sn alloy formation on <100> oriented substrates have been reported. Previously, we had studied disordered Pd−Au model alloy surfaces[24,40-44] where Pd atoms were found to be isolated by Au atoms at low surface Pd coverage. [24,40-45] A pair of these Pd monomers has been proposed to serve as the active site for vinyl acetate synthesis.[24,40]

In the present work, Pd-Sn alloy films on a Rh(100) were used as model surfaces. Compared with Sn/Pd(100) model systems, bimetallic films provide more flexibility in controlling desired surface metal concentrations.[44] The surface composition, the extent of alloying, and the electronic properties in this system were studied, as well as their catalytic activities for vinyl acetate synthesis. In contrast to Pd-Au, Pd-Sn form ordered surface alloys where the surface Pd atoms are isolated by Sn atoms, maximizing the fraction of surface isolated Pd monomer pairs.

LEIS, LEED, and XPS

The experiments were carried out in several ultrahigh vacuum (UHV) chambers equipped with XPS, LEIS, IRAS, XPS, and a cell for reaction kinetic studies. Each

chamber was also equipped with LEED, AES, and TPD. The base operating pressure for each system was ~2×10^{-10} Torr. XPS and LEIS spectra were collected using a concentric hemispherical analyzer (PHI, SCA 10-360) and Ne^+ ions (0.75 keV) with an ion beam scattering angle of ~45° with respect to the surface normal. A Mattson Cygnus 100 FTIR spectrometer was used for the IRAS measurements. The IR spectra were acquired using 4 cm^{-1} resolution and 512 scans in the single reflection mode at an incident angle of 84° with respect to the surface normal. The Rh(100) single crystal was mounted on a transferable probe capable of liquid nitrogen cooling to 80 K and resistive heating to 1500 K. The sample temperature was monitored with a W-5% Re/W-26% Re (type C) thermocouple spot-welded to the back of the Rh(100) single crystal. A heating ramp of 5K/s was used for the TPD measurements. These experimental systems have been described in detail elsewhere.[124,125]

The VA synthesis experiments were carried out in a combined elevated-pressure reactor-UHV XPS chamber. [24,40] After preparation and characterization in the UHV chamber, the Pd-Sn/Rh(100) sample was transferred in situ into the reaction chamber through a double-stage, differentially pumped Teflon sliding seal. Glacial acetic acid (CH_3COOH) was further purified by triple distillation; research-grade ethylene (C_2H_4) and ultrahigh purity O_2 were used as received. A CH_3COOH:C_2H_4:O_2 (2:4:1) mixture with a total pressure of 14 Torr was used for the kinetic studies. The vinyl acetate product was analyzed by gas chromatography using a flame ionization detector (FID).

LEIS and LEED were used to investigate the surface composition and surface structure of Pd-Sn alloy films on Rh(100). A 1 ML Sn/4 ML Pd/Rh(100) alloy system

was arbitrarily chosen first to investigate the effects of different annealing temperatures. Figure 18a shows a series of LEIS spectra for a 4 ML Pd/Rh(100) surface and a 1 ML Sn/4 ML Pd/Rh(100) alloy surface as a function of various annealing temperatures. The alloy films were annealed at each indicated temperature for 1 min, and all spectra were collected at 300 K. A single scattering feature corresponding to Pd with a kinetic energy (KE) of ca. 0.47 keV was observed from the 4 ML Pd/Rh(100) surface. After depositing 1 ML Sn, the Pd scattering peak was attenuated and a new scattering feature, assigned to Sn, emerged at 0.49 keV. The Pd scattering intensity did not drop to zero at 1 ML Sn coverage, although the Pd peak becomes much less intense. That the Pd feature does not disappear may be due to Sn-Pd interdiffusion at 300 K or to contribution of the Pd LEIS signal from Pd in the second layer of the open fcc (100) surface.[126] As the annealing temperature was increased, the intensity of the Pd feature increased concomitantly with a decrease in the Sn feature. These changes in the Pd and Sn intensities are consistent with the interdiffusion of Sn and Pd. To analyze the surface composition, the surface concentrations of Sn and Pd were calculated using the following equation in combination with the LEIS data in Figure 18a.[42,43]

$$c_{Sn} = \frac{I_{Sn}}{I_{Sn} + f_{Sn/Pd} I_{Pd}} \tag{4.1}$$

The influence of annealing temperature on surface concentration is plotted in Figure 18b. A decrease in Sn surface concentration (C_{Sn}) and an increase of Pd surface concentration (C_{Pd}) was apparent with an increase in the annealing temperature to 700 K. At 700 K, the surface concentrations of Sn and Pd were ca. 47% and 53%, respectively.

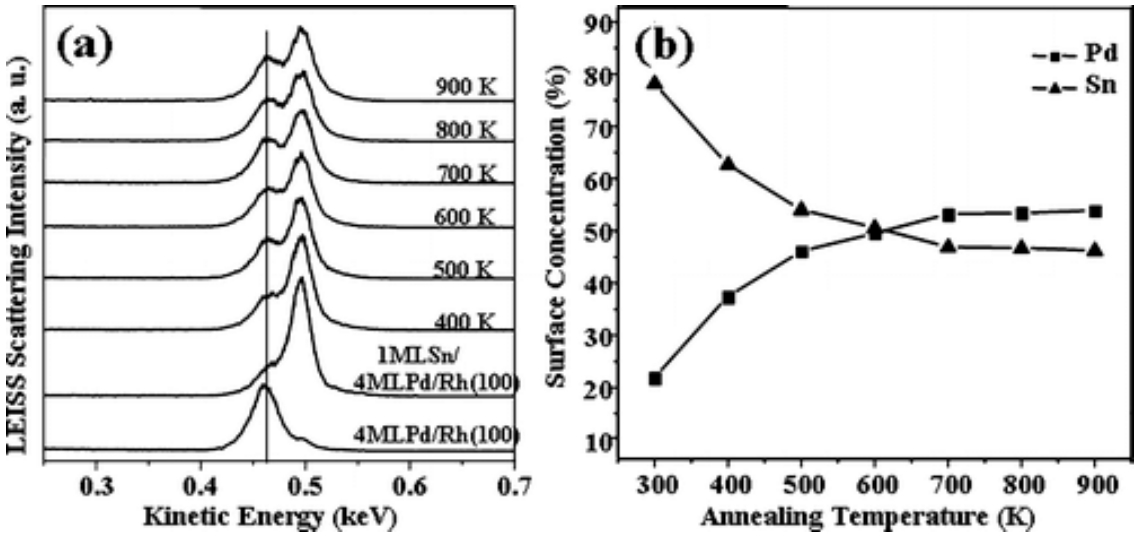

Figure 18. (a) Ne^+ scattering LEIS spectra for 4 ML Pd/Rh(100) surface and 1 ML Sn/4 ML Pd/Rh(100) surfaces with different annealing temperatures. The Pd-Sn alloy surfaces were annealed at each indicated temperature for 1 min before taking LEIS spectrum at room temperature. (b) The corresponding surface concentrations of Sn and Pd for 1 ML Sn/4 ML Pd/Rh(100) system as a function of annealing temperature.

At a temperature above 700 K, the surface composition of Pd and Sn is constant and consistent with a stable Pd/Sn surface alloy with a ratio of ~1:1.

LEED was used to further characterize the Pd - Sn alloy surface structure. Figure 19 displays the LEED pictures from (a) the clean Rh(100) substrate, (b) the 4 ML Pd/Rh(100) surface, and (c) the 1 ML Sn/4 ML Pd/Rh(100) surface. Both of the Pd and Pd−Sn alloy films were annealed at 700 K for 1 min before photographing. The 4 ML Pd film exhibited a clear (1 × 1) LEED pattern (Figure 18b), even though the spots were more diffused and the background was brighter compared with the clean Rh surface. This indicates that the Pd film grows pseudomorphic overlayers on Rh(100), adopting a substrate-like <100> orientation. Because of the small lattice difference between Pd and Rh, it is not surprising that the 4 ML Pd film surface is not as ordered as the substrate Rh(100) surface. After deposition of 1 ML Sn onto this Pd film and annealing the sample surface to 700 K, a new LEED pattern of c(2 × 2) was clearly observed (Figure 19c). A checkerboard-like, ordered c(2 × 2) Sn-Pd alloy surface structure has been proposed by Logan et al. for the Sn/Pd(100) system.[38] For the Sn/Pt(100) system, [27-35] a series of studies have concluded that a similar, planar c(2 × 2) Pt-Sn alloy structure is formed after annealing the alloy surface to 700-750 K. From the above LEIS results, the surface concentrations of Pd and Sn in the 1 ML Sn/4 ML Pd/Rh(100) surface are close to 50% after annealing to 700 K. Based on these LEIS and LEED results and the similar previous studies on the Sn/Pt(100) system, an ordered Pd-Sn alloy structure as depicted in the bottom of Figure 19 is presumed.

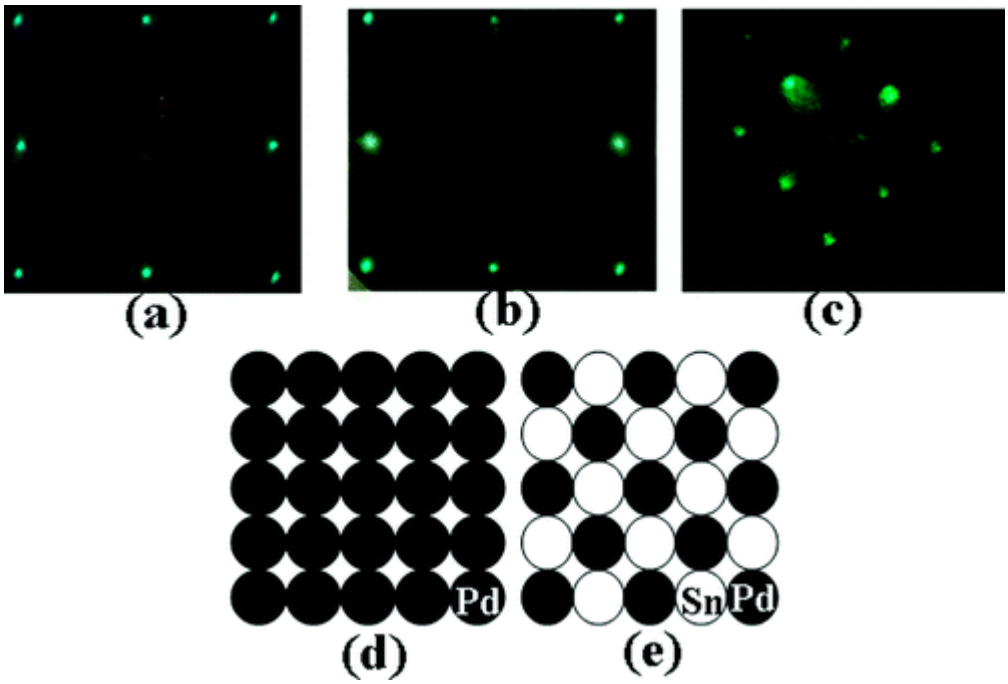

Figure 19. LEED pictures for (a) clean Rh(100) substrate, (1 × 1) ; (b) the 4 ML Pd/Rh(100) surface, (1 × 1); and (c) the 1 ML Sn/4 ML Pd/Rh(100) surface, c(2 × 2). Both the Pd film and the Pd - Sn alloy film were annealed at 700 K for 1 min before acquisition of LEED. The photos were taken at 300 K, and the incident electron beam energies are indicated with the pictures. (d and e) Schematic surface structures of Pd/Rh(100) and c(2 × 2) Pd-Sn/Rh(100).

In order to probe the proper preparation conditions for ordered Pd-Sn alloy surfaces, LEIS experiments with depositions of different initial Sn coverages on a 4 ML Pd film were carried out. The changes in the surface concentrations of Pd and Sn as a function of dosed Sn based on the LEIS data are shown in Figure 20. It should be noted that each of these alloy surfaces was annealed at 700 K for 1 min prior to acquisition of the LEIS data. Ideally, 0.5 ML Sn is needed to form a c(2 × 2) ordered Pd-Sn alloy surface assuming limited diffusion of the Sn into the bulk Pd film. Our results indeed show the surface concentrations of the 0.5 ML Sn/4 ML Pd/Rh(100) alloy surface after annealing to 700 K is approximately 1:1 Pd to Sn, specifically 40% Sn and 60% Pd. This is actually expected because the surface free energy of Sn is much smaller than that of Pd, i.e., diffusion of Sn into the bulk Pd film is thermodynamically unfavorable. With the addition of >0.5 ML Sn, the surface concentrations of Pd and Sn remained constant. It is likely that Sn in excess of 0.5 ML diffuses into the bulk leaving the c(2 × 2) ordered structure at the outmost surface layer.

XPS experiments were also carried out to study the electronic structural changes in the process of forming an ordered Pd-Sn alloy surface. In Figure 21a, Sn 3d core level spectra are displayed as a function of the annealing temperature for the 1 ML Sn/4 ML Pd/Rh(100) surface. No obvious peak intensity variations or core level binding energy (CLE) shifts are apparent as the annealing temperature is increased to 700 K. A decrease in the intensity and a slight reduction of the CLE is evident after annealing to 800 K. The Pd 3d core level features measured concomitantly are shown in Figure 21b. The CLE values for the Pd 3d features did not change significantly following the Sn

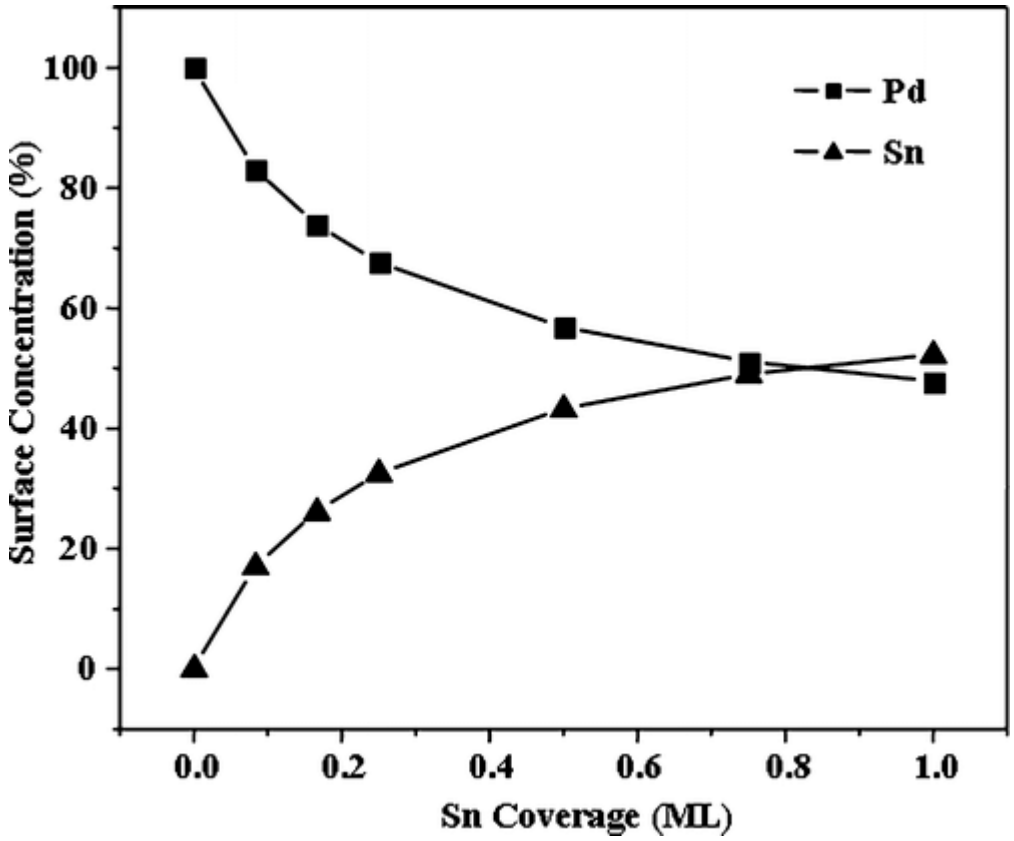

Figure 20. Surface concentrations of Sn and Pd for Pd-Sn alloy films with different initial Sn coverages on 4 ML Pd/Rh(100) surface. Each alloy surface was annealed at 700 K for 1 min before the LEIS measurement.

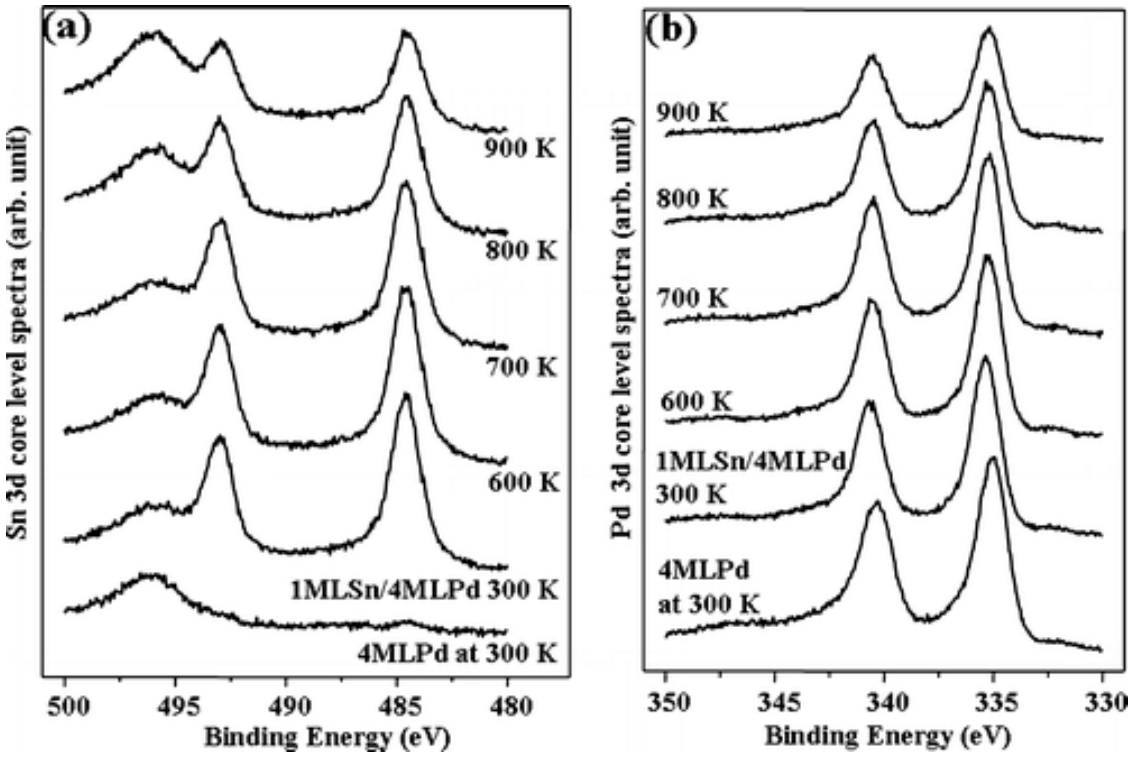

Figure 21. The XPS Sn 3d (a) and Pd 3d (b) core level spectra for the 1 ML Sn/4 ML Pd/Rh(100) surface as a function of annealing temperature.

deposition and annealing at different temperatures. The intensities, however, of these peaks are attenuated after annealing the alloy film to temperatures higher than 800 K. The observed small CLBE changes of the Pd and Sn 3d features observed after annealing correlate very well with results found previously for Sn/Pd(111).[37]

IRAS and TPD

The chemisorptive properties of Pd-Sn alloy surfaces were studied by IRAS and TPD using CO as a probe. Control experiments of CO adsorbed on a 4 ML Pd film were first carried out. Figure 22a displays a series of IRAS spectra acquired in 1×10^{-7} Torr CO background as a function of sample temperature. Only one feature was observed in this series of spectra. This feature appears as a broad peak at 1908 cm^{-1} at 500 K, then gradually blue shifts to 1985 cm^{-1} upon cooling the sample to 250 K. At CO saturation coverage, this feature reaches 2001 cm^{-1} and becomes much sharper. The spectral features and the temperature dependent frequency shift are essentially identical in the corresponding data found in CO-IRAS spectra acquired for Pd(100) under similar conditions.[115,127,128] These data are entirely consistent with the above LEED results and support the conclusion that the 4 ML Pd film on Rh(100) adopts a <100>-like orientation. Based on the TPD and LEED studies carried out for CO on Pd(100), [115,127,128] this CO-IR feature is assigned to CO adsorption on 2-fold bridging Pd sites. IRAS spectra for CO adsorption on 1 ML Sn/4 ML Pd/Rh(100) surface as a function of sample temperature are shown in Figure 22b; the alloy surface was annealed at 700 K for 1 min, and all of the spectra were collected in 1×10^{-7} Torr CO background. Only a single IR feature around 2094 cm^{-1} is apparent in this series of spectra. Comparing with

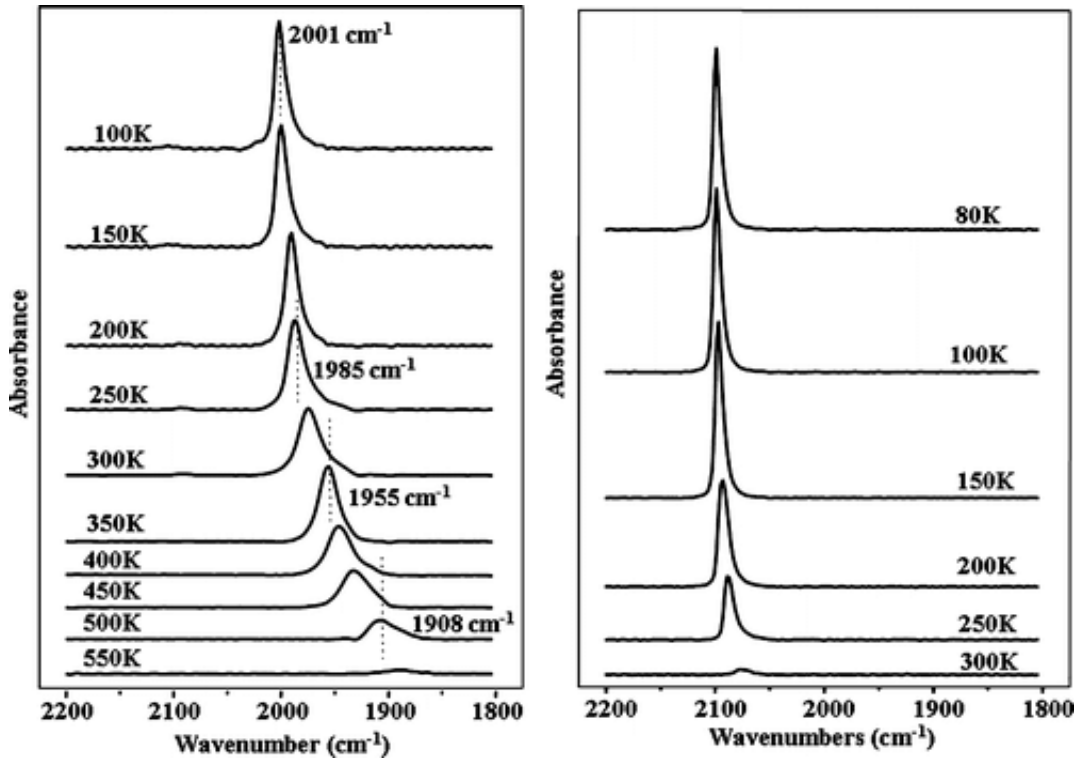

Figure 22. IR spectra for CO adsorption on (a) 4 ML Pd/Rh(100) and (b) 1 ML Sn/4 ML Pd/Rh(100) after an anneal at 700 K for 1 min, in a 1×10^{-7} Torr CO at various temperature as indicated in the figures.

the single feature observed on 4 ML Pd film surface at 2001 cm^{-1}, this IR result clearly shows that totally different adsorption sites are formed on the Pd-Sn alloy surfaces. The frequency of this feature corresponds to CO adsorption on atop Pd sites. Moreover, this IR feature attenuates between 150 and 200 K, and completely disappears below 300 K. On a 4 ML Pd film surface, a CO-IRAS feature can be seen up to 500 K. The contrast in these spectra shows that CO adsorbs differently on the Pd-Sn alloy surface. The lower desorption temperature indicates weaker CO-substrate bonding, paralleling the conclusion that CO adsorbs on atop Pd sites. It is also noteworthy that the IR frequency for isolated Pd sites on Pd-Au alloy surface is 2088 cm^{-1}, and this isolated Pd IR feature for Pd-Au vanishes around 300 K. The similarities in both IR frequency and CO desorption temperature in these two systems suggest that CO occupies identical adsorption sites in both these systems, i.e. CO adsorbs on the isolated Pd sites on the Pd-Sn alloy surface.

A direct comparison of the saturation CO-IRAS spectra from 4 ML Pd film, 4 ML Sn film, and 1 ML Sn/4 ML Pd alloy film further supports the above conclusion. As seen in Figure 23a, no IR feature is observed on 4 ML Sn film surface at 80 K due to the weak interaction between Sn and CO. Based on the above LEIS and LEED results, the 1 ML Sn/4 ML Pd alloy film annealed at 700 K forms a well-ordered c(2 × 2) alloy structure, and that the IR feature observed on Pd-Sn alloy surface arises from CO adsorption on the isolated Pd sites. Furthermore these data show that most of the surface Pd atoms on Pd-Sn alloy surfaces are isolated, consistent with an ordered c(2 × 2) arrangement.

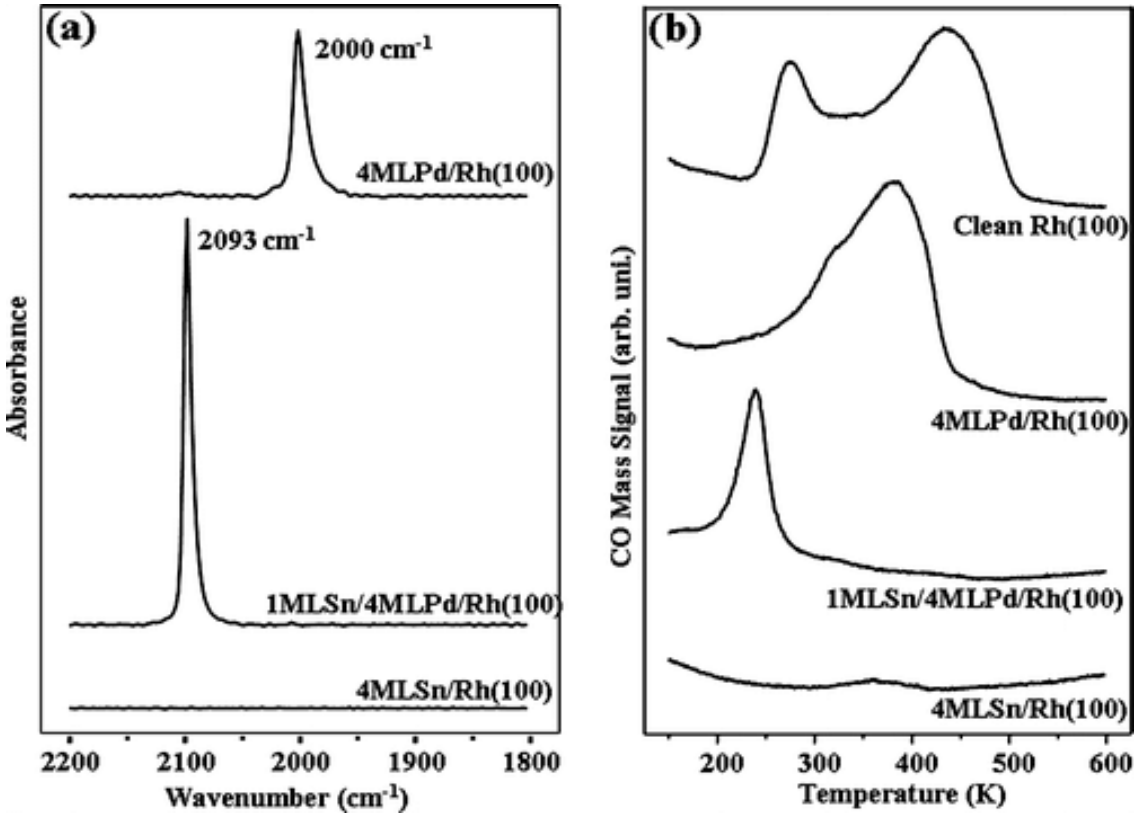

Figure 23. (a) A comparison of CO adsorption on 4 ML Sn/Rh(100), 4 ML Pd/Rh(100) and 1 ML Sn/4 ML Pd/Rh(100). Each surface was annealed at 700 K for 1 min before CO adsorption at 80 K in 1×10^{-7} Torr. (b) CO TPD on Rh(100), 4 ML Pd/Rh(100), 1 ML Sn/4 ML Pd/Rh(100), and 4 ML Sn/Rh(100). CO was adsorbed at 80 K at a saturation coverage.

It should be also noted that the IR frequency for the isolated Pd sites in Pd-Sn alloy systems is slightly higher than that in Pd-Au systems (2094 cm^{-1} vs 2088 cm^{-1}). This may be due to the difference in the surface orientation (Pd-Sn(100) vs Pd-Au(111)). Also an electronic effect, e.g., charge transfer between Pd and Sn or Au, may contribute to this difference. Further investigations regarding this issue are warranted. Moreover, a blue shift is observed in Figure 22 when the surface CO coverage is increased on the Pd-Sn alloy surface. In the Pd-Au alloy system, the IR frequency for the isolated Pd sites is not shifted with a change in the surface CO coverage. This may be caused by the fact that the saturation CO coverage on the Pd-Sn alloy surface is higher than that of the Pd-Au surface. Dipole-dipole interactions from neighboring CO molecules may induce this shift to higher frequencies, however further experiments are also required to confirm this conclusion.

CO TPD was also used to further study the CO adsorption behavior on Pd-Sn alloy surfaces. In particular, the CO adsorption/desorption properties of the c(2 × 2) ordered Pd-Sn alloy surface were examined and compared with that of clean Rh(100) substrate, 4 ML Pd, and 4 ML Sn films. In Figure 23b, saturation CO TPD spectra for all these surfaces are presented. The clean Rh(100) substrate gives a broad desorption feature ranging from 250 to 500 K. Upon deposition of 4 ML Pd on Rh(100), this broad peak is completely quenched and replaced by a feature in the range 300 to 450 K, indicating the 4 ML Pd film wets the surface effectively. With respect to the desorption temperature and spectral shape, the CO TPD spectrum from the 4 ML Pd film is almost identical with that from a Pd(100) single crystal. [115,127,128] This confirms the above

LEED and CO-IRAS results showing that the 4 ML Pd film has a <100>-like surface orientation. As was pointed out in earlier discussions of CO-IRAS and TPD studies on different facets of Pd single crystal surfaces, [115,127,128] this feature can be assigned to the CO adsorption on Pd bridging sites. For the 1 ML Sn/4 ML Pd/Rh(100) alloy film annealed at 700 K, a sharp and symmetrical CO desorption feature at 250 K is observed. This desorption temperature agrees very well with the above temperature dependent IRAS spectra (Figure 22), indicating a much weaker CO adsorption site is formed on Pd−Sn alloy surfaces, i.e., isolated Pd sites. The fact that this feature is sharp and symmetrical is also consistent with the formation of an ordered Pd-Sn alloy surface structure. In addition, no significant CO desorption features are observed for a 4 ML Sn surface. The small feature at 350 K on this surface may arise from diffused surface Rh atoms, since it is well-known that Sn can easily form alloys with Rh.

Activity for Vinyl Acetate Synthesis

VA syntheses have been carried out on both model and oxide supported Pd-Au catalysts.[24,40,81,129-134] It was demonstrated that a pair of noncontiguous, suitably spaced, Pd monomers serve as the critical reaction sites.[24] For a clean Rh(100) or Sn/Rh(100) surface, no VA formation was observed. On a Pd(4 ML)/Rh(100), a turnover frequency (TOF) of 1×10^{-5} s^{-1} was observed for a 3 h reaction, consistent with Pd being an active catalyst for VA synthesis.[24,40] Subsequently various amounts of Sn were deposited on a Pd(4 ML)/Rh(100) film followed by an anneal at 600 K for 1 min. Each surface was then in situ transferred into the reaction cell for VA reaction for 3 h. The results are shown in Figure 24. The reaction rates were computed based on the concentration of surface Pd

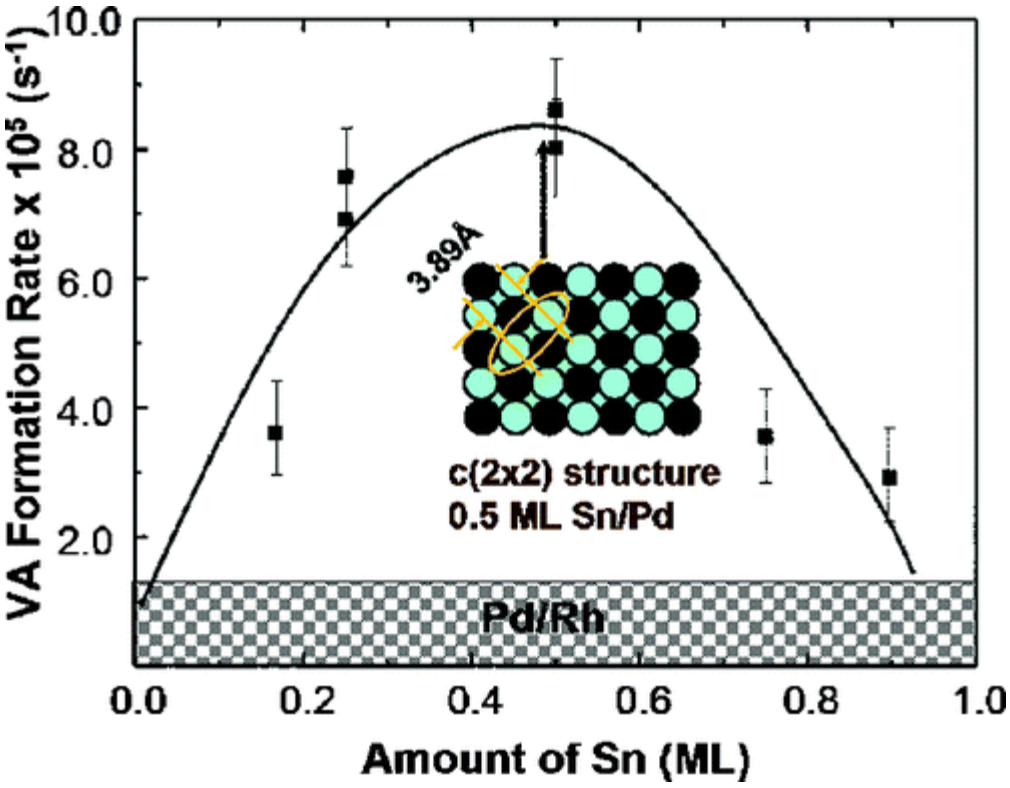

Figure 24. VA formation rate normalized to per Pd site basis on Sn/ 4.0 ML Pd/Rh(100) annealed to 600 K for 60 s. Reaction at 450 K; p_{O2} = 2.0 Torr; p_{C2H4} = 9.0 Torr; p_{AcOH} = 4.0 Torr; time = 3 h.

assuming that only Pd is active for VA synthesis. The VA formation rate increases with increasing Sn coverage, maximizing at a Sn coverage of 0.5 ML. The VA rate decreases with a further increase in Sn coverage up to 1 ML. The rate at 0.5 ML Sn coverage is significantly higher compared to Pd-alone on Rh(100). As discussed in the previous section, a c(2 × 2) ordered surface arrangement was formed at a Sn coverage of 0.5 ML. For this c(2 × 2) structure, all surface Pd atoms are isolated by Sn with a maximum number of isolated Pd pairs. Such isolated pairs have been demonstrated previously to be a more efficient active sites for VA synthesis than for contiguous Pd sites. [24,40] These data then are consistent with isolated Pd pairs serving as the catalytic active site for VA synthesis. In the Pd-Au alloy system, an ensemble effect was assumed to be the dominant factor for the enhanced VA reactivity, whereas a ligand (or electronic) effect was considered to be insignificant due to the limited chemical interaction between Pd and Au.[24] In the Pd-Sn system, the chemical interaction between Pd and Sn is much stronger. Therefore, it is difficult to assess the influence of a ligand (electronic) effect on the VA reactivity without further detailed investigations. The fact that the VA reactivity decreases as the Sn coverage is increased from 0.5 to 1 ML may indicate that a ligand effect plays a significant role. Even though the surface Pd concentration remains at 50% during the Sn coverage between 0.5 to 1 ML, the extra Sn that diffuses into the second or deeper layers may affect the chemisorptive behavior of the surface Pd atoms, which may result in a diminution of the VA rate within this Sn coverage range.

However, it is emphasized that the rate obtained for the Pd-Sn surface over a three-hour-average is much smaller than that for a Pd-Au surface. This lower rate may

be due to oxidation of Sn under VA synthesis reaction conditions as indicated by XPS after reaction. Such oxidation of Sn will result in dealloying of Sn-Pd and phase separation of Pd and SnO_x. Furthermore, the SnO_x residue on the surface serves to block the Pd active sites. Noting the time dependent rate, of greater significance is the initial reaction rate of the Pd-Sn catalyst as shown in Figure 25 for a 0.5 ML Sn/Pd(4 ML)/Rh(100) surface. The VA formation rate indeed decreases very rapidly as the reaction proceeds. After 10 h of reaction, the activity is in fact much less than for Pd alone. An initial rate of 5 x 10^{-4} molecules/(per site per second) was obtained by extrapolating the rate data to zero time, a rate some fifty times higher than that found for Pd alone.

Conclusions

Pd-Sn bimetal thin films were synthesized on Rh(001). A 4 ML Pd on Rh(100) exhibits similar properties as Pd(100). Upon deposition of Sn onto Pd/Rh(100) and following an annealing at 600 K, an ordered surface arrangement of c(2 × 2) was formed at a Sn coverages greater than 0.5 ML. LEIS and IRAS using CO as a probe confirmed a surface structure containing equal amounts of Sn and Pd with isolated Pd and Sn atoms. This checkerboard arrangement showed a maximum catalytic performance for VA synthesis. This alloy system demonstrates that a pair of isolated Pd monomers serves as an active site for VA synthesis as previously proposed. [24,40]

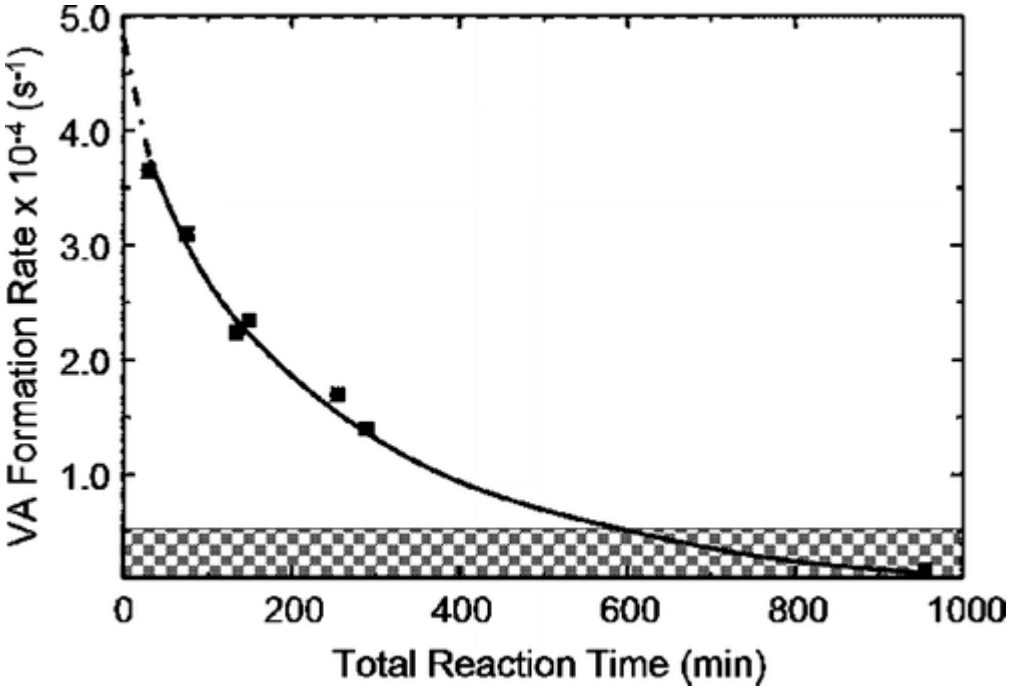

Figure 25. VA formation rate as a function of time on 0.5 ML Sn/4.0 ML Pd/Rh(100) annealed to 600 K for 60 s. Reaction at 450 K; p_{O2} = 2.0 Torr; p_{C2H4} = 9.0 Torr; p_{AcOH} = 4.0 Torr.

5. BIMETALLIC BULK ALLOY CATALYST CHARACTERIZATION*

Atomic Scale Assembly of a Heterogeneous Catalytic Site

Since one of the ultimate goals in heterogeneous catalysis is the design of novel catalysts from the nanoscale up, a fundamental understanding of the catalytic chemistry at the molecular- and atomic-scale is critical.[135] Recent advances in nanoscience have greatly contributed to this effect. Current tools useful to bottom-up catalyst design already include the control of the quantum-size effect by the dimensionality of the active nanoparticles.[136] In bimetallic catalysis, examples of these tools include the use of ligand effects to inhibit active-site poisoning[26] or the use of ensemble effects to facilitate the adsorption of specific reactant molecules.[45]

Recently, our group demonstrated that the active catalytic site for vinyl acetate (VA) formation

$$\underset{\text{Acetic acid}}{1/2\ O_2 + CH_3COOH} + \underset{\text{Ethylene}}{CH_2{=}CH_2} \xrightarrow{Pd} \underset{\text{Vinyl Acetate}}{CH_3COOCH{=}CH_2} + H_2O$$

on a Pd/Au(100) surface alloy is a Pd "monomer pair" with Au nearest-neighbors (Figure 26A). For this process, while a Au-isolated surface Pd atom is active for VA formation, the presence of a second Pd atom lowers the barrier for the step juxtaposing

*Reprinted with permission from "Atomic-Scale Assembly of a Heterogeneous Catalytic Site" by Patrick Han, Stephanus Axnanda, Igor Lyubinetsky, and D. Wayne Goodman, *Journal of American Chemical Society* **2007,** *129,* 14355-14361, Copyright [2007] by American Chemical Society

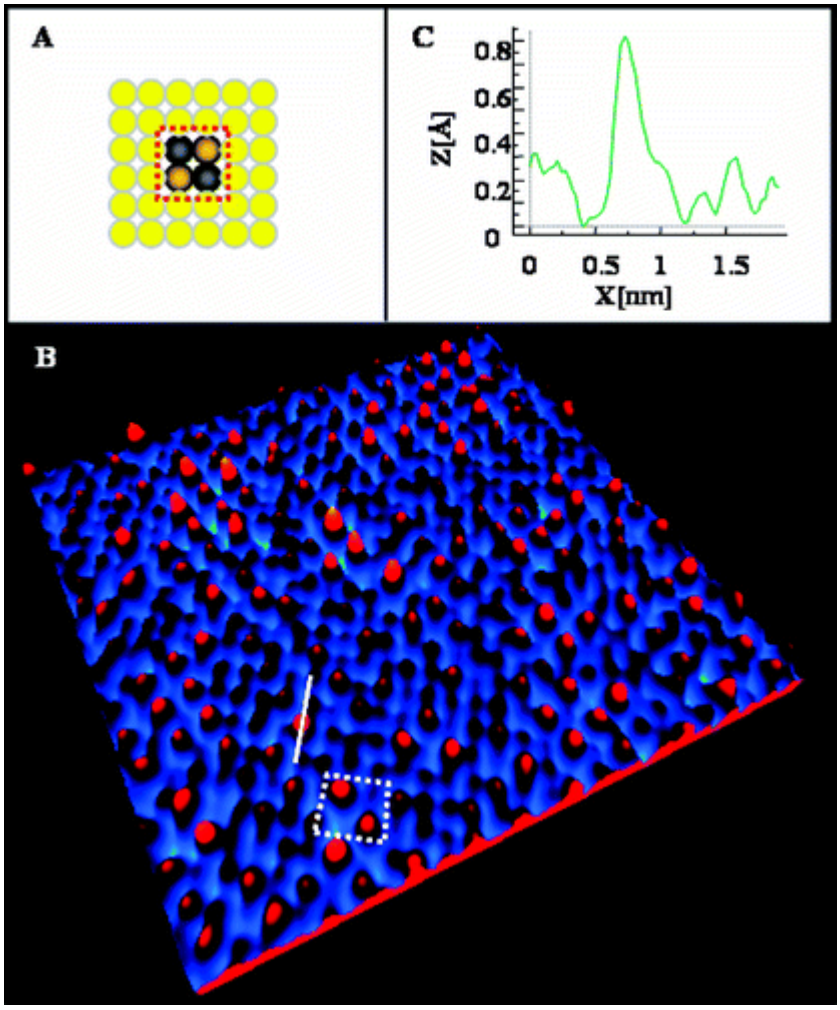

Figure 26. (A) Schematic representation of the catalytic site active to vinyl acetate formation referred to as "monomer pair" from ref [24] (red dotted square). This configuration is closely related to the c(2 × 2) structure on a metal fcc(100) surface. (B) 3D-view of an STM image (7.7 nm × 7.7 nm, $V_s = -10$ mV, $I_t = 5.0$ nA) of the AuPd(100) bulk alloy. The white dotted square highlights an example of the targeted Pd monomer pair. (C) Height trace of a Pd atom surrounded by Au atoms. The location of (C) is shown as a white line in (B).

acetic acid and ethylene,[24] believed to be rate-limiting.[137,138] Therefore, the key aspect of ref 24 lies in the precise locations of the surface atomic species. To maximize the activity enhancement for VA formation, the optimum distance between Pd atoms within a single catalytic site is predicted to be 0.33 nm, while the two atoms shared as nearest-neighbors by the Pd atoms must be Au atoms. This catalytic site structure is best modeled by the c(2 × 2)-like configuration on a (100)surface shown in Figure 26A, which has a Pd−Pd distance of 0.41 nm.

Here, we use ultrahigh vacuum (UHV) scanning tunneling microscopy (STM) to image the Pd monomer pair on a AuPd(100) bulk alloy surface, to target the Pd monomer-pair active site. Moreover, we present a method for increasing the concentration of active sites that relies on the thermodynamic properties of binary solid mixtures.[139] We demonstrate that, by choosing a bulk alloy of specific composition, and by using a specific crystal preparation method, it is possible to influence the atomic arrangement within the AuPd(100) surface lattice, maximizing the concentration of this desired active site. The validity of this concept is tested by comparing the Pd distribution on our surface with that of a previously imaged $Au_3Pd(100)$ surface prepared differently by Achoff et al.[140] This method of globally controlling the lateral distribution of metal atoms at the atomic scale has important implications in bimetallic catalysis and other alloy technologies. Its usefulness extends to any field that requires a bottom-up approach to nanoscale surface structures.[141-143]

Experimental Section

The experiments were performed in two UHV chambers. The first chamber is equipped with an STM (Omicron VT-STM), a semispherical electron energy analyzer (VG), a mass spectrometer (Ametek), and electron and ion guns (VG and SPECS, respectively). A base pressure of 5×10^{-11} Torr was maintained. All STM images were acquired at room temperature, in constant current mode, using an electrochemically etched W tip. The AuPd(100) bulk alloy single crystal was purchased from Matek, and the ordered surface was obtained through repeated sputter and anneal cycles (E = 500 eV, I = 0.38 μA, Ar^+ sputtering at room temperature for 20 min, annealing at ~550 °C for 15 min). The sample was annealed without sputtering at 550 °C for 30 min before imaging and was allowed to cool to room temperature without deliberate temperature quenching. The surface temperature was measured optically by infrared pyrometry.

The second chamber is equipped with low-energy ion scattering spectroscopy (LEISS), X-ray photoelectron spectroscopy, temperature programmed desorption, and low-energy electron diffraction (LEED) with a base pressure of 5×10^{-10} Torr. For the LEISS experiments, the sample was heated resistively. The temperature was measured using a C-type thermocouple (W-5%Re/W-26%Re) spot welded to the backside of the sample. LEISS experiments were carried out using a He^+ beam with an energy of 1000 eV and an incident angle of ~45° from the surface normal. The LEISS spectra were collected using a concentric hemispherical analyzer and were acquired at room temperature. The sample was treated with the same cleaning procedure used in the first

chamber before LEISS experiments were done. The surface concentrations of Au (c_{Au}) from the AuPd alloy were calculated using the following equation:[74]

$$c_{Au} = I_{Au} / (I_{Au} + f_{Au/Pd}.I_{Pd}) \quad (5.1)$$

where $f_{Au/Pd}$ is the ratio of the scattering intensity for pure Au and Pd, and I_{Au} and I_{Pd} are the scattering intensity from Au and Pd from the alloy surface, respectively.

Results and Discussion

Imaging the AuPd(100) surface with atomic resolution reveals a chemical contrast between Pd and Au surface atoms.[144] Figure 26B shows a Fourier-filtered STM image of the surface. The white dotted square highlights a Pd monomer pair, the targeted active site (highlighted in Figure 26A by a red dotted square). The chemical contrast is explained by the difference in the local electronic density of states near the Fermi edge between Pd and Au atoms.[145] This effect is further enhanced by STM tips with a specific type of apex prone to an increased interaction with Pd, the more reactive surface species.[145] Based on this and previous STM work on a $Au_3Pd(100)$ bulk alloy,[140] we assign the higher protrusions in Figure 26B to Pd atoms. Typically, the apparent-height difference associated with the chemical contrast for alloy surfaces ranges from 10 to 60 pm,[145] with very narrow apparent-height distributions for each metallic species. Our observed height difference between Pd and Au surface atoms falls within this range (Figure 26C).

Aside from the contrast between Au and Pd, the entire surface is also modulated by the electronic contribution of subsurface atoms.[146] This is apparent in Figure 27A,

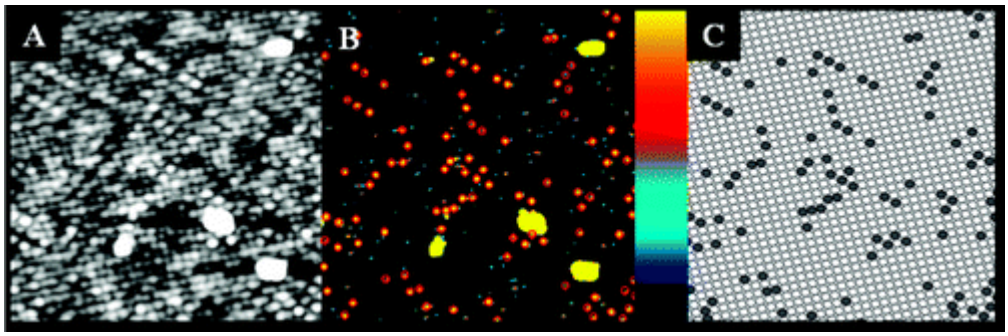

Figure 27. (A) STM image of a AuPd(100) bulk alloy (10 nm × 10 nm, V_s = −15 mV, I_t = 6.3 nA). The large white features are impurities thought to be carbon (Auger electron spectroscopic measurement of the surface showed no visible signal of C, S, O, K, or Ca). (B) The same STM image as that in (A) excluding all data points below the cutoff height, which is set to 5 pm below the highest point of the image. The color bar scale spans from 0 to 5 pm. The red circles denote the features designated to be Pd atoms. These red circles are set to have an area of ~0.15 nm^2. (C) Schematic representation of (A) for clarity.

which shows an unfiltered STM image of the AuPd(100) surface. Here, a disparity in apparent height is observable between atoms of the same species.

Since the exact location of each surface Pd atom is critical to surface Pd distribution measurement, we use unprocessed STM data for Pd assignment. Due to the convolution of both chemical contrast and the electronic contribution of the subsurface atoms, the following method was used to distinguish Pd from Au atoms. To designate the surface Pd atoms, all data points of the image in Figure 27A below a cutoff height are shown uniformly in black in Figure 27B. The cutoff height chosen is 5 pm below the highest surface atom (impurities are not included in the process). Any remaining bright spots in Figure 27B that have a surface area of ~0.15 nm^2 are designated as Pd atoms. Local profile measurements are performed to ensure correct assignments (Figure 26C). All surface atoms are then counted, giving 103 Pd atoms out of a total of 1287 surface atoms (8% Pd). This is in good agreement with our LEISS measurements (10% Pd at 550 °C annealing temperature, Figure 28). Figure 27C shows a schematic representation of the STM image shown in Figure 27A for clarity.[147] This analysis is performed for three STM images acquired over different regions of the surface.

To analyze the distribution of the surface Pd atoms, we compare the observed distribution with a calculated random distribution.[148] $P(C)$, the probability of a surface Pd atom having its eight nearest-neighbors arranged in a specific configuration C (shown on the abscissa of Figure 29), is calculated assuming a complete random distribution. The following equation is used

$$P(C) = m(\rho_{Pd}{}^{n} \times \rho_{Au}{}^{(8-n)}), \qquad 0 \le n \le 8 \tag{5.2}$$

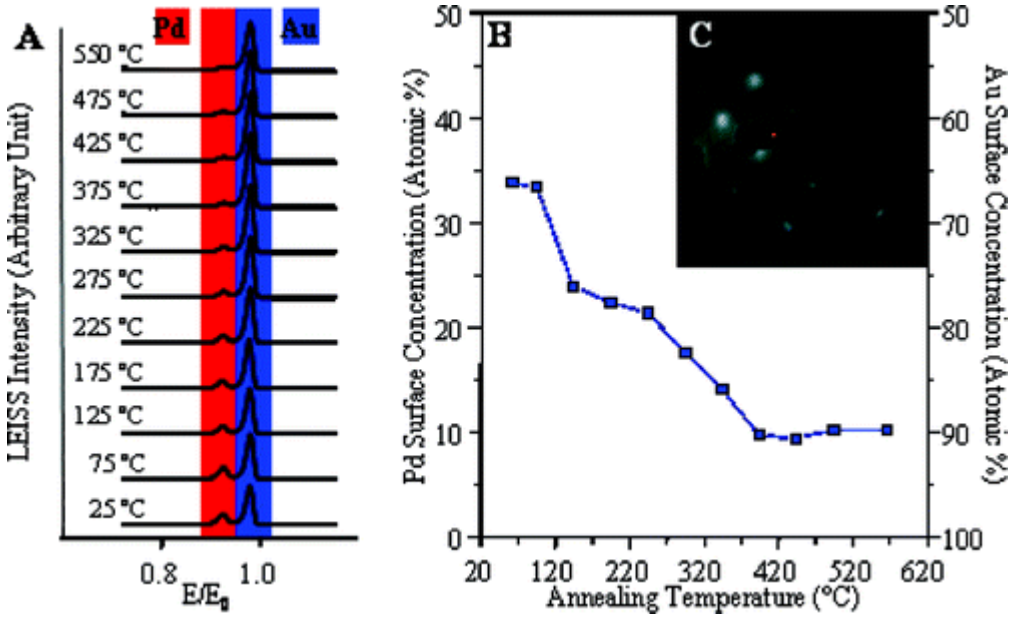

Figure 28. (A) Low-energy ion scattering spectra of AuPd(100) as a function of temperature. Each spectrum was collected at 25 °C after the sample was annealed to the indicated temperature. The spectrum at 25 °C was collected immediately after sputtering at 25 °C. (B) Surface concentration of Pd on AuPd(100) as a function of annealing temperature. Except at 25 °C, the sample was annealed at each temperature for 10 min. The low Pd surface composition at 25 °C may be a result of surface segregation at this temperature. It should be noted that, in a separate LEISS experiment, annealing the sample at 550 °C for 3 × 10 min showed no change in Pd surface concentration: we conclude that the Pd surface concentration reaches equilibrium after 10 min. (C) Low-energy electron diffraction of AuPd(100) after the last annealing of the sample at 550 °C, showing the fcc(100)-(1 × 1) square pattern.

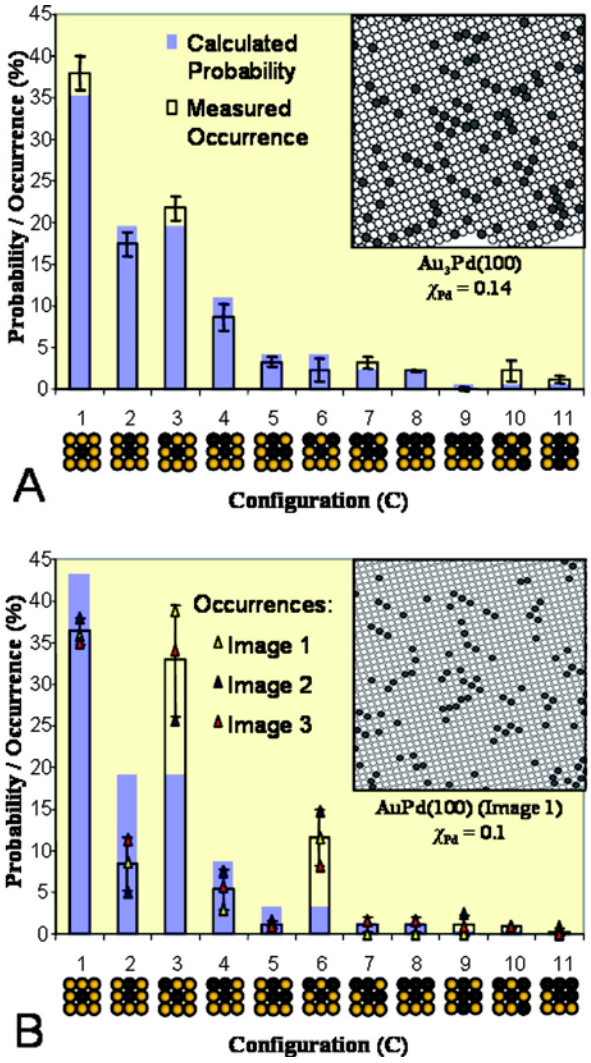

Figure 29. Comparison between calculated probability and observed occurrence of specific nearest-neighbor configurations around a Pd atom. The chart in (A) shows the Pd distribution from the STM image (7.9 nm × 7.9 nm) acquired previously by Achoff et al. over a $Au_3Pd(100)$ surface[140] (schematic representation in the inset). Error bars in (A) show the standard deviations between the calculated probabilities and measured occurrences. The chart in (B) shows the Pd distributions of the AuPd(100) surface. Each measured occurrence in (B) is the averaged value of respective measurements made on three STM images (10 nm × 10 nm) acquired over different surface regions. The occurrence measurement of each image is also shown as triangles. Error bars in (B) show the standard deviations of the averaging process. The inset in (B) shows a representative schematic of the three STM images. All calculated probabilities and occurrences are normalized. The Pd mole fractions used for the probability calculation is measured by STM in (A) and by LEISS in (B).

where ρ_{Pd} and ρ_{Au} are the probabilities of finding a Pd and Au surface atom, respectively, *m* is the number of degenerate configurations, and *n* is the number of nearest-neighbor Pd atoms. For a complete random distribution, $P(C)$ depends only on the surface concentration of each metal. Therefore, the respective surface mole fractions observed by LEISS ($\chi_{Au} = 0.9$, $\chi_{Pd} = 0.1$) can be used as ρ_{Au} and ρ_{Pd} for AuPd(100). The results of the first 11 most probable configurations are displayed in Figure 29 as solid blue bars. A complete list of calculated $P(C)$ for $\chi_{Pd} = 0.1$ as well as the systematic method used to categorize them can be found in Figure 30. The same $P(C)$ calculation is performed for the image acquired previously by Achoff et al.[140] Here, the mole fractions ($\chi_{Au} = 0.86$, $\chi_{Pd} = 0.14$) measured directly from the image are used. It should be noted that each configuration shown in Figure 29 represents one of many equivalent configurations.

For the observed distribution, Pd atoms of the same and equivalent eight nearest-neighbor configurations are totaled as occurrences, which are displayed on top of the respective calculated probabilities as transparent bars in Figure 29. For Figure 29A, this was done for a single image acquired previously by Aschoff et al.[140] For Figure 29B, each occurrence is the average of the respective measurements of three STM images (all 10 nm × 10 nm) acquired over different surface regions. The individual measurements of these images are also displayed in Figure 29B as colored triangles. All probabilities and occurrences are normalized and shown as percentages. No Pd with $C > 11$ is observed.

The charts in Figure 29 illustrate that the two surfaces of interest have markedly different Pd distributions. The distribution of $Au_3Pd(100)$ (Figure 29A) follows the

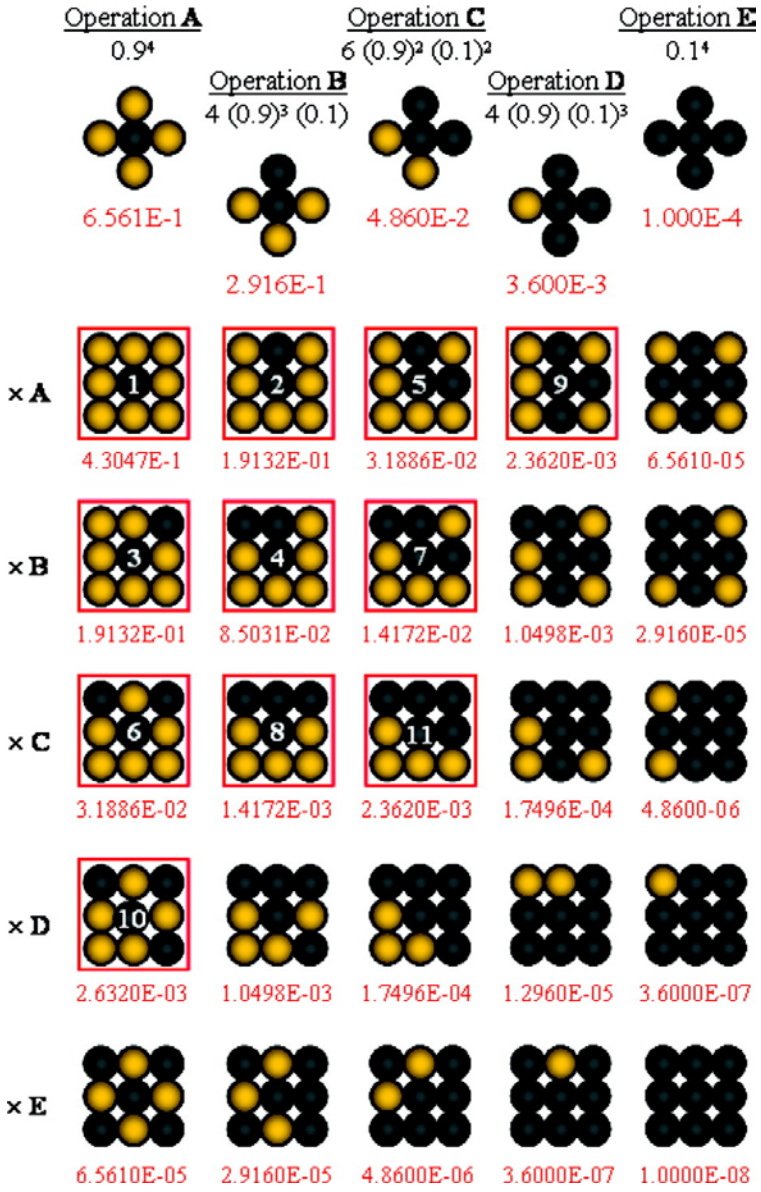

Figure 30. Calculation of the probability of finding a Pd surface atom surrounded by its eight nearest-neighbors in a specific configuration, using eq 5.2 (see text). The calculations are made for a surface with 0.9 ML Au and 0.1 ML Pd, assuming a complete random distribution. The top row of the figure shows the schematic of the configurations with the first four nearest-neighbors only. Operations A-D used to calculate the probabilities are shown in black above the schematics, and the resulting probabilities are shown in red below the schematics. The bottom of the figure lists the probability calculation including the next four nearest-neighbors. The red squares indicate the 11 configurations with the highest probabilities. These are the configurations listed along the *x*-axis in both Figures 30 and 32. The numbers on the central Pd atoms assign the descending order of calculated probability magnitude.

calculated random distribution quite well, while the distribution of AuPd(100) (Figure 29B) shows a clear preference for configurations 3 and 6, both of which involve Pd atoms arranged in local c(2 × 2)-like structures exclusively. The occurrences of all other configurations in Figure 29B are well below the calculated random probabilities.

Figure 29 also provides a sense of uniformity of the AuPd(100) Pd surface distribution. While only a single STM image is used to compile Figure 29A, three images acquired over different surface regions are used to compile Figure 29B to compensate for the local nature of STM. From the individual occurrence measurements (colored triangles in Figure 29B), it is clear that the preference for configurations 3 and 6 is present over all three regions. Moreover, focusing on configurations 3 and 6, a higher count of one configuration is accompanied by a lower count of the other. This is an indication that the number of monomer-pair active sites (Figure 26A) is also uniform across the surface. A monomer-pair count for each image yields 35, 36, and 29 sites for Images 1−3, respectively, averaging to 33 ± 4 sites/100 nm^2. It should be noted that the standard deviation of this average monomer-pair count is well within experimental error, as the actual configuration for Pd atoms located at the edge of the STM images is unknown.

A similar monomer-pair count for the image of $Au_3Pd(100)$[140] yields 25 sites/100 nm^2. Taking into account the surface Pd composition, the number of monomer-pair sites per surface Pd atom amounts to 0.27 and 0.15 sites/Pd for AuPd(100) and $Au_3Pd(100)$, respectively. From these observations, we conclude that the AuPd(100) surface presented here has a uniform, nonrandom Pd surface distribution with a preference for

local c(2 × 2)-like Pd arrangements. Per surface Pd atom, this type of Pd surface distribution yields almost twice the number of the targeted Pd monomer-pair sites when compared with a surface with random Pd distribution.

To demonstrate the relevance of our findings, it is important to understand the order−disorder transformations in binary bulk alloy single crystals.[139] [8] For these solid solutions, the terms “order” and “disorder” do not refer to the crystal lattice but are used to describe the relative arrangement of the two atomic species within the lattice. More specifically, complete disorder means that the probability for an atom of species *x* finding a neighboring atom of species *y* at a specific distance *d* (*P*(*x*,*y*,*d*)) is random (*P*(*random*)), while a higher degree of order means a significant deviation of *P*(*x*,*y*,*d*) from *P*(*random*). This type of chemical ordering is a function of thermodynamics and is dependent on the atomic size of the metal components, as well as the interatomic interactions between the components.[149]

In solid solutions there are two types of chemical order, namely short-range order (SRO) and long-range order (LRO).[139] The distinction between the two is first a spatial one. From the atomic perspective, if the deviation of *P*(*x*,*y*,*d*) from *P*(*random*) drops rapidly with distance, the order is short-range. For LRO, the deviation of *P*(*x*,*y*,*d*) from *P*(*random*) must remain constant for a long enough distance such that the symmetry of the crystal is lowered. Therefore, it follows that LRO can be detected in X-ray diffraction (XRD) data as superlattice reflections. SRO, which only affects the background scattering of XRD, is usually measured by X-ray diffuse scattering (XDS).

A second distinction between SRO and LRO is thermodynamic in origin. LRO is only present below a critical temperature (T_c), while SRO may or may not exist above T_c. This is illustrated by the phase diagram in Figure 31.[150] While the two types of order relate to bulk binary alloys, the same ideas can be applied to their surfaces, as both LRO and SRO had been previously observed by proximal probes.[151-153]

The different surface Pd distributions of AuPd(100) and Au_3Pd(100) result from two factors, namely bulk composition and surface preparation. This point is illustrated by the red shaded area in Figure 31. The red shaded area indicates the usual annealing temperature range for metal crystal preparation, which falls between the T_c of both AuPd and Au_3Pd. For the AuPd(100) in this work, the sample was sputtered at room temperature and annealed at 550 °C without sputtering for 30 min to allow equilibration before imaging at room temperature. The low concentration of surface Pd (10%) is due to Au surface segregation caused by the difference in the surface energies of the metallic species.[145] The equilibration time allows both surface segregation and SRO to reach completion, explaining the deviation of the observed Pd surface distribution from the calculated random distribution (Figure 28B). The fact that the sample was annealed above T_c has a crucial thermodynamic implication; i.e., the sample preparation method excludes the presence of LRO but permits SRO, as shown in our STM images.[154]

Due to its lower bulk Pd concentration, a similar treatment of a Au_3Pd(100) sample yields a surface free of Pd atoms,[140] instead of the desired long-range c(2 × 2) structure as suggested by Figure 31, which indicates LRO at the preparation temperatures below T_c. To counteract the effects of Au surface segregation, Aschoff et

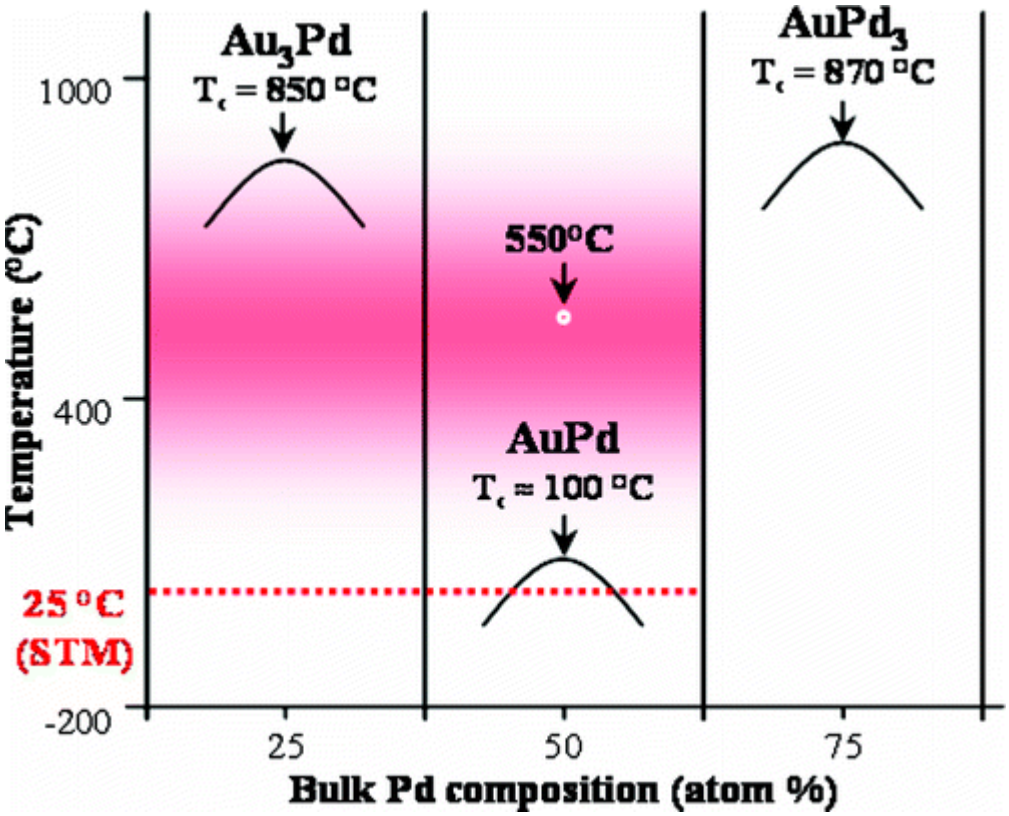

Figure 31. Partial temperature-composition phase diagram of AuPd solid solutions based on ref 150, below the melting point. The curved lines show the order-disorder phase boundaries of the alloy at various compositions. The red shaded area represents the usual sample annealing temperature range during sample preparation. This temperature range encompasses the actual annealing temperatures for both AuPd(100) from this work and $Au_3Pd(100)$ from ref 140. The white circle in the AuPd phase indicates the actual annealing temperature for the AuPd(100) sample preparation in this work. The red dotted line shows room temperature, at which all STM images were acquired.

al. used differential sputtering, consisting of sputtering the surface while annealing, preferentially removing the surface segregated species.[90] In the case of $Au_3Pd(100)$, Au is preferentially removed, leaving the layers near the surface Pd-rich. During sample cooling, Au atoms resurface by diffusion, but the process is quenched before both surface segregation and SRO can reach equilibrium. The random distribution of surface Pd atoms seen in Figure 29A reflects this process.

From these observations, we propose that the thermodynamic properties of AuPd alloys can be used to tailor surface ordering. Choosing the (100) face of the bulk alloy allows for the formation of Pd pairs of the right distance for promoting VA formation; opting for a higher bulk Pd composition reduces the effects of surface segregation. In addition, the unusually low T_c of AuPd (Figure 31) provides a wide temperature range where regular crystal preparation methods can be used to fine-tune the degree of surface SRO. To this end, our LEISS data indicate that the Pd surface concentration does not decrease monotonically with increasing annealing temperature but does so in a stepwise fashion. Figure 28B shows there is no significant change in surface Pd concentration for annealing temperatures ranging from 375 to 550 °C. However, the degree of SRO within this temperature range had been previously demonstrated by XDS to be temperature-dependent.[155] According to Ivernova et al., the degree of SRO in a AuPd 1:1 mixture increases with temperature from T_c to peak near 500 °C. This means that on a (100) surface of a AuPd 1:1 bulk alloy, both the activity and selectivity for catalytic reactions such as VA synthesis can be systematically controlled. We have shown that annealing the crystal between 375 and 550 °C yields a surface with 10% surface Pd atoms. In

principle, within this temperature range, the degree of SRO, i.e., the number of desired catalytic sites, can be maximized by a specific annealing temperature. Further work is needed to determine the ideal temperature.

It should be noted that the temperature–composition phase diagram shown in Figure 31 only addresses the bulk of the AuPd alloys. In addition, it is well-known that the concentration profile near the surface of a bulk binary alloy is not uniform due to surface segregation.[156] This brings up the possibility that the phase diagram of the alloy surface might be different from that of the bulk. However, although the exact relationship between the thermodynamic properties of the surface and that of the bulk cannot be inferred directly, this work demonstrates that such a relationship not only does exist, at least for the AuPd system, but it can also be utilized for enhancing the concentration of targeted active sites.

With regard to industrial AuPd catalysts, the formation of AuPd alloy crystallites had been previously demonstrated by XRD and transmission electron microscopy.[81,157] Furthermore, our group had verified the presence of both (111) and (100) facets of these AuPd alloy crystallites by infrared reflection adsorption spectroscopy on an industrial-like SiO_2-supported AuPd catalyst[79] (Figure 32). Based on this and our present observations, we propose that the role of the Au promoter in Au–Pd catalysts is twofold. First, the inert Au atoms separate the Pd surface atoms spatially, making the formation of Pd monomer-pair active sites with a 0.41 nm Pd–Pd distance possible over the (10 0) alloy crystal facets.[24] Second, the number of monomer pairs at the surface is thermodynamically controlled by the bulk crystallinity, bulk composition, and catalyst

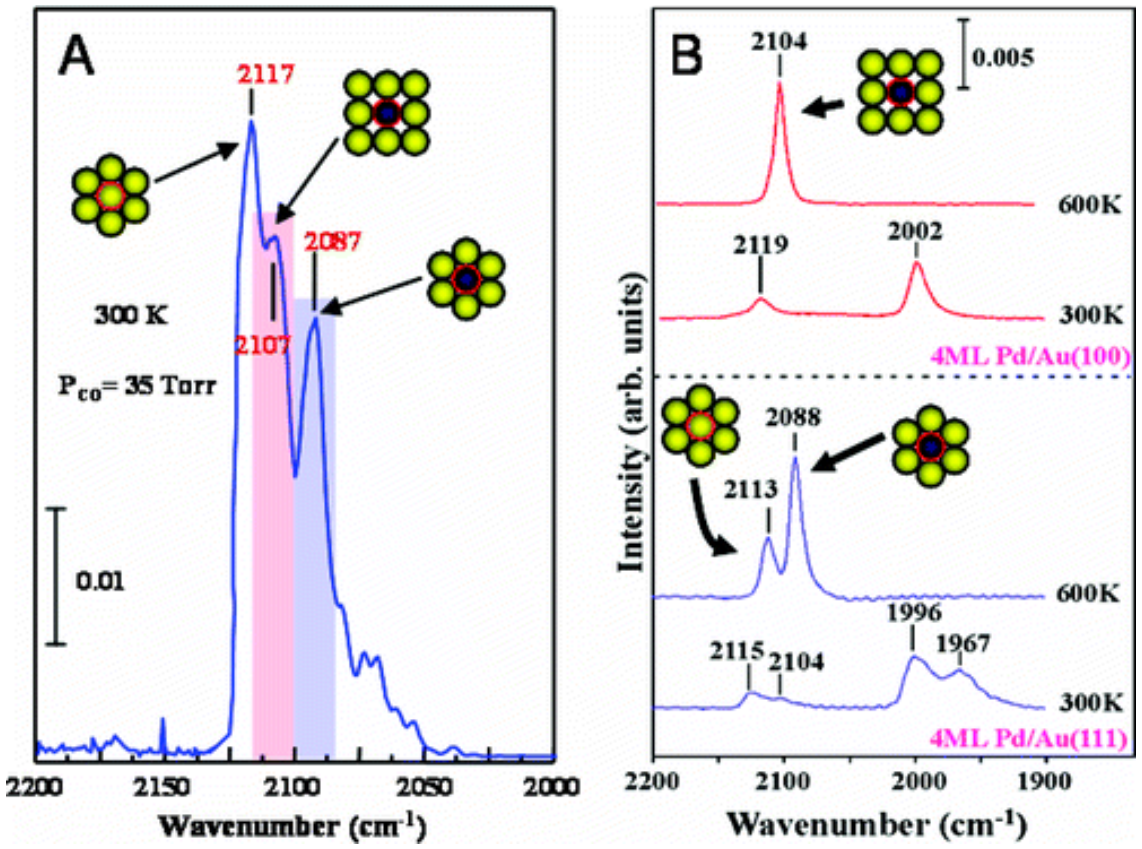

Figure 32. Infrared reflection absorption spectra for CO adsorption on: (A) SiO_2 supported AuPd catalyst; and (B) 4 ML Au on Pd(100) (top) and 4 ML Au on Pd(111) (bottom). Based on the assignments in (B) the signals at 2117 and 2087 cm^{-1} in (A) are assigned to CO adsorbed on Au and Pd within a (111) facet of AuPd alloy crystallites, respectively. Accordingly the signal at 2107 cm^{-1} is assigned to CO adsorbed on Pd within a (100) facet of AuPd alloy crystallites. The spectrum in (A) was acquired at 300 K with a background CO pressure of 35 Torr. Details of the spectra in (B) for CO adsorption on Pd/Au(111) and Pd/Au(100) can be found in ref 24.

temperature (throughout the life span of the catalyst). Therefore, in light of our proposed mechanism, further improvement is possible to optimize not only the reaction rate but also the selectivity of industrial AuPd catalysts. Fine - tuning the thermodynamic parameters can potentially change the degree of SRO, while leaving the total surface Pd atoms unchanged.[158] Finally, since this proposed mechanism relies exclusively on the fundamental thermodynamics of binary mixtures, the role of SRO, LRO, and surface segregation may be extensive in alloy catalysts. The control of SRO is a means of controlling the degree of randomness of the surface atomic distribution and, therefore, can be used to enhance other desired effects such as the ligand effect in a Ni/Au bulk alloy system[26 3] or the ensemble effect in Pd/Au bulk alloy systems.[24,45] These results have implications not only to mixed-metal catalysis but also to other technologies that rely on an atomic-level approach to alloy surface structures such as molecular self-assembly and molecular devices.[141-143]

Conclusion

We have used a combination of STM and LEISS to demonstrate that the surface Pd distribution of a AuPd(100) bulk alloy surface can be controlled by its thermodynamic properties. By choosing the bulk composition and preparation method of an fcc (100) bulk alloy single crystal, we have targeted a catalytic site of known atomic structure and have increased the coverage of the desired site known to enhance VA formation.[24] This effect is further confirmed by comparing the Pd surface distribution of our surface with that of a previously imaged AuPd(100) prepared with a different

scheme that favors a random Pd distribution.[140] Our method of assembling a targeted catalytic site is an additional tool toward bottom-up catalyst design.

6. SURFACE AND ELECTROCHEMICAL CHARACTERIZATION OF PT-CO ELECTROCATALYST

Pt-Co alloy thin film and nanoparticles electrocatalysts are characterized using low energy ion scattering spectroscopy (LEISS), X-Ray photoelectron spectroscopy (XPS), low energy electron diffraction (LEED), temperature programmed desorption (TPD), scanning tunneling microscopy (STM), electron diffraction spectroscopy (EDS) on transmission electron microscope (TEM), and electrochemical measurements in this section. This integrated approach is used to correlate the surface structure and compositional properties of Pt-Co alloy electrodes with the activity and stability of Pt-Co alloy electrodes towards oxygen reduction reaction (ORR) for fuel cell applications, as explained in the introduction section. Fuel cells are promising energy sources that combine zero emissions (except for water vapor) with the ability to convert chemical energy to electrical energy with high efficiencies. Among many different types of fuel cells, proton exchange membrane fuel cells (PEMFCs) show the highest promise for widespread commercial use. In PEMFC, the electrolyte is a solid proton conducting membrane which allows the cell to operate at a comparatively low temperature as well as to generate specific power (W/kg) and a power density (W/cm^3) higher than other types of fuel cells.[159] In the present construction of PEMFCs, Pt metals dispersed on a conducting support are the most widely used electrocatalyst materials for both anode and cathode. Major drawbacks in using Pt as the catalyst include high cost, sensitivity to contaminants, and Pt dissolution. Present-day researches have adopted two main goals in improving the electrode materials: increase the electrocatalyst efficiency and decrease

the amount of Pt employed.[160-167] It has been shown that alloying Pt with a less-noble metal increases the catalytic activity toward ORR while decreasing the Pt required for the same output power density. [59] Our work described here is focused on such Pt-based alloy, specifically Pt-Co bimetallic materials. The mechanism by which Pt-Co alloys, in particular Pt_3Co, promote greater activity toward oxygen reduction has been the subject of numerous studies. [61,63,166] Explanations include: (i) an increase in the *5d* orbital-vacancy in Pt [168]; (ii) changes in the interatomic distance and coordination number of Pt [67]; and (iii) dioxygen activation at (adjacent) Co sites [169]. However, there is still a lack of studies that have examined the influence of the structural and compositional properties of the alloy surface on catalyst efficiency are not as abundant.

In this study, to allow the observation of surface and electrochemical properties of Pt-Co alloy, Pt and Co films are prepared by vapor deposition under ultra high vacuum (UHV) conditions. Two types of Pt-Co alloy were prepared, *thin-film* and *clusters* of Pt-Co alloy.

The study is started off by analyzing surface properties and electrocatalytic activity of *thin film* Pt-Co. For thin-film Pt-Co study, multiple surface characterization techniques are employed. The main surface characterization technique used throughout this study is low energy ion scattering spectroscopy (LEIS). LEIS spectroscopy is unique in its ability to monitor the outermost surface layer since the repulsive character of ion-atom interactions serves to inhibit the interaction of the probe ions with sub-surface species. The surface versus bulk composition of Pt-Co thin films is assessed using this technique. The resulting surface phase diagram illustrates how the surface concentration

of Pt and Co varies from the bulk as the overall composition is varied. Other surface analysis techniques incorporated here are low-energy electron diffraction (LEED), X-ray photoelectron spectroscopy (XPS) and temperature programmed desorption (TPD). The study of thin-film alloy is then followed by combining surface characterization data with electrochemistry measurements, which will allow the correlation of the catalytic efficiency of Pt-Co toward ORR with the surface properties of the catalyst. The electrocatalytic efficiencies of various Pt and Co compositions are assessed. Finally, the stability of the alloy films has been tested at different applied voltages. Changes in the Pt-Co surface composition after each electrochemistry experiment have been monitored using LEIS and XPS. Preferential dissolution of Co is apparent and quantitatively assessed.

The study is than continued by preparing the other form of Pt-Co model alloy, which is Pt-Co *nanoparticle* or *cluster*. These clusters will be the better representation of the real high surface area Pt-Co alloy directly used in the fuel cell. For this model, Pt-Co clusters are supported on HOPG. The phase diagrams and electrocatalytic activity of this system are also studied and will be compared with the thin film Pt-Co system. In addition, energy dispersive x-ray spectroscopy (EDX) analysis were carried out. EDX spots were taken at different positions of the Pt-Co particles showing variations of chemical compositions throughout the particle. By comparing the Pt-Co particle before and after acid treatment, the change in chemical compositions throughout the particle is observed, and the dissolution of Co from the particle is analyzed. Scanning tunneling

microscopy (STM) works are also done in observing the effect of electrochemistry treatment on the stability of the structure of model Pt-Co clusters alloy.

Pt-Co Alloy Preparations

Thin films were prepared by physical vapor deposition in ultrahigh vacuum (UHV) as described previously.[77] A doser was constructed by tightly winding wires of Pt and Co metals in small segments around Ta filaments. The filament is resistively heated at a sufficiently high current to initiate sublimation of the desired metal onto a cold metal single crystal substrate. For Pt-Co clusters, Pt and Co metals were deposited onto an HOPG sample with a submonolayer amount of Pt or Co, to achieve Pt-Co clusters alloy.

Calibration of the dosing (film-formation) rate was conducted via an "XPS breakpoint analysis"[170] In this procedure, a plot of the XPS intensity is obtained as a function of dosing time from submonolayer to full-monolayer coverages, see Figure 33. The point at which the slope changes marks the time at which a second monolayer begins to form. It is also taken as the total time (t_{ML}) required to deposit one full monolayer. In the preparation of an *n*-ML film, the total dosing time was simply equated to ($n \times t_{ML}$). At the end of each deposition, the alloy films were annealed at 900 K for 20 minutes to ensure that Pt and Co had become alloyed. Prior to and subsequent to the electrochemical experiments, interfacial composition was determined by LEISS, XPS or TPD, and surface structure by LEED.

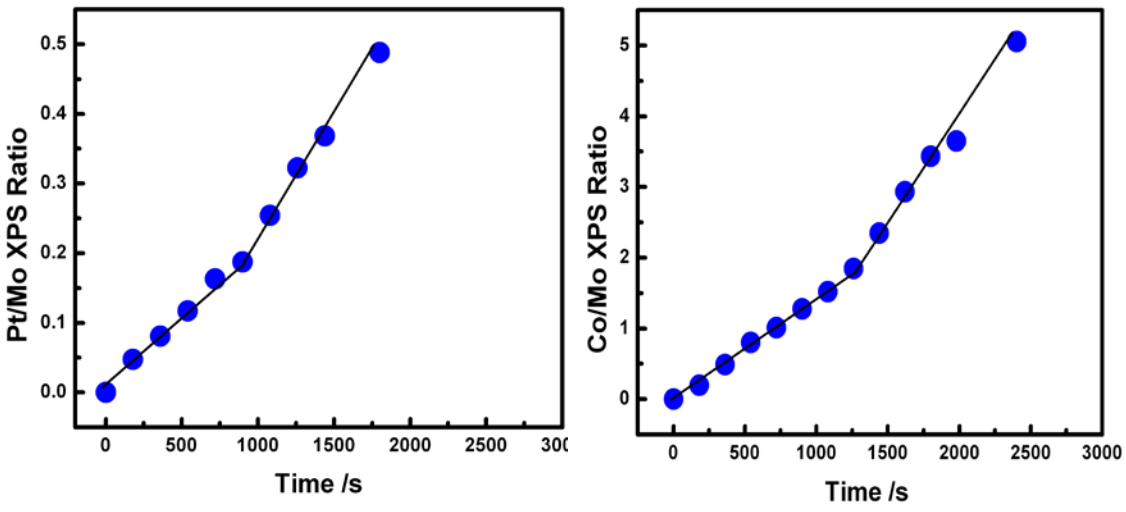

Figure 33. The "XPS break point" metal-doser calibration method. The point at which the slope changes (the "break point") signals the completion of one monolayer (ML) and the onset of the second monolayer. The data shown are for the Pt and Co dosers and a Mo(110) substrate.

Surface Characterization

Surface characterization experiments were carried out in an ultrahigh vacuum (UHV) chamber equipped with LEISS, XPS, temperature programmed desorption (TPD), and LEED with a base pressure of $5x10^{-10}$ Torr. The sample, mounted to two copper legs, could be heated to 1500 K resistively and to 2400 K by e-beam. Cooling of the sample to 90 K was possible via a liquid nitrogen reservoir attached to the copper legs. The sample temperature was measured using a 5%Re/W-26%Re/W (C-type) thermocouple spotwelded to the backside of the sample.

LEIS experiments were carried out with a He+ beam of 1 keV and an incident angle of 45º. To avoid surface damage, only one LEIS scan was used to collect each spectrum. For XPS measurement, XPS data was collected using an Al K_α source with an incident angle of 45º with respect to the surface normal. Photoelectrons were collected and analyzed by a concentric hemispherical analyzer.

STM experiments were conducted at room temperature, using the Omicron STM1 in a separate vacuum chamber with the base pressure lower than 2.0 x 10-10 Torr. All images were scanned in the constant-current mode with an electrochemically etched tungsten tip. All bias voltages are reported with reference to the sample. The scanning conditions for all the STM images: bias voltage 1.0V, and tunneling current 0.1nA.

EDX analysis were done on Pt-Co nanoparticles in FEI Tecnai F20 G2 TEM equipped with energy dispersive spectrometer (EDS) and post-column Gatan Image filter. The TEM is equipped with field emission gun at a working voltage of 200 kV. Magnifications were calibrated using commercial cross-line grating replica and SiC

lattice images.[171] The samples were prepared by peeling the prepared Pt-Co nanoparticles formed on HOPG substrate with transparent adhesive tape and removing the tape with acetone following the method by Astana et al.[172] The adhesive tape is employed to peel off a few sheets of the graphene surface containing the Pt-Co nanoparticles. The tape was than transferred to a small clean vial and mixed with acetone. The adhesive tape dissolved and the attached HOPG layers separated from the tape. The HOPG layers containing Pt-Co clusters were then dispersed in absolute ethanol and deposited onto a carbon-coated copper grid.

Electrochemistry Methods

A solution of 0.1M high purity H_2SO_4, acquired from Sigma-Aldrich, was used as the electrolyte. All solutions were prepared using Millipore MilliQ water. UHP N_2 and O_2 were used for all indications. Experiments were conducted using an EG&G PARC model 273 potentiostat interfaced with a Windows PC running EChem software. A three-electrode assembly was used. A custom-built Ag/AgCl reference was used. When prepared, the sample was transferred through a differentially pumped sliding seal to a high-pressure chamber, held at positive pressure with either O_2 or N_2 gas, where electrochemical experiments were to be conducted, while maintaining UHV condition in the main chamber. The UHV chamber used in this experiment is represented in Figure 34.

Cyclic voltammetry (CV) collected at a scanning rate of 1 mV/s unless otherwise indicated. All potentials referenced are versus the reversible hydrogen electrode (RHE). The open circuit potential value of each composition is used as an indication of the

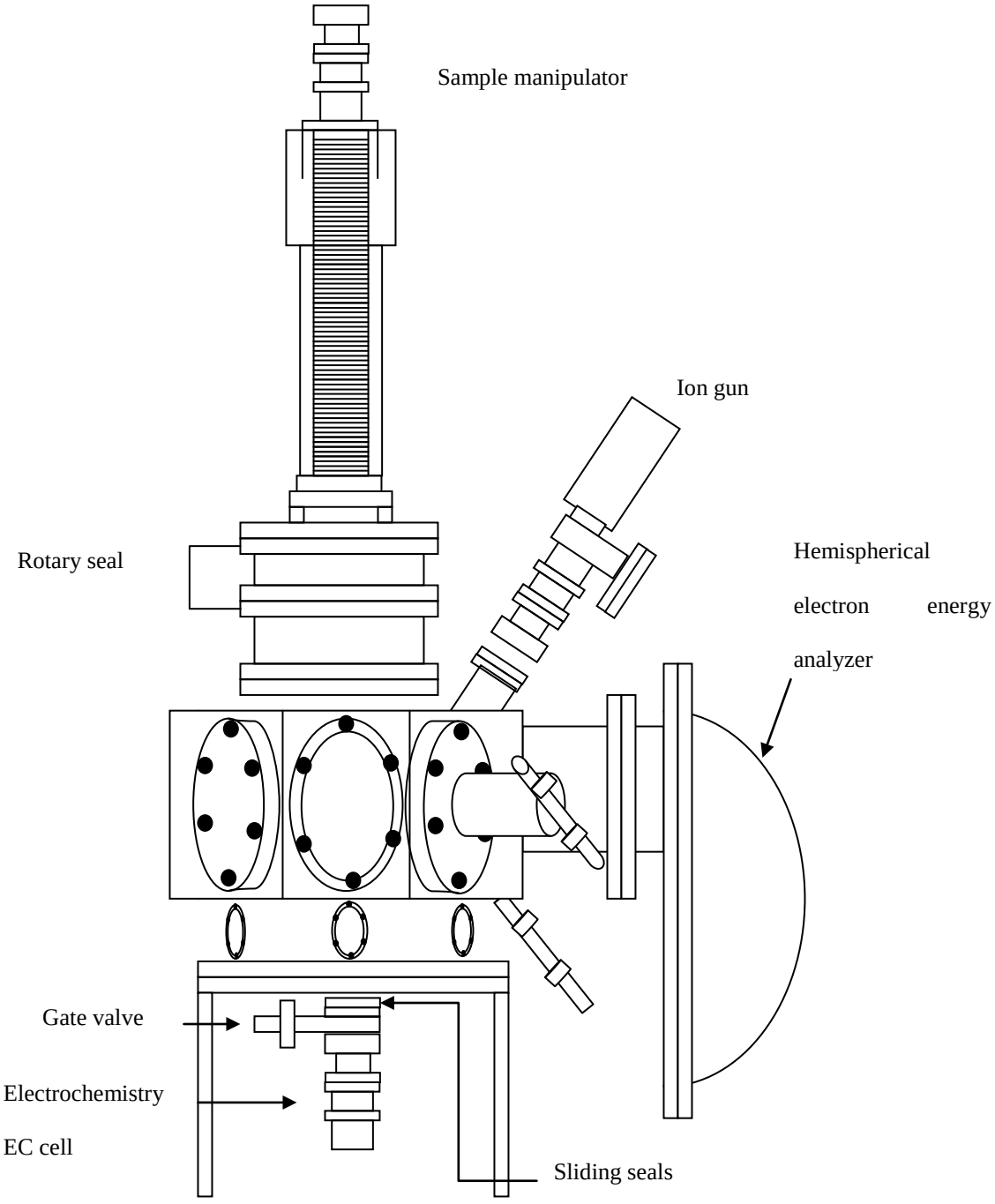

Figure 34. Schematic diagram of an integrated LEED-TPD-XPS-LEISS-EC apparatus.

efficiency (voltage) towards ORR. The *theoretical* OCP of an O_2-saturated cathode relative to a standard hydrogen electrode (SHE), would be 1.229 V. Since the magnitude of a hydrogen fuel cell voltage (E_{Cell}) is given by $E_{Cathode} - E_{SHE} = E_{Cell}$, an alloy electrode that yields on OCP closes to the thermodynamic value would be the best choice.

Pt-CoThin-film Alloy

LEIS Measurement

The first experiment performed was the determination of alloying temperature. Pt and Co were deposited onto a single metal substrate followed by annealing at different temperatures. Figure 35 shows LEISS spectra of a single metal substrate onto which a ten-monolayer film of a Pt-Co mixture, deposited in a 1:4 monolayer ratio, was heated to selected temperatures. In Figure 35a, 2 ML of Pt were deposited first, followed by 8 ML of Co. In Figure 35b, the reverse deposition sequence was used where 8 ML of Co were first deposited followed by 2 ML Pt.

There are five notable features in the data shown in Figure 35a. (i) Below 600 K, no Pt LEISS peak is observable; this indicates that 8 ML of Co completely cover 2 ML of Pt. (ii) At 700 K, a Pt peak emerges; this suggests that the Pt underlayer and the Co overlayer have started to intermix. (iii) In the temperature range between 800 and 1000 K, the ratio of the Pt and Co peak heights is invariant; this can be taken as evidence for the formation of a stable fixed-composition alloy. (iv) Below 1000 K, the fact that a Mo peak is not observed means that the alterations in the Co and Pt signals

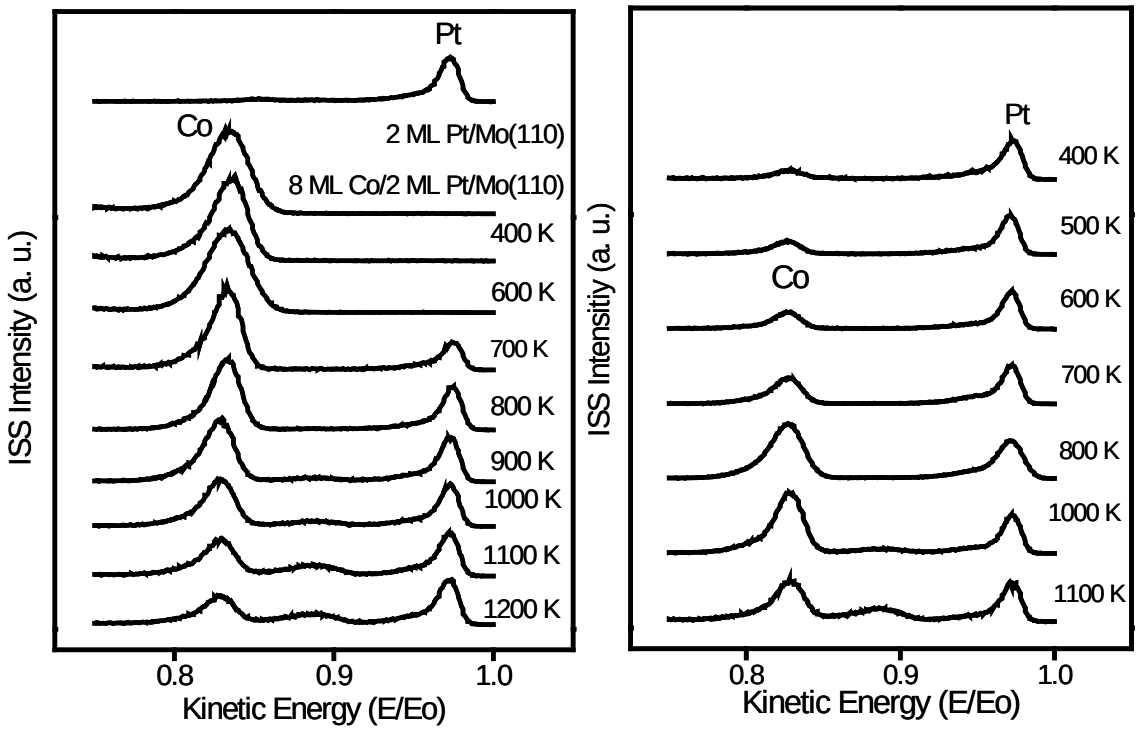

Figure 35. LEIS spectra of Pt-Co films on a Mo(110) substrate after a 30-minute treatment at the temperatures indicated. (a) 2 ML of Pt were deposited first followed by 8 ML of Co. (b) 8 ML of Co were deposited first followed by 2 ML of Pt. The peak at $E/E_0 \sim 0.83$ is due to Co; that at $E/E_0 \sim 0.98$ is for Pt. The LEISS spectra were collected at 300 K.

are due to alloy formation and not to thermal desorption. (v) At T > 1000 K, the peak intensities for both Co and Pt decrease and a peak for Mo emerges; all indicative of desorption of Pt and Co.

There are three notable features in Figure 35b. (i) Below 600 K, a LEISS peak for Co is observed; signifying that 2 ML of Pt is not sufficient to completely mask 8 ML Co. (ii) At temperatures between 800 and 1000 K, the peak-intensity ratios are identical to those in Figure 37. This shows that regardless of the order of metal deposition, the composition of the annealed (alloyed) film converges to the same value. (iii) Above 1000 K, spectra identical to those in Figure 35a are obtained in terms of the appearance of the Mo peak and the disappearance of both Pt and Co peaks.

Additional Pt-Co films were prepared, each consisting of a total of ten monolayers but with varying Pt:Co ratios (Pt:Co ratio of 1:9, 2.5:7.5; 5:5; 7.5:2.5; 8.8:1.2; 9.5:0.5). The results, in terms of LEISS spectra, are summarized in Figure 36. In every case, a stable top most-layer alloys was formed when the deposits were annealed at 1000 K. As apparent in Figure 36, the peak-intensity ratios were not invariant and depended upon the initial Pt:Co composition ratio.

Qualitatively, it can be readily deduced from the data in Figure 35 and Figure 36 that, in the alloyed state formed at 1000 K, the elemental composition at the *outermost* layer, as measured by the LEISS Pt:Co peak-intensity ratio, is vastly different from that in the *bulk*. These peak intensities can be quantitatively converted to surface concentrations.[74]

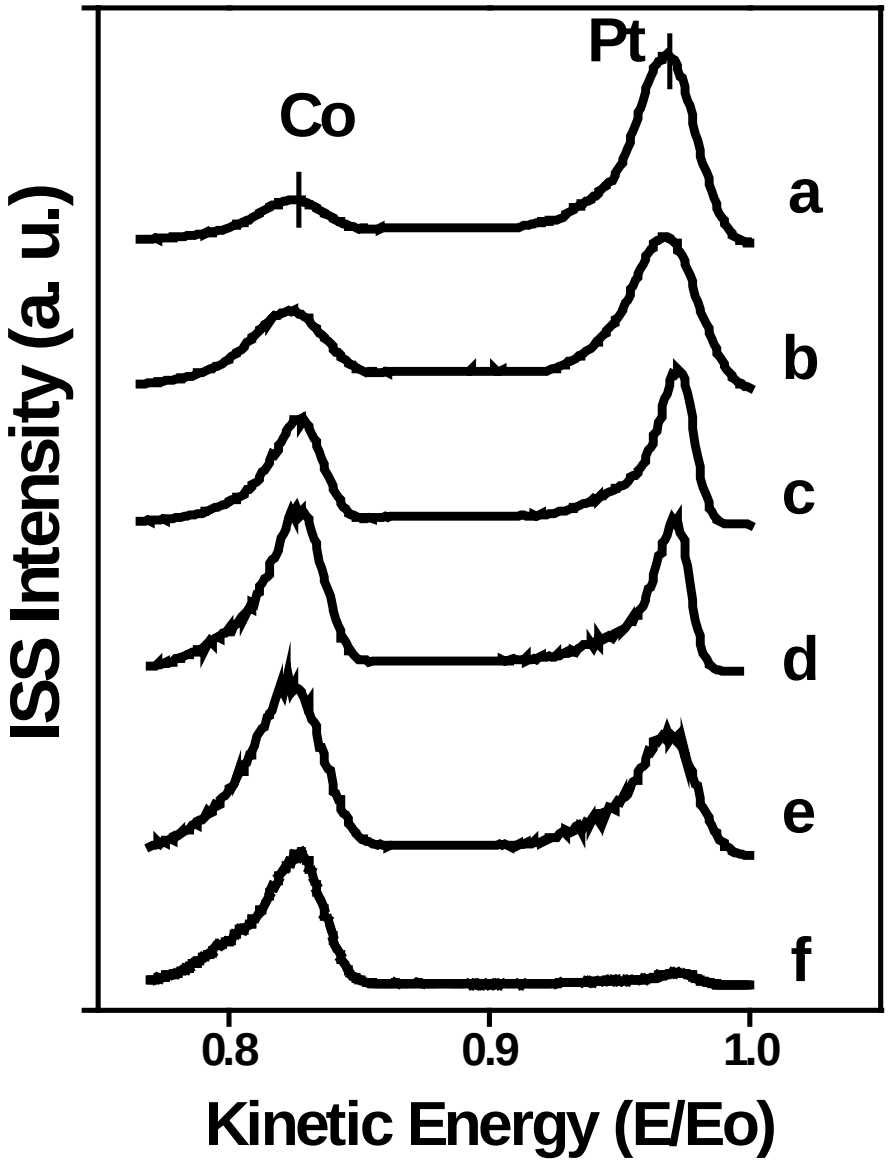

Figure 36. LEIS spectra of Pt-Co alloys at various bulk compositions annealed at 1000 K for 30 minutes. Each spectrum was acquired at 300 K. The ML(Co)-to-ML(Pt) ratios for the films were as follows: (a) 1:9; (b) 2.5:7.5; (c) 5:5; (d) 7.5:2.5; (d) 8.8:1.2; and (f) 9.5:0.5.

The divergence between the elemental composition at the topmost layer and that in the bulk is appreciated best when the *atom-percent* composition of Pt (or Co) at the alloy surface is plotted as a function of the *monolayer-percent* composition of Pt (or Co) in the bulk. Such a plot, which represents the phase diagram of the outermost-layer Pt-Co alloy, is shown in Figure 37. The open circles are data for when Pt was deposited initially, whereas the closed circles are for when Co was deposited initially. Three features in the plot are noteworthy. (i) The surface phase diagram is independent of the order or sequence of metal deposition. (ii) The convergence between the surface and bulk compositions occurs only when the bulk composition is almost entirely Co or is predominantly Pt. (iii) The discrepancy is most dramatic when the fraction of Co in the bulk is higher than 90%. For films in which the Co bulk composition is between 30% and 70%, the surface concentration of Pt is almost a constant at 70%. From these trends, we infer that: (i) Pt preferentially segregates to the surface, not unexpected since it has a lower surface free energy than Co; and (ii) for the interfacial alloy, the thermodynamically favored composition is essentially a 3:1 Pt-to-Co atom-percent ratio, Pt_3Co.

LEED Measurement

The two-dimensional order of the Pt-Co alloys was investigated by low-energy electron diffraction (Figure 38). The fact that distinct LEED spots are observed indicates that the alloy interface is well-ordered. Figure 38a shows the LEED pattern for alloys having Pt:Co atom-percent ratio lower than 3:1. Figure 38b shows a typical

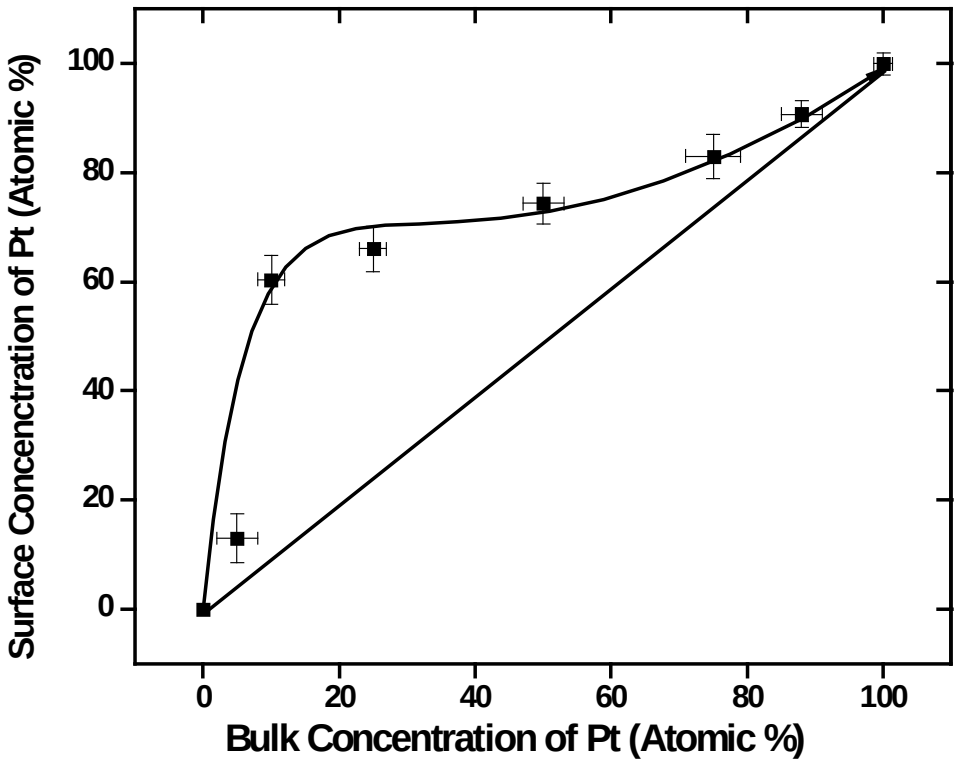

Figure 37. Surface phase diagram (atomic% of Pt at the outermost layer *versus* atomic% of Pt in the bulk) of the Pt-Co films after annealing at 1000 K for 30 minutes.

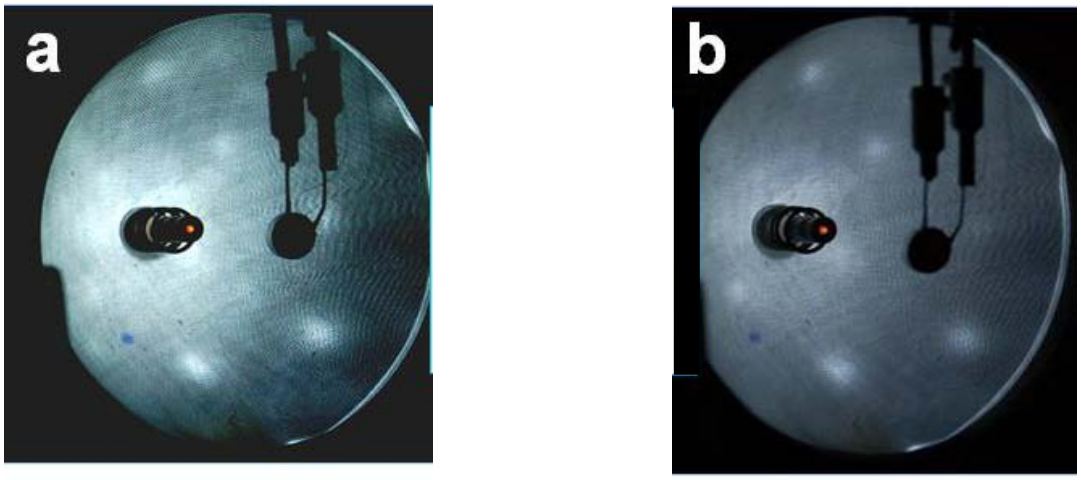

Figure 38. LEED patterns of the annealed Pt-Co alloys at points in the surface phase diagram where: (a) complex pattern is observed, and (b) hexagonal pattern, reminiscent of pure Pt(111) surface, is observed.

LEED pattern for alloys that contained 75 atom- percent of Pt; the hexagonal pattern is reminiscent of a pure Pt(111) surface. At such high Pt surface concentrations, the outermost layer is most likely populated by comparatively wide Pt(111) domains. Figure 38a shows that a different LEED pattern is obtained when the Pt:Co atom-percent ratio is lower than 3:1.

XPS Measurement

The electronic property of bulk Pt-Co thin film alloy was also studied. From the XPS spectra, a shift in binding energies of Co and Pt depends on the initial bulk composition of the Pt-Co alloy. The higher the initial amount of Co in the bulk, the larger the binding energy shift as can be seen in Figure 39. Toda et al. proposed that when Pt is alloyed with Fe-group metals, the 5d vacancy is increased, which could then be correlated with the activity of Pt alloyed with Fe-group metals.[60] It was observed that increasing shift in BE of Pt 5 d electrons occurs as the amount of Co (or the alloying metal) is increased. The XPS data we obtained in the study can be correlated with the proposed mechanism by Toda et al. It is observed that binding energy of Pt shifts about 0.3 eV when bulk Pt:Co is 3:1 (Figure 39). When the amount of cobalt is increased between Pt:Co 1:4 to 1:9 the binding energy of Pt shifts about 0.9 eV. When Co bulk amount is higher than 25%, the binding energy shift increases and approaches a constant value.

Electrochemical measurements

Figure 40 shows a plot of the open-circuit potential as a function of the alloy-surface composition in an O_2-saturated 0.1 *M* H_2SO_4 solution. The highest voltage, 0.86

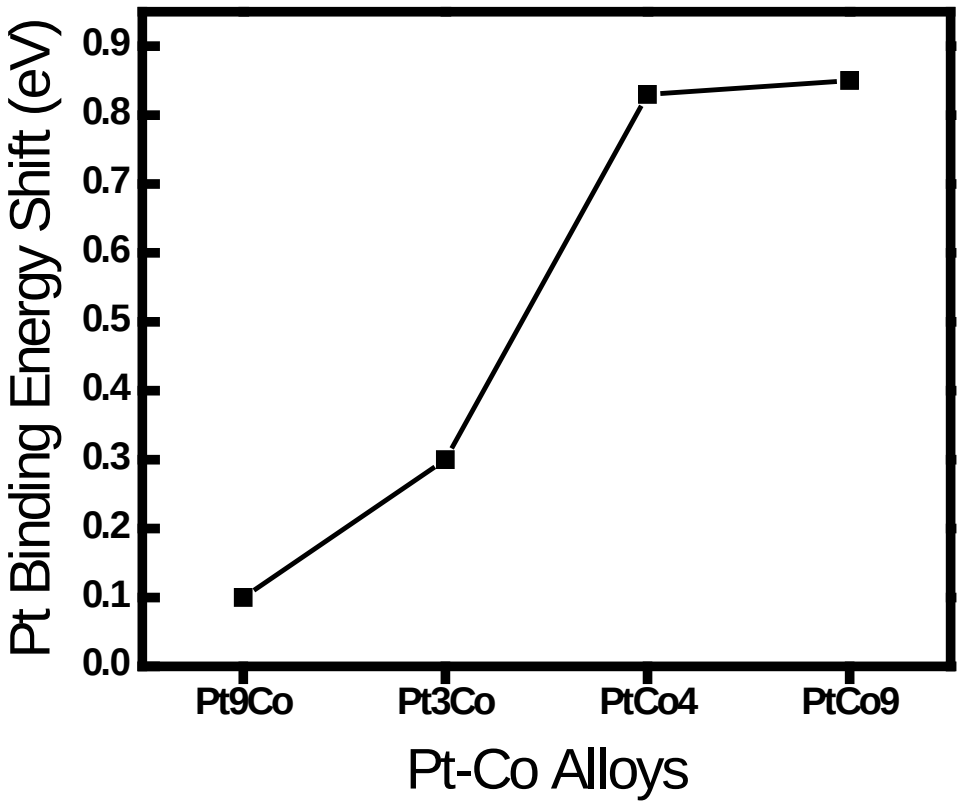

Figure 39. Pt XPS binding energy shift of Pt-Co for various alloy compositions.

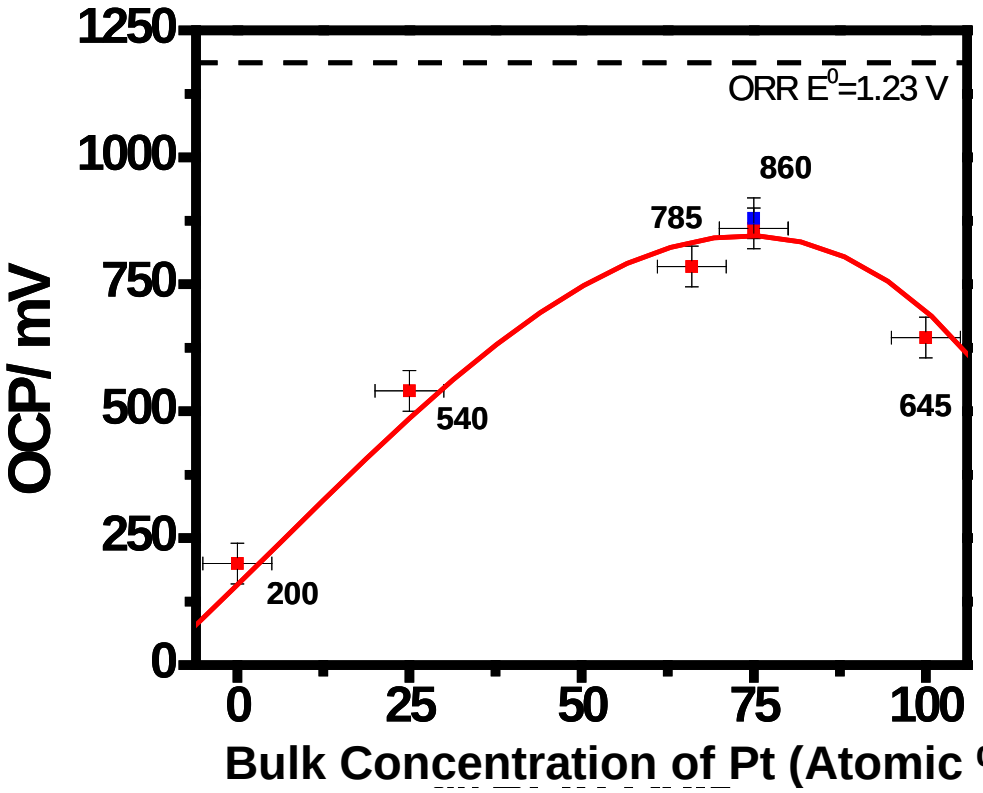

Figure 40. Measured open-circuit potential values as a function of the surface concentration (atomic%) of Pt.

V, was obtained for the alloy of composition that corresponded to Pt_3Co. This value is 0.68 V higher than that of pure Co and 0.22 V greater than that of pure Pt, yet considerably lower than the ideal potential of 1.229 V. In a control experiment, in which the sulfuric acid solution was thoroughly deaerated with ultrapure N_2, an OCP value (*ca*. 0.5 V) was obtained that was independent of the alloy surface composition.

From the cyclic voltammogram of pure Pt in deaerated 0.1 *M* H_2SO_4, it can be seen that 0.68 V represents the onset of surface oxide (or hydroxide) formation, although the amount formed is minuscule compared to that when the potential is at 1.229 V. In other words, even at saturation concentrations, O_2 gas is unable to oxidize a pure Pt surface even with the OCP driven to 1.229 V. The effect of Co clearly facilitates O_2 activation. It is further conjectured that the oxygen atoms formed on the Co sites irreversibly "spill over" to the Pt sites, increasing the amount of Pt-surface oxide and, consequently, also the OCP[173]. The present work suggests that the optimal Pt-Co surface concentration for such a synergistic process is Pt_3Co [174].

Cyclic voltammograms for alloys of varying Pt-Co concentration were collected in deaerated and O_2-saturated 0.1 *M* H_2SO_4. A single-cycle set of CVs for the Pt_3Co cathode is shown in Figure 41. The voltammograms were started from the OCP and the potential was initially scanned in the negative direction to the hydrogen evolution region. The morphologies of the current-potential curves are not too different from those of pure Pt. In deaerated solution, there is an appreciably wide double-layer "window" between the hydrogen evolution and oxygen evolution regions. In O_2-saturated 0.1 *M* H_2SO_4, a massive cathodic wave, due to the reduction of dioxygen, appears at potentials

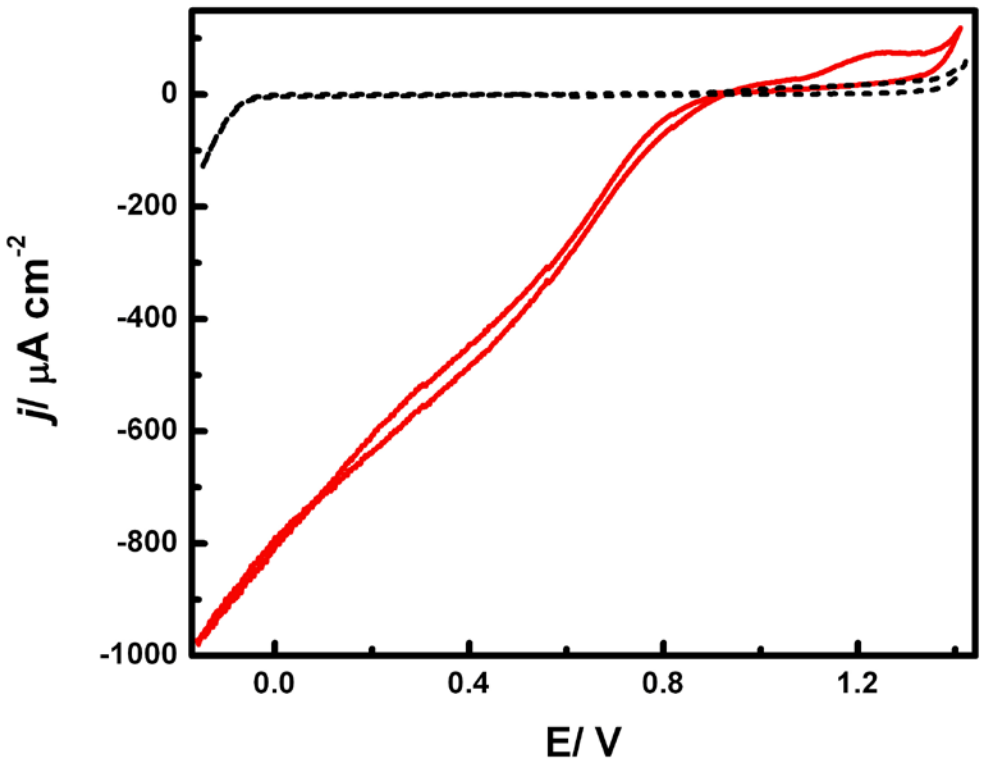

Figure 41. First-scan cyclic voltammograms for Pt_3Co in 0.1 *M* H_2SO_4. Dotted curve: deaerated (N_2-saturated) solution; solid curve: O_2-saturated solution.

immediately below the OCP. The high cathodic current persists even after the potential sweep is reversed in the positive direction. These results are not too different from those for pure Pt, as may be expected since two-thirds of the surface is made up of Pt.

Effect of Electrochemical Treatment on Pt-Co Thin Films

Little can be deduced about the nature of the alloy interface from only the cyclic current-potential curves. An important question that needs to be addressed is whether the cyclic voltammograms are accompanied by changes in the surface composition of the alloy. While a qualitative solution to this problem can easily be obtained from multiple voltammetric scans, a quantitative answer is fundamentally necessary. Therefore, the stability of the prepared alloy films was studied by observing the surface composition of the Pt-Co alloy by LEIS before and after the cyclicvoltammetry measurement. Initially, we observed that when collecting the CV of the Pt-Co thin film alloy with a potential window of 0 V to 1.4 V, Co is significantly decreased from both the surface and the bulk. Figure 42a and Figure 42b show the ISS and XPS data, respectively, of Pt-Co at before and after the CV measurements with a potential window of 0 V to 1.4 V. Both graphs show significant reduction of Co ISS and XPS intensity. However, when the potential window is decreased (0 V to 1.0 V), the loss of Co is diminished from both the surface and the bulk, as shown in Figure 42c and Figure 42d, respectively.

There have been studies conducted on the stability of Pt-Co. In 1990, Beard and Ross studied the stability of Pt_3Co carbon-supported alloy using EXAFS, XPS, XRD

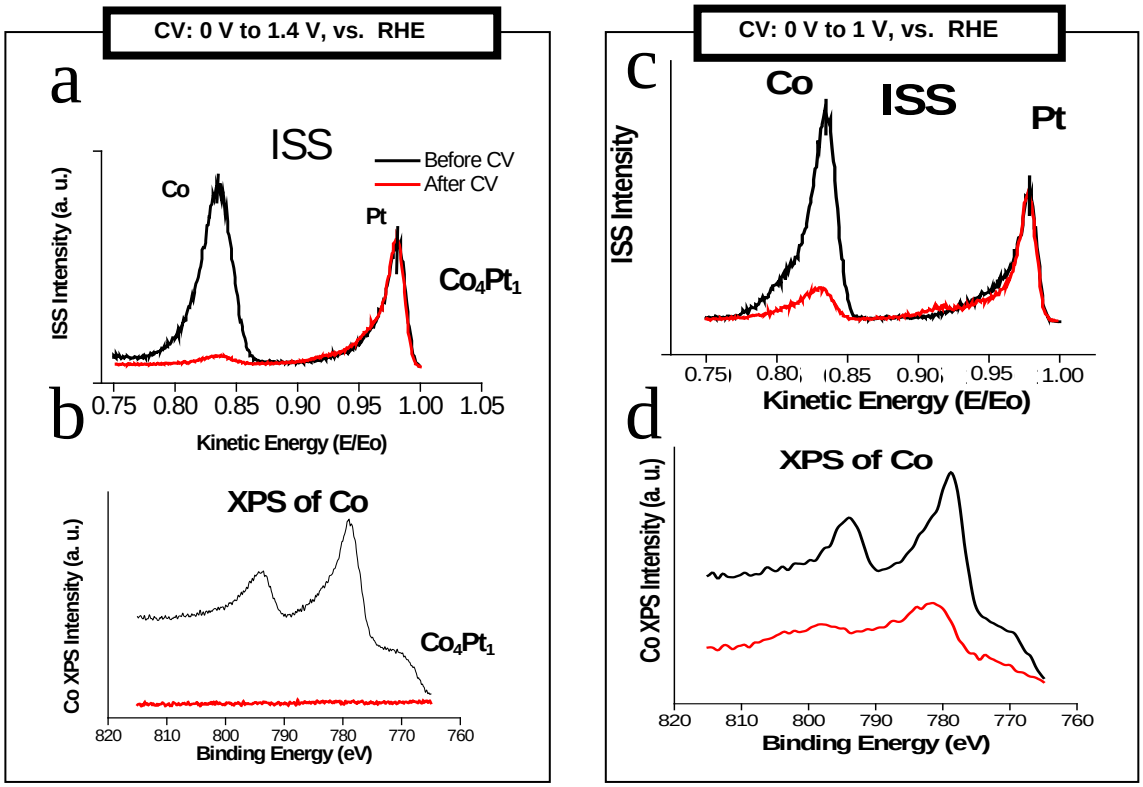

Figure 42. LEISS and XPS of Pt-Co (1:4 bulk ratio) taken before and after CV measurements at different potential window. (a). LEISS, and (b). Co XPS of alloys before and after CV at 0 V to 1.4 V. (c). LEISS, and (d) Co XPS of alloys before and after CV at 0 V to 1.0 V. The higher potential window shows significant Co dissolution

and XRF [61]. In their study, carbon-supported Pt-Co (3:1 atom ratio) catalysts were prepared in acid and alkaline aqueous media, followed by heat-treatments at 700, 900, and 1200 °C. They then performed the activity and stability measurements on the catalysts by calculating the current density at 0.9 V vs. RHE after applying a potential sweep from 0.9 to 0.6 V in O_2-saturated electrolyte followed by maintaining the potential at 0.6 V for 48 hrs. From the stability test, they observed Co loss from as-prepared catalyst (without annealing) and the annealed catalyst at 1200 °C as determined by XAF. The amount of Co loss is significantly higher from the as-prepared catalyst. The as-prepared catalyst shows a disordered alloy from XRD data, while the catalyst annealed at 1200 °C shows both the disorder and order alloy. It was proposed that Co loss is greater from the disordered alloy (as-prepared) compared to the ordered alloy (annealed). However, only one holding potential was applied to the catalysts to study the stability of Pt-Co alloy in their study.

Another stability study was done by Watanabe at al. [160] who studied the stability of ordered and disordered Pt-Co alloy as well as the change in catalytic activity of the alloys before and after stability test. The ordered alloy was prepared by annealing at 650 °C for 5 hours while the disordered alloy was prepared by annealing the ordered alloy at 850 °C for 15 minutes. They found that the activity of the ordered alloy is higher compared to the disordered alloy. However, after they applied treatment for the stability test (0.8 V vs. RHE, 205 °C in H_3PO_4), the activity of ordered alloy decreased 47% compared to 1% for the disordered alloy. Here, they proposed that the loss of Co occurs

from the surface and the bulk. The loss of Co from the bulk in the ordered alloy is more significant than in the disordered alloy.

The previous stability studies as described above so far have been carried out by applying potentials a single value. It is desirable to understand the behavior of the Pt-Co alloy under different holding potentials throughout the operating and cyclic voltammetry measurements ranges. Another critical matter involves the stability the Pt_3Co alloy under fuel-cell operating conditions; that is, after prolonged use at the OCP in an O_2-saturated solution. These issues can be simultaneously tackled if the surface composition of the Pt_3Co alloy is monitored as a function of time at a given applied potential. For such measurements, the alloy electrode is withdrawn from the O_2-saturated electrolyte at the test potential and, prior to transfer into the surface analysis chamber, rinsed in deaerated ultrapure (Millipore) water. The results are shown in Figure 43.

There are four important trends are to note in Figure 43. (i) Regardless of the applied potential, there is an immediate drop of *ca.* 10% of the original Co concentration. (ii) Regardless of the external potential, the surface concentration of Co becomes independent of time after the initial rapid decrease. (iii) At $E_{Applied} \leq E_{OCP}$, the Co surface concentration quickly converges to a constant value of approximately 18%. (iv) At potentials more positive than OCP, the initial decline in surface concentration is much more precipitous (from 20% to 11%) than at lower potentials (form 20% to 18%). However, the amount of Co retained is unchanged even after extended periods.

It can be seen in Figure 41 that the anodic oxidation of the alloy surface takes

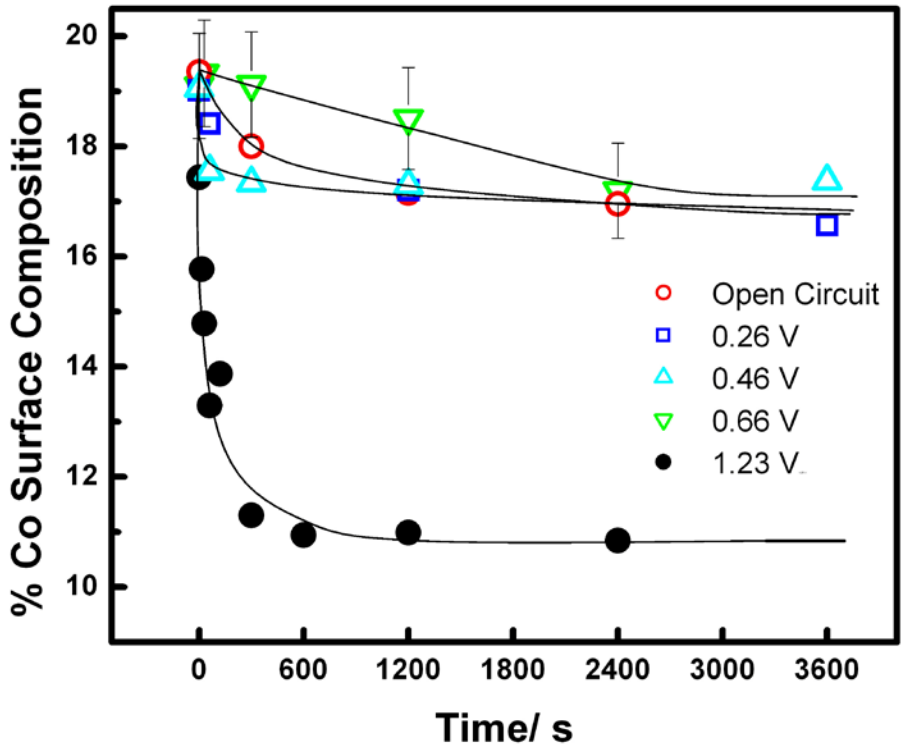

Figure 43. The dissolution profile of Pt_3Co in terms of the amount of Co that remains at the outermost layer as a function of applied potential and time.

place at potentials above the OCP. This may account for the observed 45% decrease in the initial Co surface concentration at $E_{Applied} > E_{OCP}$ because the oxidized surface of Co is not impervious to acid-driven dissolution. The fact that 55% of the initial Co concentration is retained on the surface suggests that an appreciable quantity of Co is rendered comparatively inert towards anodic dissolution when alloyed to Pt.

To show that Co dissolution occurs not only on the surface, but also the near-surface region, XPS and TPD measurements are presented. Figure 44 shows the XPS data for the 10 minute holding at different applied potential for Pt_3Co thin film. Between 0.6 and 1.1 V, the constant peak intensity before and after the potential holding experiment indicates that the (near-surface) bulk composition of Co does not change. However, when the potential is increased to 1.23 V (which is the thermodynamic value for oxygen reduction) a significant reduction of Co peak in the ISS (Figure 43) and Co XPS spectra (Figure 44), respectively, indicates that the amount of Co is reduced both from the surface and the bulk. Therefore, a significant fraction of the loss of Co was from the near surface.

Temperature programmed desorption (TPD) data also shows that Co bulk amount is reduced after the alloy electrode is held under 1.23 V potential. Figure 45 shows TPD of pure Co and Pt-Co alloy. Figure 45a shows pure Co TPD at different coverages, up to 20 ML. Figure 45b shows Pt-Co alloy TPD at different coverages before and after electrochemical treatment. Loss of Co from the bulk is observed after the alloy is treated with the electrochemical technique.

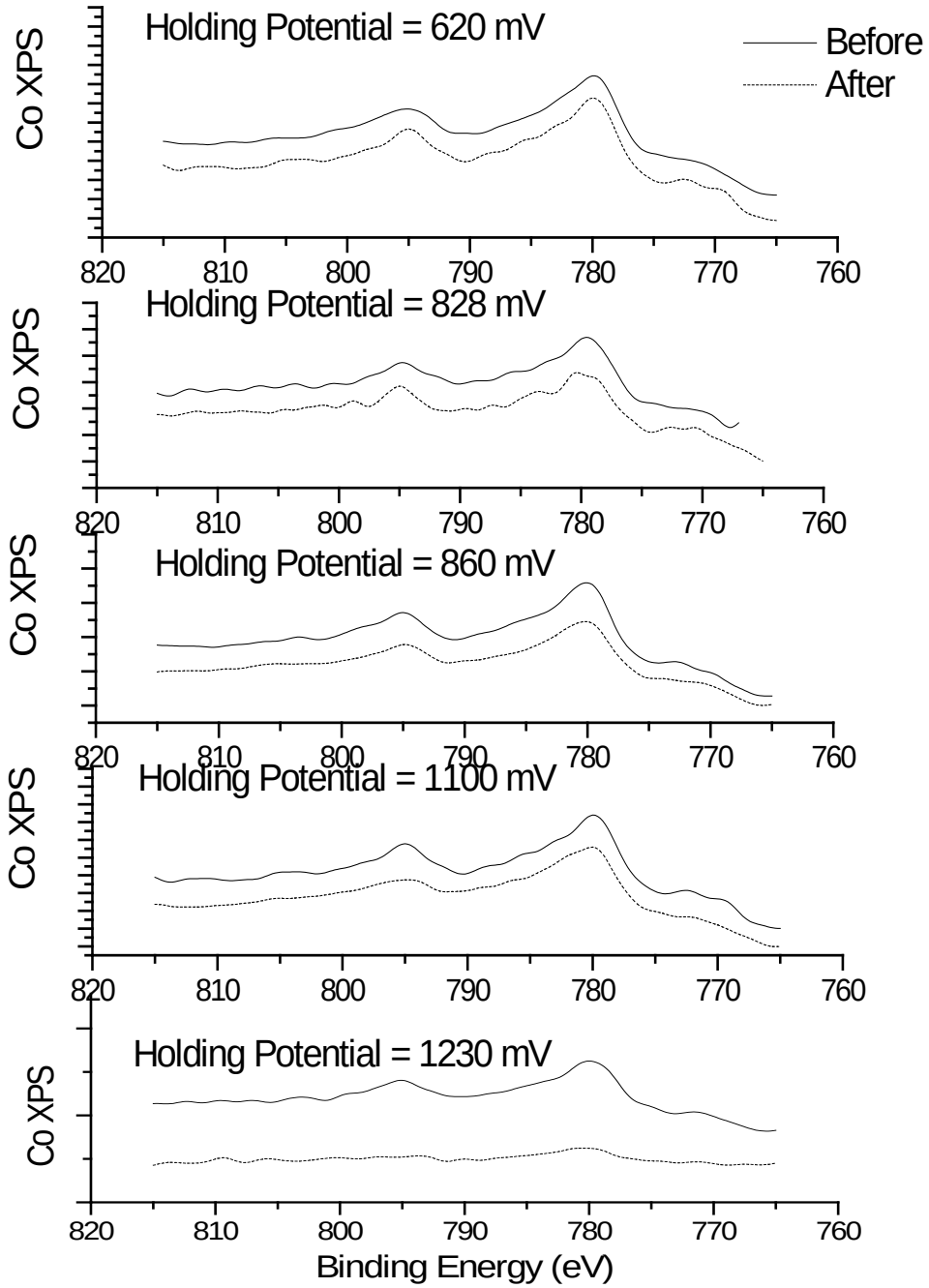

Figure 44. Co XPS spectra before and after stability study by dipping the sample in 0.1 M H_2SO_4 saturated with O_2 at different potential holding for 10 minutes.

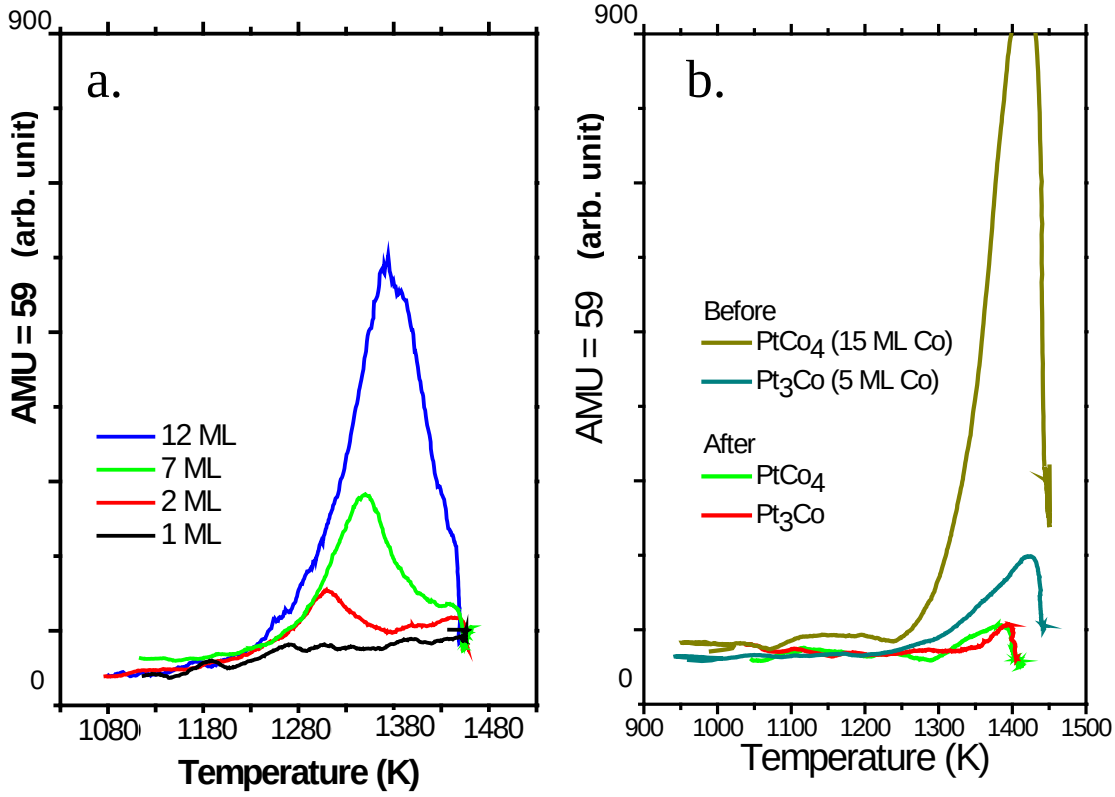

Figure 45. CO TPD of pure Co (a) and Pt-Co alloy (b).

Pt-Co Nanoparticles (Clusters) Alloys

The study presented earlier was done on Pt_3Co thin film deposited on a refractory metal substrate. To further validate the results on the planar system compared to high surface area Pt_3Co particles that are actually used in fuel cell system, it is desirable to do a comparison study with Pt_3Co particles. To prepare Pt_3Co particles, a HOPG substrate is utilized in this part of the study. The Pt_3Co surface phase diagram of the particles will be first studied and compared to the previous data observed from the planar surface. The electrocatalytic activity of Pt_3Co particles will then also be studied and compared. The last comparison study will be the stability of Pt_3Co by looking at the dissolution of Co.

The stability study of Pt_3Co particles shows correlation between electrochemical treatment and alloy activity. [175] It has recently been proposed that by treating Pt_3Co supported on carbon in acid electrolyte, a change in Pt_3Co particles composition is observed, followed by the observation of higher activity of Pt_3Co towards ORR when compared to commercial Pt/C catalyst.[176] However, no mechanisms on the increase of Pt_3Co activity towards ORR with the change of Pt_3Co composition affected by the electrochemical treatment have been proposed. In this part of the study, the Pt_3Co particles supported on HOPG will be used to observe the difference in surface composition, electronic properties and electrochemical activity of Pt_3Co caused by electrochemical treatment.

LEIS Measurements.

After depositing Pt-Co on clean HOPG, LEISS measurements were taken at

different Pt and Co bulk ratio to get the surface phase diagram of Pt-Co particles. Figure 46 shows the surface phase diagram of Pt-Co deposited on HOPG compared with previous data shown earlier from Pt-Co thin film deposited on refractory metal single crystal. For Pt-Co planar surfaces (green line), segregation of Pt to the surface as a function of Pt-Co bulk ratio is much more significant. From this surface phase diagram, both Pt-Co planar surface and clusters, the outermost surface layer is enriched significantly in Pt, with the surface concentration of Pt on Pt-Co planar surface being greater than that for clusters with an identical Pt-Co bulk ratio.

STM Measurement

In constructing the phase diagram, as shown in Figure 46, the deposited Pt and Co on HOPG substrate were first annealed to 900 K to achieve alloying condition between Pt and Co. LEISS measurements have shown that when deposited Pt and Co were annealed below 700 K, no stable surface composition is observed, as shown in Figure 35. However, stable surface composition is observed when the annealing temperature is between 800 and 1000 K. The same annealing experiment was also studied using STM. Figure 47a-h are STM images of Pt-Co clusters deposited on HOPG after annealing to different temperatures, showing the evolution of Pt-Co morphology. Figure 47a shows Pt particles deposited on HOPG at room temperature. Big Pt islands with smooth surface are observed. Figure 47b is the image of Co deposited on Pt/HOPG at room temperature. Round Co clusters dispersed on the surface indicate no alloying happen at this point.

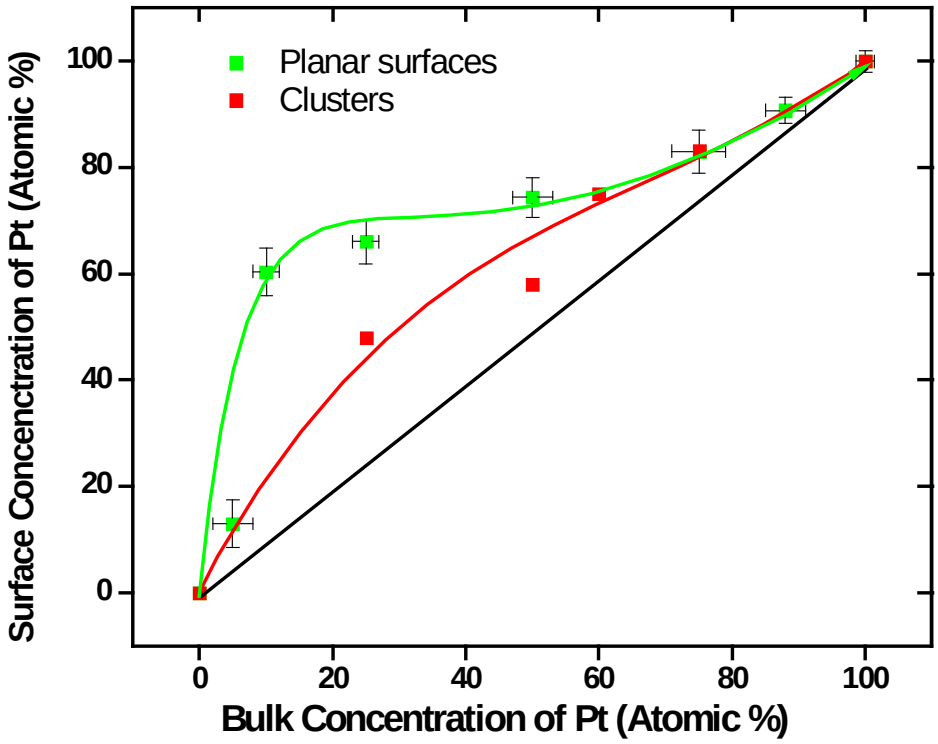

Figure 46. Surface phase diagram of Pt-Co planar surface (green line) and clusters (red line).

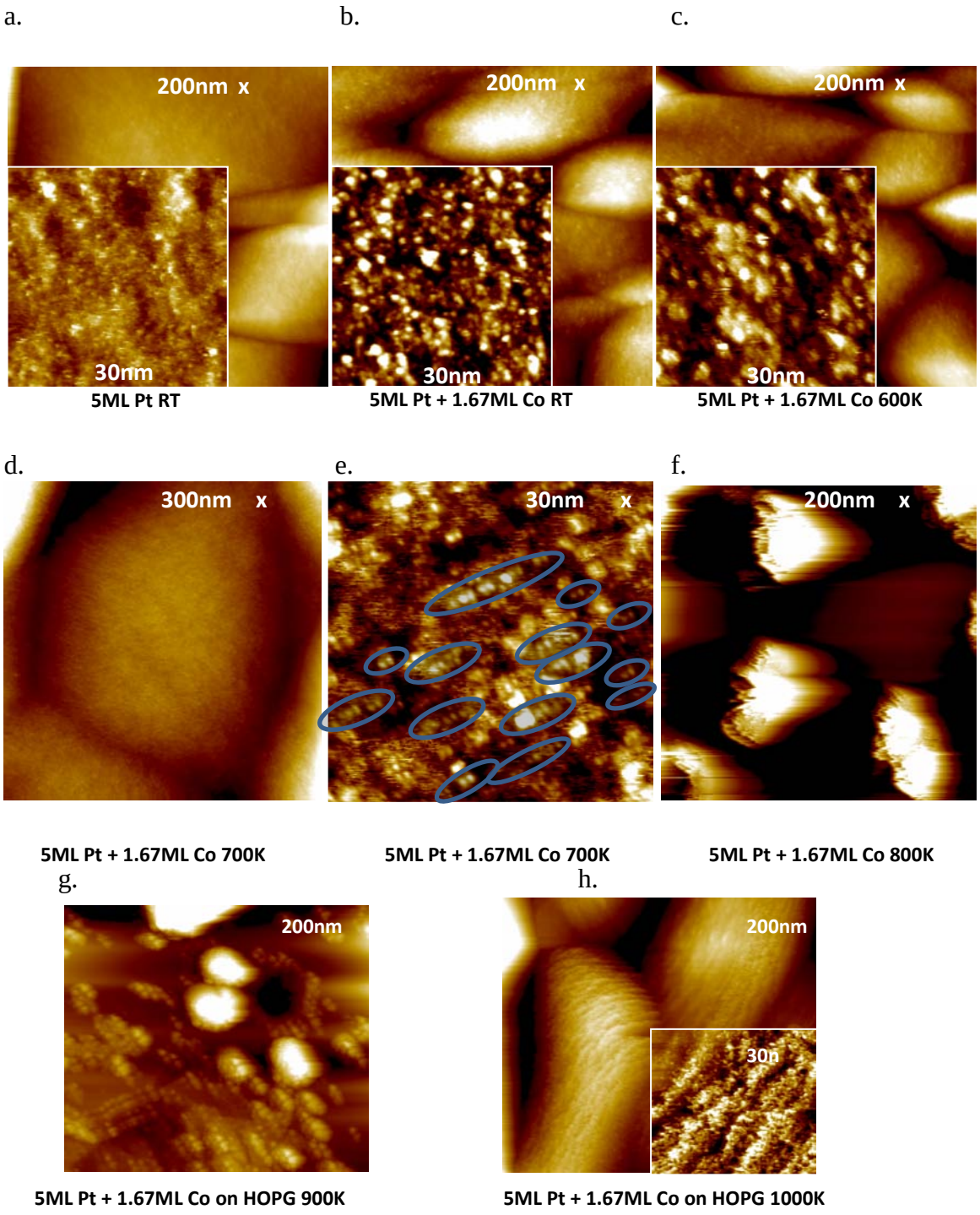

Figure 47. STM image of: a. 5 ML Pt on HOPG, b. 1.67 ML Co on Pt/HOPG at room temperature, c. annealed at 600 K, d. annealed at 700 K, e. enlarged d, f. annealed at 800 K, g. annealed at 900 K, h. annealed at 1000 K. The scanning conditions for all the STM images above: bias voltage is 1.0V, and tunneling current is 0.1nA.

When the system is annealed to 600 K, shown in Figure 47c, no significant change in the morphology of Pt islands is observed. However, the inset 30nm x 30nm image shows the density of the clusters decreases while the sizes of the clusters increase, which means Co clusters begin to sinter at 600K on Pt/HOPG surface. Figure 47d is the morphology of the surface annealed to 700K for 10 min, showing large islands formed on the surface. The close-up picture, Figure 47e, shows that small Co clusters are now arranged in a line, as indicated by the blue circles, which might be caused by the formation of well ordered Pt islands on the surface. When the annealing temperature reaches 800 K, Figure 47f shows big metal islands with the height higher than 10 nm are formed and the dark flat area is assigned to HOPG substrate because the HOPG pattern could be clearly seen in close-up STM images in those areas. The change in the morphology above 800 K should indicate that the alloying between Pt and Co has occurred. When the annealing temperature reaches 1000 K and above, Figure 47h shows a rough surface, which could indicate the diffusion of Co into the HOPG substrate. These STM images provide another proof that the alloying between Pt and Co starts when the system is annealed between 800 K and 1000 K.

Electrochemistry Measurements

To check the catalytic activity of Pt-Co clusters on HOPG, the same electrochemistry measurements as previously described for Pt-Co planar surfaces were also applied on Pt-Co/HOPG system. Figure 48a and b show the OCP values from planar surfaces and clusters, respectively. From the plot it is shown that Pt-Co planar surfaces and clusters show the same trend, in which Pt:Co having bulk ratio of 3:1 shows the

a.

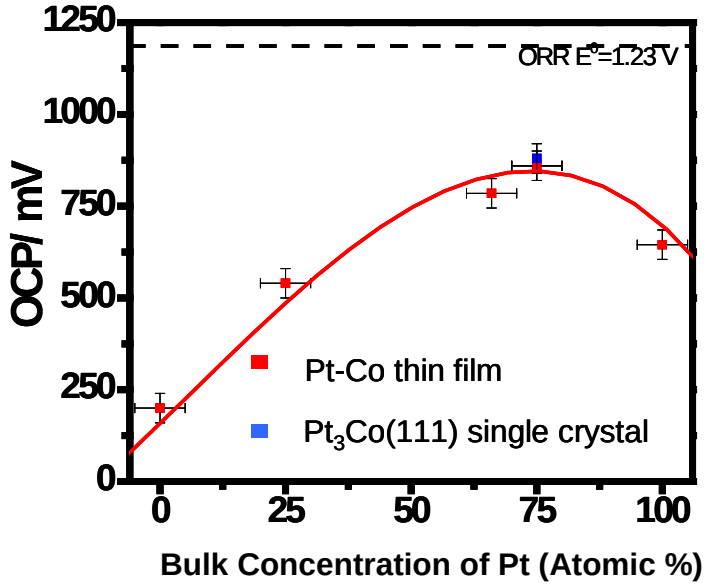

b.

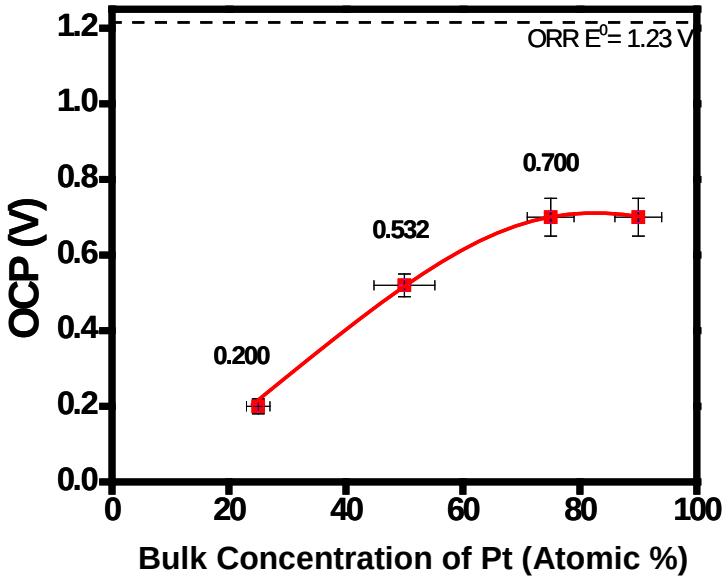

Figure 48. OCP value of Pt-Co planar surfaces (a) and clusters (b).

highest value for OCP, which here referred to as having the highest efficiency toward ORR.

Effect of Electrochemical Treatment on Pt-Co Clusters Stability

The next comparison study that was done was the dissolution of Co in the 0.1 M H_2SO_4 electrolyte. Initially, the goal in this part of the study is to check if Pt-Co clusters undergo similar Co dissolution as Pt-Co planar surfaces when treated with similar condition as summarized in Figure 43. Pt-Co planar surfaces show that Co dissolution occurs from the near surface and the amount of Co dissolution depends on the applied voltage. To further confirm that Co dissolution occurs when the system is treated in acid electrolyte, elemental analysis on Pt-Co particles was done using TEM equipped with EDS . EDX spots were taken at different points of the particles. By evaluating the change in Pt to Co intensity ratio from EDX plot, the variation in chemical compositions throughout the particle is observed. Figure 49 shows the TEM image of Pt_3Co annealed to 900 K without any acid treatment. The inset shows the peak area of Pt M and Co K-α energies calculated from the EDX plot. It is observed that, more Co is found in the core of the particles compare to the surface of the particle. Therefore, based on the ratio of Pt to Co EDX peak area, more Pt is found on the surface, which agrees with the surface phase diagram constructed from LEISS data. Figure 50 shows the TEM image of Pt_3Co after acid treatment. The inset shows the peak area of Pt M and Co K-α energies calculated from the EDX plot. It is clearly seen that there is a significant reduction of Co amount, hence increase in Pt to Co ratio. Also, higher Pt to Co ratio is found on the

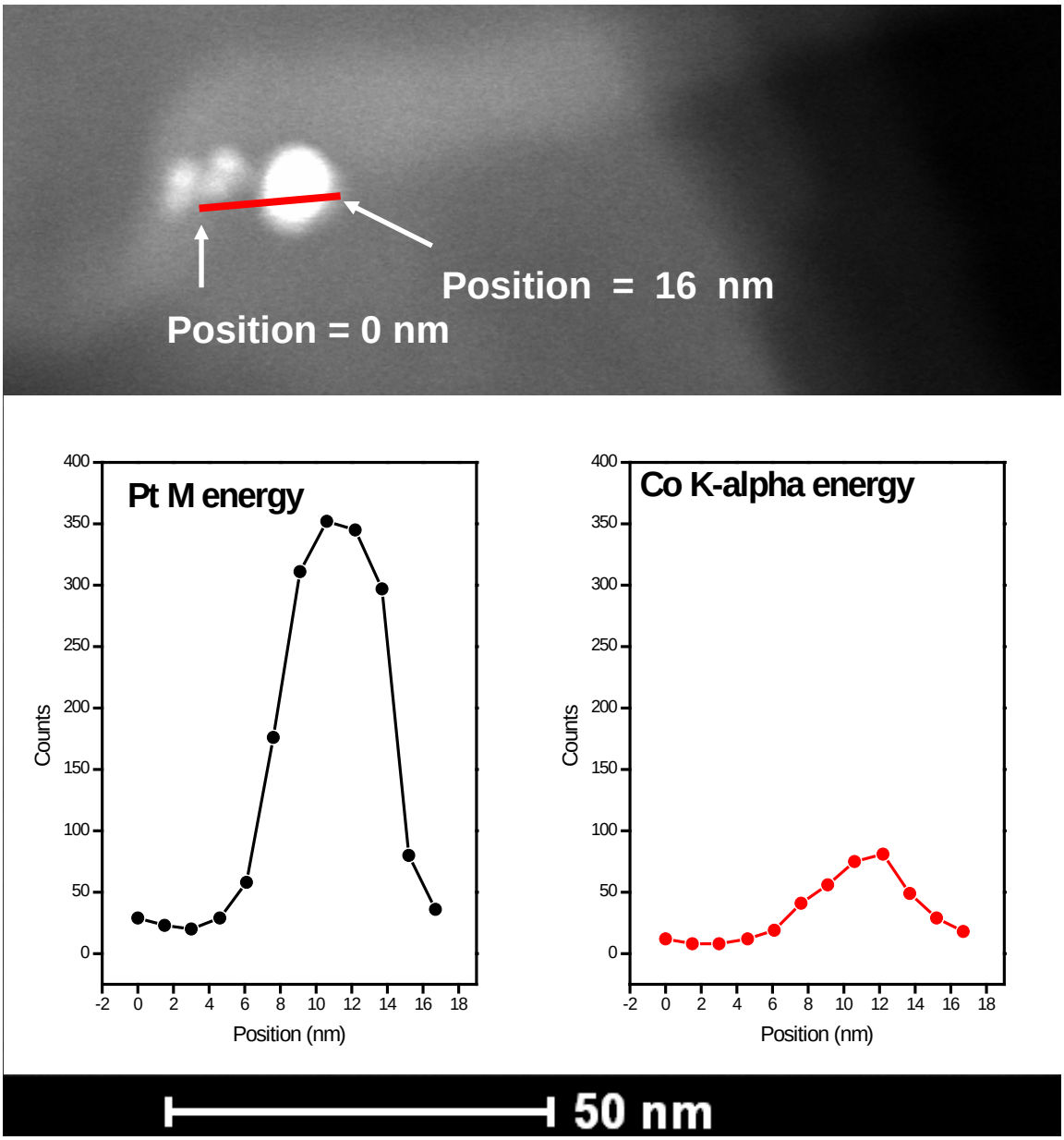

Figure 49. TEM image of a Pt_3Co nanoparticle annealed to 900 K. The image was taken with Tecnai F20 G^2 TEM. Energy Dispersive spectroscopy spot capture was carried out in twelve different positions for 8 s, as shown by the white dots on the red line and number 1-12. Inset: (left) intensities of Pt M peak at different positions, (right) intensities of Co K-α at different positions.

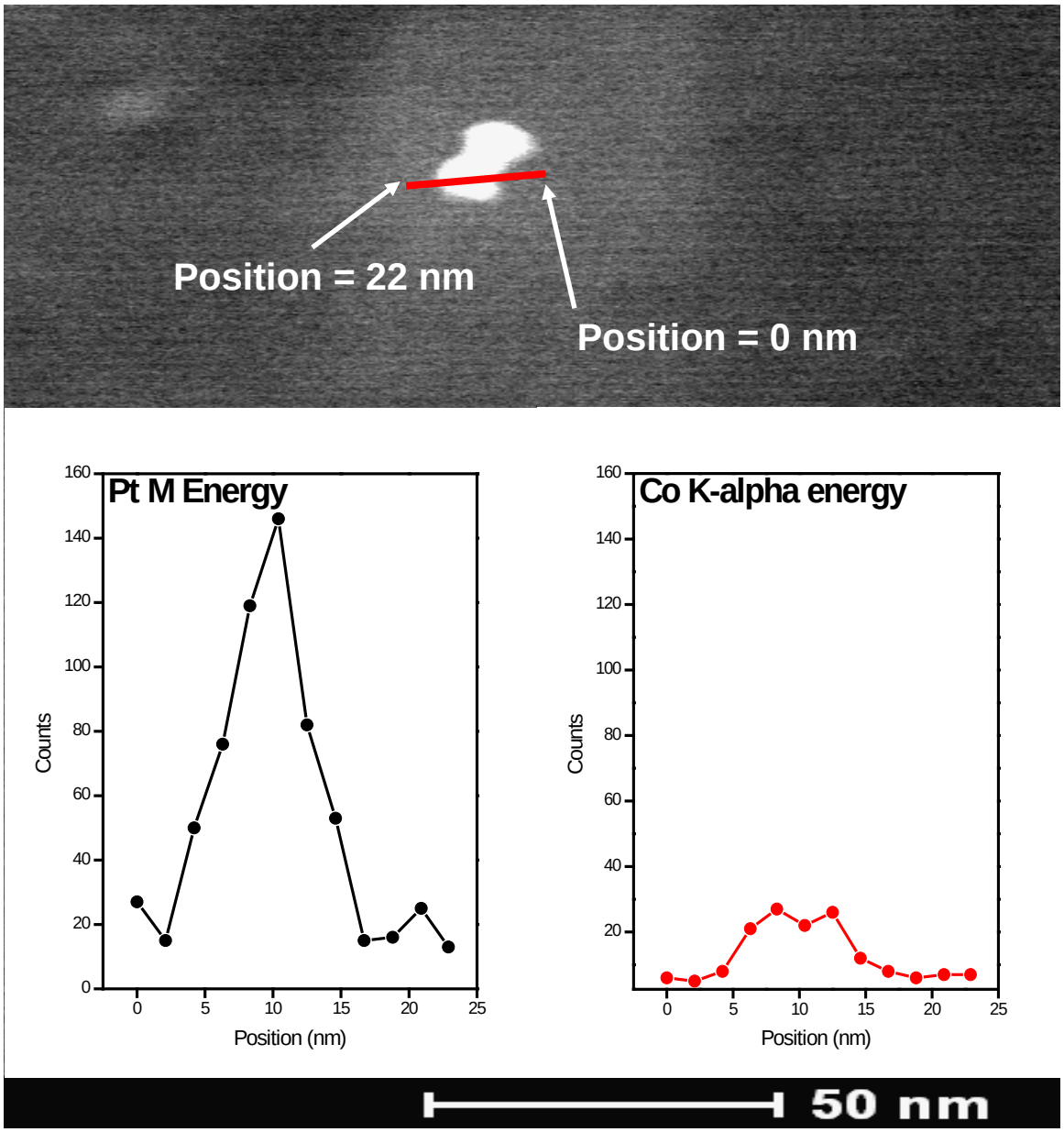

Figure 50. TEM image of a Pt_3Co nanoparticle treated in 0.1 M H_2SO_4 with 1.23V applied potential. The image was taken with Tecnai F20 G^2 TEM. Energy Dispersive spectroscopy spot capture was carried out in twelve different positions for 8 s, as shown by the white dots on the red line and number 1-12. Inset: (left) intensities of Pt M peak at different positions, (right) intensities of Co K-α at different positions.

surface than the core area. This data further confirm the observation made previously, that Co dissolves out of the surface and near surface region.

Another measurement was also done on the system during dissolution study in addition to LEISS and EDX measurements. STM experiments were done on Pt-Co before and after treatment in the electrolyte at 1.23 V applied potential. Figure 51(a) shows the room temperature STM image taken from 0.3ML Pt + 0.1ML after annealing to 900K. Consistent with the previous STM studies of 6.67ML Pt_3Co, the alloying of PtCo is observed in the image. Figure 51(b) is the STM image taken after electrochemical treatment (EC treatment), showing that roughness of the surface happens and a significant particle size reduction is found. From previous section, it is shown that 1.23 V will cause significant Co dissolution. Therefore, this STM data provides the information on the morphology change of Pt-Co clusters when treated in the stated electrolyte with 1.23 V applied potential. The fact that there is a significant particle size reduction proposes that there could be a change in the catalytic activity of the particles after the acid treatment. Recently, the increase in Pt-Co activity towards ORR after a certain acid treatment has been proposed by several research groups.[176,177]

Chen et al. has shown that Pt_3Co supported on carbon and treated in acid and annealed to 1000 K for 3 hour in vacuum will have higher activity towards ORR compared to Pt particles supported on carbon having the same particle size.[176] It was proposed that acid treating Pt_3Co will cause a change in the structure of the particles, where percolated Pt-rich surface and Pt-poor core regions structure is formed. They

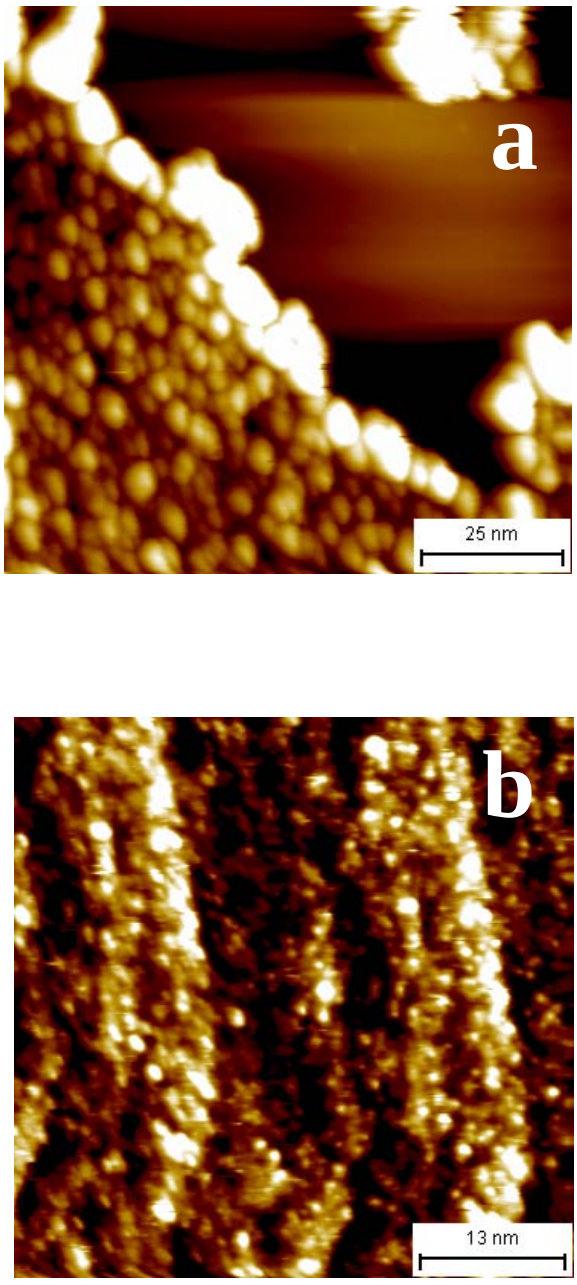

Figure 51. (a) STM image of 0.4ML Pt_3Co annealed to 900K before EC treatment in 0.1 M H_2SO_4 with applied 1.2 V potential (100nm x 100nm, 1.0V, 0.1nA), and (b) STM mage of Pt_3Co after CE treatment followed by annealing to 900K (50nm x 50nm, 1.0V, 0.1nA).

proposed that by having Pt-rich and Pt-poor regions, the interfacial regions could have shortened Pt-Pt bond distance. Shortened Pt-Pt bond distance could lead to lower the valence band center relative to Fermi level,[178,179] reduce the binding strength of oxygenated adsorbates,[168] and enhance the ORR activity.[176] Hence, in this study, they proposed that leaching in acid will cause a shortened Pt-Pt bond distance which will eventually cause an increase in ORR activity.

Another study showing increased activity of Pt alloy after electrochemical treatment is presented by Koh and Strasser.[177] In this study, Pt-Cu is analyzed. It shown that after CV measurement, by applying potential sweep between 0.6 V and 1.2 V, they observed change in CV profile and also on the composition of Pt and Cu. They observed a Pt-enriched Pt-alloy, which essentially Pt surface. They suggested that the dealloying of the alloying metal (in this case Cu) will cause favorable structural arrangements of Pt atoms on the surface.[177]

All the recent studies briefly described above have shown that there is an increase in the activity after the Pt alloy is treated in acid with applied potential, even up to 1.2 V. From EDS measurements, change in chemical composition throughout the particles is observed after Pt-Co clusters are treated in acid with applied potential. It is observed that Co dissolves from the near surface region. STM also shows significant change of the structures, in which the particle size of Pt-Co is significantly reduced. The data presented in this section provide a foundation in proposing the mechanism of increased efficiency of Pt-Co alloy toward ORR activity by observing the change in surface composition of Pt-Co alloy.

7. SUMMARY

Surface characterizations of Au-Pd/SiO_2, Pd-Sn/Rh(100), AuPd(100), Pt-Co thin film, and Pt-Co/HOPG clusters model catalysts were carried out using a combination of low-energy ion-scattering spectroscopy (LEISS), X-ray photoelectron spectroscopy (XPS), low-energy electron diffraction (LEED), temperature programmed desorption (TPD), scanning tunneling microscopy (STM), electrochemistry techniques, infrared reflection absorption spectroscopy (IRAS), and transmitted electron microscopy (TEM).

Au-Pd bimetallic model catalysts were synthesized as alloy clusters on SiO_2 ultrathin films under ultrahigh vacuum (UHV) conditions. Relative to the bulk, the surface of the clusters is enriched in Au. With CO as a probe, IRAS and TPD were used to identify isolated Pd sites at the surface of the supported Au-Pd clusters. Ethylene adsorption and dehydrogenation indicate a clear structure-reactivity correlation with respect to the structure/composition of these Au-Pd model catalysts.

Pd-Sn bimetallic model catalysts were prepared as alloy films on a Rh(100) substrate via physical vapor deposition. The ordered surface alloy of c(2 × 2), showing 50% surface concentration of Pd, has the highest formation rate for vinyl acetate (VA) synthesis. This is consistent with our proposal that a pair of suitably spaced, isolated Pd monomers is the more efficient site for VA synthesis.

A AuPd(100) alloy single-crystal model catalyst bulk alloy's thermodynamic properties and surface lattice spacing were used to control and optimize the concentration of the active site (Pd atom pairs at a specific Pd-Pd distance with Au

nearest-neighbors). Scanning tunneling microscopy reveals that sample annealing has a direct effect on the surface Pd arrangements.

Pt-Co thin films and clusters alloy model catalysts were prepared under UHV condition. Pt surface segregation occurs in both systems, with planar surfaces showing more significant Pt segregation. A stable Pt-Co alloy starts to form when the annealing temperature is between 800 K and 1000 K. Co dissolves from near surface region of Pt-Co thin films and clusters. Particle size reduction of Pt_3Co clusters is observed when significant amount of Co is dissolved from the system.

In this study, we successfully prepared and analyzed several model catalysts using a UHV chamber and multiple surface science techniques. A new methodology to conveniently synthesize bimetallic model catalysts with different surface versus bulk compositions by growing bimetal atomic overlayers on a refractory metal or HOPG substrate (or an oxide support) and subsequent thermal treatments is offered. Results spanning the analysis of isolated Pd active sites on Au-Pd surfaces through the observation of surface segregation of Pt on Pt-Co model alloy surfaces show possibilities for investigating various mixed-metal systems and the correlation between their surface structures to their catalytic functions.

REFERENCES

(1) Engl, T.; Ertl, G. *J. Chem. Phys.* **1978**, *69*, 1267.

(2) Madey, T. E.; Engelhardt, H. A.; Menzel, D. *Surf. Sci.* **1975**, *48*, 304.

(3) Ivanov, V. P.; Boreskov, G. K.; Savchenko, V. I. *J. Catal.* **1977**, *48*, 269.

(4) Valden, M.; Lai, X.; Goodman, D. W. *Science* **1998**, *281*, 1647.

(5) Jia, J.; Haraki, K.; Kondo, M. J. N.; Domen, K.; Tamaru, K. *J. Phys. Chem. B.* **2000**, *104*, 11153.

(6) Hayashi, T.; Tanaka, K.; Haruta, M. *J. Catal.* **1998**, *178*, 566.

(7) Cosandey, F.; Madey, T. E. *Surf. Rev. Lett.* **2001**, *8*, 73.

(8) Bond, G. C.; Thompson, D. T. *Catal. Rev. Sci. Eng* **1999**, *41*, 319.

(9) Bianchi, C.; Porta, F.; Prati, L.; Rossi, M. *Top. Catal.* **2000**, *13*, 231.

(10) Haruta, M.; Tsubota, S.; Kobayashi, T.; Kageyama, H.; Genet, M. J.; Delmon, B. *J. Catal.* **1993**, *144*, 175.

(11) Knell, A.; Barnickel, P.; Baiker, A.; Wokaun, A. *J. Catal.* **1992**, *137*, 306.

(12) Haruta, M.; Yamada, N.; Kobayashi, T.; Iijima, S. *J. Catal.* **1988**, *115*, 301.

(13) Gardner, S. D.; Hoflund, G. B.; Upchurch, B. T.; Schryer, D. R.; Kielin, E. J.; Schryer, J. *J. Catal.* **1991**, *129*, 114.

(14) Valden, M.; Lai, X.; Goodman, D. W. *Science* **1998**, *281*, 1647.

(15) Okazawa, T.; Kohyama, M.; Kido, Y. *Surf. Sci.* **2006**, *600*, 4430.

(16) Parker, S. C.; Campbell, C. T. *Top. Catal.* **2007**, *44*, 3.

(17) Parker, S. C.; Grant, A. W.; Bondzie, V. A.; Campbell, C. T. *Surf. Sci.* **1999**, *441*, 10.

(18) Cosandey, F.; Zhang, L.; Madey, T. E. *Surf. Sci.* **2001**, *474*, 1.

(19) Chen, M. S.; Wallace, W. T.; Kumar, D.; Zhen, Y.; Gath, K. K.; Cai, Y.; Kuroda, Y.; Goodman, D. W. *Surf. Sci.* **2005**, *581*, L115-L121.

(20) Chen, M. S.; Santra, A. K.; Goodman, D. W. *Phys. Rev. B* **2004**, *69*, 155404-1 - 155404-7.

(21) Chen, M. S.; Goodman, D. W. *Surf. Sci.* **2005**, *574*, 259.

(22) Chen, M. S.; Goodman, D. W. *Science* **2004**, *306*, 252.

(23) Rodriquez, J. A.; Goodman, D. W. *Science* **1992**, *257*, 897.

(24) Chen, M. S.; Kumar, D.; Yi, C. W.; Goodman, D. W. *Science* **2005**, *310*, 291.

(25) Rodriquez, J. A.; Jirsak, T.; Chaturvedi, S.; Hrbek, J. *J. Am. Chem. Soc.* **1998**, *120*, 11149.

(26) Besenbacher, F.; Chorkendorff, I.; Clausen, B. S.; Hammer, B.; Molenbroek, A. M.; Norskov, J. K.; Stensgaard, I. *Science* **1998**, *279*, 1913.

(27) Overbury, S. H.; Mullins, D. R.; Paffett, M. T.; Koel, B. E. *Surf. Sci.* **1991**, *254*, 45.

(28) Paffett, M. T.; Logan, A. D.; Simonson, R. J.; Koel, B. E. *Surf. Sci.* **1991**, *250*, 123.

(29) Paffett, M. T.; Windham, R. G. *Surf. Sci.* **1989**, *208*, 34.

(30) Paffett, M. T.; Gebhard, S. C.; Windham, R. G.; Koel, B. E. *J. Phys. Chem.* **1990**, *94*, 6831.

(31) Hayden, B. E.; Rendall, M. E.; South, O. *J. Am. Chem. Soc.* **2003**, *125*, 7738.

(32) Peck, J. W.; Koel, B. E. *J. Am. Chem. Soc.* **1996**, *118*, 2708.

(33) Stamenkovic, V. R.; Arenz, M.; Lucas, C. A.; Gallagher, M. E.; Ross, P. N.; Markovic, N. M. *J. Am. Chem. Soc.* **2003**, *125*, 2736.

(34) Szanyi, J.; Paffett, M. T. *J. Am. Chem. Soc.* **1995**, *117*, 1034.

(35) Xu, C.; Peck, J. W.; Koel, B. E. *J. Am. Chem. Soc.* **1993**, *115*, 751.

(36) Hamm, G.; Schmidt, T. J.; Breitbach, J.; Franke, D.; Becker, C.; Wandelt, K. *Surf. Sci.* **2004**, *562*, 170.

(37) Lee, A. F.; Baddeley, C. J.; Tikhov, M. S.; Lambert, R. M. *Surf. Sci.* **1997**, *373*, 195.

(38) Logan, A. D.; Paffett, M. T. *J. Catal.* **1992**, *133*, 179.

(39) Tsud, N.; Skala, T.; Sutara, F.; Veltruska, K.; Dudr, V.; Fabik, S.; Sedlacek, L.; Chab, V.; Prince, K. C.; Matolin, V. *Surf. Sci.* **2005**, *595*, 138.

(40) Chen, M. S.; Luo, K.; Wei, T.; Kumar, D.; Yi, C. W.; Goodman, D. W. *Catal. Today* **2006**, *117*, 37.

(41) Wei, T.; Goodman, D. W. **in preparation**.

(42) Luo, K.; Wei, T.; CYi, C. W.; Axnanda, S. *J. Phys. Chem. B* **2005**, *109*, 23517.

(43) Yi, C. W.; Luo, K.; Wei, T.; Goodman, D. W. *J. Phys. Chem. B* **2005**, *109*, 18535.

(44) Wei, T.; Wang, J. H.; Goodman, D. W. *J. Phys. Chem. C* **2007**, *111*, 8781.

(45) Maroun, F.; Ozanam, F.; magnussen, O. M.; Behm, R. J. *Science* **2001**, *293*, 1811.

(46) Rieger, P. H. *Electrochemistry*; Second ed.; Kluwer Academic Publishers: Dordrecht, Netherlands, 1994.

(47) Faraday, M. *Philos. T. R. Soc. Lond.* **1833**, *123*, 675.

(48) Faraday, M. *Philos. T. R. Soc. Lond.* **1834**, *124*, 77.

(49) Grove, W. R. *P. R. Soc. Lond.* **1843**, 268-278, 346-354, 422-432.

(50) Ostwald, W. *Electrochemistry, History and Theory*; Amering Publishing Co.: Washington, D. C., 1980.

(51) Tilden, W. A. *Famous Chemists*; Ayer Publishing: Londres, 1968.

(52) Crowe, B. J.; NASA, Ed.; GPO: 1973.

(53) Viswanathan, B.; Scibioh, M. A. *Fuel Cells, Principles and Applications*; Graphica Printers: Hyderabad, 2007.

(54) Appleby, A. J.; Foulkes, F. R. *Fuel Cell Handbook*; Van Nostrand Reinhold: New York, 1989.

(55) Bard, A. J.; Faulkner, L. R. *Electrochemical Methods: Fundamentals and Applications*; John Wiley & Sons, Inc.: New York, 2001.

(56) Kinoshita, K. *Electrochemical Oxygen Technology*; John Wiley & Sons, Inc.: New York, 1992.

(57) Appleby, A. J.; Savy, M. *J. Electroanal. Chem* **1978**, *92*, 15.

(58) Yeager, E. *J. Mol. Catal.* **1986**, *38*, 5.

(59) Zignani, S.; Antolini, E.; Gonzalez, E. R. *J. Power Sources* **2008**, *182*, 83.

(60) Toda, T.; Igarashi, H.; Uchida, H.; Watanabe, M. *J. Electrochem. Soc.* **1999**, *146*, 3750.

(61) Beard, B. C.; Ross, P. N. *J. Electrochem. Soc.* **1990**, *137*, 3368.

(62) Glass, J. T.; Cahen, G. L.; Stoner, G. E. *J. Electrochem. Soc.* **1987**, *134*, 58.

(63) Lucas, C. A.; Markovic, N. M.; Ross, P. N. *Phys. Rev. B* **1997**, *55*, 7964-7971.

(64) Stamenkovic, V.; Mun, B. S.; Mayrhofer, K. J. J.; Ross, P. N.; Markovic, N. M.; Rossmeisl, J.; Greeley, J.; Norskov, J. K. *Angew. Chem. Int. Ed.* **2006**, *45*, 2897-2901.

(65) Wang, Y.; Balbuena, P. B. *J. Phys.Chem. B* **2005**, *109*, 18902.

(66) Hammer, B.; Norskov, J. K. *Adv. Catal.* **2000**, *45*, 71.

(67) Stamenkovic, V.; Schmidt, T. J.; Markovic, N. M.; P. N. Ross, J. *J. Phys. Chem. B* **2002**, *106*, 11970.

(68) Fadley, C. S. In *Electron Spectroscopy, Theory, Techniques, and Applications* Brundle, C. R., Baker, A. D., Eds.; Pergamon Press: New York, 1978.

(69) Brongersma, H. H.; Draxler, M.; Ridder, M. d.; Bauer, P. *Surf. Sci. Rep.* **2007**, *62*, 63.

(70) Ertl, G.; Kuppers, J.; Park, R. L. *Phys. Today* **1976**, *29*, 57.

(71) Attard, G.; Barnes, C. *Surfaces;* Oxford University Press Inc.: New York, 1998.

(72) Binnig, G.; Rohrer, H. *IBM J. Res. Dev.* **1986**, *30*, 355.

(73) Ertl, G.; Kuppers, J. *Low Energy Electrons and Surface Chemistry;* Verlag Chemie: Weinheim, Germany, 1985.

(74) Niehus, H.; Heiland, W.; Taglauer, E. *Surf. Sci. Rep.* **1993**, *17*, 213-303.

(75) King, D. A. *Surf. Sci.* **1975**, *47*, 384.

(76) Luo, K.; Kim, D. Y.; Goodman, D. W. *J. Mol. Catal. A* **2001**, *167*, 191.

(77) Yi, C. W.; Luo, K.; Wei, T.; Goodman, D. W. *J. Phys. Chem. B* **2005**, *109*, 18535.

(78) Province, W. D.; Mills, P. L.; Lerou, J. J. *Stud. Surf. Sci. Catal.* **1996**, *101*, 191.

(79) Bissot, T. C. U.S., 1977.

(80) Crathorne, E. A.; MacGowan, D.; Morris, S. R.; Rawlinson, A. P. *J. Catal.* **1994**, *149*, 254.

(81) Han, Y. F.; Wang, J. H.; Kumar, D.; Yan, Z.; Goodman, D. W. *J. Catal.* **2005**, *232*, 467.

(82) Choudhary, T. V.; Sivadinarayana, C.; Datye, A. K.; Kumar, D.; Goodman, D. W. *Catal. Lett.* **2003**, *86*, 1.

(83) Sarkany, A.; Horvath, A.; Beck, A. *Appl. Catal. A* **2002**, *229*, 117.

(84) Storm, J.; Lambert, R. M.; Memmel, N.; Onsgaard, J.; Taglauer, E. *Surf. Sci.* **1999**, *436*, 259.

(85) Ormerod, R. M.; Baddeley, C. J.; Lambert, R. M. *Surf. Sci. Lett.* **1991**, *259*, L709.

(86) Bonarowska, M.; Malinowski, A.; Juszczyk, W.; Karpinski, Z. *Appl. Catal. B* **2001**, *30*, 187.

(87) Malinowski, A. *Pol. J. Chem.* **2002**, *76*, 1461.

(88) Jablonski, A.; Overbury, S. H.; Somorjai, G. A. *Surf. Sci.* **1977**, *65*, 578.

(89) Wood, B. J.; H., W. *Surf. Sci.* **1975**, *52*, 151.

(90) Swartzfager, D. G.; Ziemecki, S. B.; Kelley, M. J. *J. Vac. Sci. Technol.* **1981**, *19*, 185.

(91) Hilaure, L.; Legare, P.; Holl, Y.; Maire, G. *Surf. Sci.* **1981**, *103*, 125.

(92) Varga, P.; Hetzendorf, G. *Surf. Sci.* **1985**, *162*, 544.

(93) Anton, R.; Eggers, H.; Veletas, J. *Thin Solid Films* **1993**, *226*, 39.

(94) Nascente, P. A. P.; de Castro, S. G. C.; Landers, R.; Kleiman, G. G. *Phys. Rev. B* **1991**, *43*, 4659.

(95) Lee, Y.; Jeon, Y.; Chung, Y.; Lim, K.; Whuang, C.; Oh, S. *J. Kor. Phys. Soc.* **2000**, *37*, 451.

(96) Koel, B. E.; Sellidj, A.; Paffett, M. T. *Phys. Rev. B* **1992**, *46*, 7846.

(97) Weissman-Wenocur, D. L.; Stefan, P. M.; Pate, B. B.; Shek, M. L.; Lindau, I.; Spicer, W. E. *Phys. Rev. B* **1983**, *27*, 3308.

(98) Rainer, D. R.; Xu, C.; Holmblad, P. M.; Goodman, D. W. *J. Vac. Sci. Technol. A* **1997**, *15*, 1653.

(99) Piaszenski, G.; Aschoff, M.; Speller, S.; Heiland, W. *Nucl. Instrum. Methods Phys. Res. B* **1998**, *135*, 331.

(100) Kuntze, J.; Speller, S.; Heiland, W. *Phys. Rev. B* **1999**, *60*, 1535.

(101) Robach, Y.; Abel, M.; Porte, L. *Surf. Sci.* **2003**, *526*, 248.

(102) Rainer, D. R.; Corneille, J. S.; Goodman, D. W. *J. Vac. Sci. Technol. A* **1995**, *13*, 1595.

(103) Davis, R. J.; Boudart, M. *J. Phys. Chem.* **1994**, *98*, 5471.

(104) Refsnyder, S. N.; Lamb, H. H. *J. Phys. Chem. B* **1999**, *103*, 321.

(105) Kaszkur, Z. *Phys. Chem. Chem. Phys.* **2004**, *6*, 193.

(106) Xu, X. P.; Szanyi, J.; Xu, Q.; Goodman, D. W. *Catal. Today* **1994**, *21*, 57.

(107) Min, B. K.; Santra, A. K.; Goodman, D. W. *J. Vac. Sci. Technol. A* **2003**, *21*, 2319.

(108) Min, B. K.; Santra, A. K.; Goodman, D. W. *Catal. Today* **2003**, *85*, 113.

(109) Min, B. K.; Wallace, W. T.; Santra, A. K.; Goodman, D. W. *J. Phys. Chem. B* **2004**, *108*, 16339.

(110) Unterhalt, H.; Rupprechter, G.; Freund, H.-J. *J. Phys. Chem. B* **2002**, *106*, 356.

(111) Wolter, K.; Seiferth, O.; Kuhlenbeck, H.; Baumer, M.; Freund, H.-J. *Surf. Sci.* **1998**, *399*, 190.

(112) Carlsson, A. F.; Naschitzki, M.; Baumer, M.; H.-J., F. *J. Phys. Chem. B* **2003**, *107*, 778.

(113) Guo, X.; Yates, J. T. *J. Chem. Phys.* **1989**, *90*, 6761.

(114) Xu, X.; Goodman, D. W. *J. Phys. Chem.* **1993**, *97*, 7711.

(115) Szanyi, J.; Kuhn, W. K.; Goodman, D. W. *J. Vac. Sci. Tech. A* **1993**, *11*, 1969.

(116) Lemire, C.; Meyer, R.; Shaikhutdinov, S. K.; Freund, H.-J. *Surf. Sci.* **2004**, *552*, 27.

(117) Gelin, P.; Siedle, A. R.; Yates, J. T. *J. Phys. Chem.* **1984**, *88*, 2978.

(118) Rainer, D. R.; Wu, M. C.; Mahon, D. I.; Goodman, D. W. *J. Vac. Sci. Tech. A* **1996**, *14*, 1184.

(119) Guo, X.; Madix, R. J. *J. Am. Chem. Soc.* **1995**, *117*, 5523.

(120) Shaikhutdinov; Baumer, M.; Lear, T..; Lennon, D.; Oldman, R. J.; Jackson, S. D.; Freund, H.-J. *J. Catal.* **2001**, *200*, 330.

(121) Stuve, E. M.; Madix, R. J. *Surf. Sci.* **1985**, *152/153*, 1985.

(122) Frank, M.; Baumer, M. *Phys. Chem. Chem. Phys.* **2000**, *2*, 3723.

(123) Gates, J. A.; Kesmodel, L. L. *Surf. Sci.* **1983**, *124*, 68.

(124) Campbell, R. A.; Goodman, D. W. *Rev. Sci. Instrum.* **1992**, *63*, 172.

(125) Leung, L. W. H.; He, J. W.; Goodman, D. W. *J. Chem. Phys.* **1990**, *93*, 8328.

(126) Haner, A. N.; Ross, P. N.; Bardi, U. *Surf. Sci.* **1991**, *249*, 15.

(127) Ortega, A.; Huffman, F. M.; Bradshaw, A. M. *Surf. Sci.* **1982**, *119*, 79.

(128) Kuhn, W. K.; Szanyi, J.; Goodman, D. W. *Surf. Sci. Lett.* **1992**, *274*, L611.

(129) Han, Y. F.; Kumar, D.; Sivadinarayana, C.; Goodman, D. W. *Catal. Lett.* **2004**, *94*, 131.

(130) Han, Y. F.; Kumar, D.; Sivadinarayan, C.; Clearfield, A.; Goodman, D. W. *J. Catal.* **2004**, *224*, 60.

(131) Han, Y. f.; Kumar, D.; Goodman, D. W. *J. Catal.* **2005**, *230*, 353.

(132) Kumar, D.; han, Y. F.; Chen, M. S. *Catal. Lett.* **2006**, *106*, 1.

(133) Kumar, D.; Han, Y. F.; Goodman, D. W. *Top. Catal.* **2007**, *46*, 169.

(134) Kumar, D.; Chen, M. S.; Goodman, D. W. *Catal. Today* **2007**, *123*, 77.

(135) Bell, A. T. *Science* **2003**, *299*, 1688.

(136) Valden, M.; Lai, X.; Goodman, D. W. *Science* **1998**, *281*, 1647.

(137) Nakamura, S.; Yasui, T. *J. Catal.* **1970**, *17*, 366.

(138) Samanos, B.; Boutry, P.; Montarna, R. *J. Catal.* **1971**, *23*, 19.

(139) Gordon, P. *The Order-Disorder Transformation: Principles of Phase Diagrams in Material Systems*; McGraw-Hill: New York, 1968.

(140) Aschoff, M.; Speller, S.; Kuntze, J.; Heliand, W.; Platzgummer, E.; Schmid, M.; Varga, P.; Baretzky, B. *Surf. Sci.* **1998**, *415*, L1051.

(141) Hatzor, A.; Weiss, P. S. *Science* **2001**, *291*, 1019.

(142) Roder, H.; Hahn, E.; Brune, H.; Bucher, J. P.; Kern, K. *Nature* **1993**, *366*, 141.

(143) Tseng, G. Y.; Ellenbogen, J. C. *Science* **2001**, *294*, 1293.

(144) Hebenstreit, E. L. D.; Hebenstreit, W.; Schmid, M.; Varga, P. *Surf. Sci.* **1999**, *441*, 441.

(145) Schmid, M.; Varga, P. In *The Chemical Physics of Solid Surfaces: Alloy Surface and Surface Alloys*; Woodruff, D. P., Ed.; Elsevier Science: New York, 2002; Vol. 10, p 118.

(146) Wouda, P. T.; Schmid, M.; Nieuwenhuys, B. E.; Varga, P. *Surf. Sci.* **1998**, *417*, 292.

(147) It should be noted that this method may underestimate the number of surface Pd atoms, as the cutoff height is set relatively high above the surface to avoid any accidental inclusion of Au atoms.

(148) Han, P.; Mantooth, B. A.; Sykes, E. C. H.; Donhauser, Z. J.; Weiss, P. S. *J. Am. Chem. Soc.* **2004**, *126*, 10787.

(149) Guczi, L. *Catal. Today* **2005**, *101*, 53.

(150) Okamoto, H.; Massalski, T. B. *Bull. Alloy Phase Diagr.* **1985**, *6*, 229.

(151) Gauthier, Y.; Dolle, P.; Baudoing-Savois, R.; Hebenstreit, W.; Platzgummer, E.; Schmid, M.; Varga, P. *Surf. Sci.* **1998**, *396*, 137.

(152) Niehus, H.; T., B.; Voetz, M.; Morgenstern, K. *Surf. Rev. Lett.* **1996**, *3*, 1899.

(153) Rodewald, M.; Rodewald, K.; DeMeulenaere, P.; VanTendeloo, G. *Phys. Rev. B* **1997**, *55*, 14173.

(154) Although no deliberate quenching was performed, we assume that all processes involving atomic rearrangement have undetectable relaxation time during STM imaging at room temperature.

(155) Ivernova, V. I.; Katsnel'son, A. A. *Sov. Phys. Crytallogr.* **1967**, *11*, 504.

(156) Stamenkovic, V.; Fowler, B.; Mun, B. S.; Wang, G.; Ross, P. N.; Lucas, C. A.; Markovic, N. M. *Science* **2007**, *315*, 493.

(157) Persson, K.; Ersson, A.; Jansson, K.; Iverlund, N.; Jaras, S. *J. Catal.* **2005**, *231*, 139.

(158) It should be noted that at the thermodynamic properties of alloy nanoparticles might be considerably different from those of the alloy single crystal. Further investigation on the order-disorder transformation of alloy nanoparticles is necessary.

(159) Bezerra, C. W. B.; Zhang, L.; Liu, H.; Lee, K.; Marques, A. L. B.; Marques, E. P.; Wang, H.; Zhang, J. *J. Power Sources* **2007**, *173*, 891.

(160) Watanabe, M.; Tsurumi, K.; Mizukami, T.; Nakamura, T.; Stonehart, P. *J. Electrochem. Soc.* **1994**, *141*, 2659.

(161) Kim, K. T.; Hwang, J. T.; Kim, Y. G.; Chung, J. S. *J. Electrochem. Soc.* **1993**, *140*, 31.

(162) Gottesfeld, S.; Paffett, M. T.; Redondo, A. *J. Electroanal. Chem* **1986**, *205*, 163.

(163) Daube, K. A.; Paffett, M. T.; Gottesfeld, S.; Campbell, C. T. *J. Vac. Sci. & Tech. A* **1986**, *A4*, 1617.

(164) Paffett, M. T.; Berry, J. G.; Gottesfeld, S. *J. Electrochem. Soc.* **1988**, *135*, 1431.

(165) Paffett, M. T.; Daube, K. A.; Gottesfeld, S.; Campbell, C. T. *J. Electroanal. Chem* **1987**, *220*, 269.

(166) Glass, J. T.; George, J. T.; Cahen, G. L.; Stoner, G. E.; Taylor, E. J. *J. Electrochem. Soc.* **1987**, *134*, 58.

(167) Adzic, R. R.; Zhang, J.; Sasaki, K.; Vukmirovic, M. B.; Shao, M.; Wang, J. X.; Nilekar, A. U.; Mavrikakis, M.; Valerio, J. A.; Uribe, F. *Top. Catal.* **2007**, *46*, 249.

(168) Mukerjee, S.; Srinivasan, S.; Soriaga, M. P.; McBreen, J. *J. Electrochem. Soc.* **1995**, *142*, 1409.

(169) Fernandez, J. L.; White, J. M.; Sun, Y.; Tang, W.; Henkelman, G.; Bard, A. J. *Langmuir* **2006**, *22*, 10426.

(170) Kumar, D.; Chen, M. S.; Goodman, D. W. *Thin Solid Films* **2007**, *515*, 1475.

(171) Luo, Z. P. *Acta. Mater.* **2006**, *54*, 47.

(172) Astana, A.; Matsui, Y.; Yasuda, M.; Kimoto, K.; Iwata, T.; Ohshima, K. *J. App. Cryst.* **2005**, *38*, 361.

(173) Fernandez, J. L.; White, J. M.; Sun, Y.; Tang, W.; Henkelman, G.; Bard, A. J. *Langmuir* **2006**, *22*, 10426-10431.

(174) Fernandez, J. L.; Walsh, D. A.; Bard, A. J. *J. Am. Chem. Soc.* **2005**, *127*, 357.

(175) Lim, B.; Jian, M.; Camargo, P. H. C.; Cho, E. C.; Tao, J.; Lu, X.; Zhu, Y.; Xia, Y. *Science* **2009**, *324*, 1302.

(176) Chen, S.; Ferreira, P. J.; Sheng, W.; Yabuuchi, N.; Allard, L. F.; Shao-Horn, Y. *J. Am. Chem. Soc.* **2008**, *130*, 13818.

(177) Koh, S.; Strasser, P. *J. Am. Chem. Soc.* **2007**, *129*, 12624.

(178) Xu, Y.; Ruban, A. V.; Mavrikakis, M. J. *J. Am. Chem. Soc.* **2004**, *126*, 4717.

(179) Mavrikakis, M.; Hammer, B.; Norskov, J. K. *Phys. Rev. Lett.* **1998**, *81*, 2819.

VITA

Stephanus Axnanda was born to Kilian Lumban Gaol and Karnatje Manurung in Rumbai, Sumatra, Indonesia. He received B.S. and M.S. in chemical engineering from Texas A&M University in December 2002 and May 2004, respectively. In Fall 2004, he went on to pursue his doctoral study and joined Dr. D. Wayne Goodman's research group, and graduated with his PhD in December 2009. Stephanus may be reached at: Chemistry Department, Texas A&M University PO Box 30012, College Station, TX 77842-3012. His e-mail address is: stephanus.axnanda@gmail.com.